

---

# The impact of antisite disorder on magnetism and transport in the double perovskites

---

By

**Viveka Nand Singh**

Harish-Chandra Research Institute, Allahabad



A Thesis submitted to the  
Board of Studies in Physical Science Discipline  
In partial fulfilment of requirements  
For the degree of  
**DOCTOR OF PHILOSOPHY**  
of  
Homi Bhabha National Institute



June 2012



## Certificate

This is to certify that the Ph.D thesis titled “The impact of antisite disorder on magnetism and transport in the double perovskites” submitted by Viveka Nand Singh is a record of bonafide research work done under my supervision. It is further certified that the thesis represents independent work by the candidate and collaboration was necessitated by the nature and scope of the problems dealt with.

Date:

**Prof. Pinaki Majumdar**

Thesis Adviser



## Declaration

This thesis is a presentation of my original research work. Whenever contributions of others are involved, every effort is made to indicate this clearly, with due reference to the literature and acknowledgment of collaborative research and discussions.

The work is original and has not been submitted earlier as a whole or in part for a degree or diploma at this or any other Institution or University.

This work was done under the guidance of Prof. Pinaki Majumdar, at Harish-Chandra Research Institute, Allahabad.

Date:

**Viveka Nand Singh**

Ph. D. Candidate



*To my family...*



# Acknowledgments

First and foremost, I would like to thank my supervisor Professor Pinaki Majumdar for his sincere guidance and support during my PhD work. I learned a lot from him, during the discussions which used to be very exciting and challenging. He taught me how one should think through the research problem and constantly encouraged me to think independently.

I would also like to thank my collaborators Dr. Sanjoy Datta and Dr. Subrat Das. It was a wonderful experience to work with them.

I would like to thank Prof. G. V. Pai, with whom I have many wonderful discussions on physics and personal issues. These discussions were very helpful to me. He was there whenever I needed any help.

Next, I would like to thank Dr. Prabuddha Sanyal, Dr. Shamik Banerjee, Dr. Anamitra Mukharjee, Dr. Kalpatru Pradhan, and Rajarshi Tiwari. I enjoyed many beneficial discussions with them.

I would like to thank the entire condensed matter group at Harish-Chandra Research Institute (HRI), they were very supportive and I would also like to acknowledge many useful discussions with them. I would also like to thank the entire HRI community for making my stay enjoyable and memorable during my PhD. I would like to acknowledge the use of the High Performance Scientific Computing facility at HRI.

Finally, I would thank my parents and my wife, without their love, support, and faith, this venture could not have been successful. I would like to thank Akansha for carefully reading the thesis and providing useful suggestions.

I dedicate this thesis to my family members.



# Synopsis

---

Title : The Impact of Antisite Disorder on Magnetism and Transport in the Double Perovskites

Name : Viveka Nand Singh

Supervisor : Prof. Pinaki Majumdar

Affiliation : Harish-Chandra Research Institute, Allahabad

---

Perovskites are materials of the form  $ABO_3$ , while ‘double perovskites’ are of the form  $ABO_3 \cdot AB'O_3 \equiv A_2BB'O_6$ . The B and B' are the electronically active ions, typically  $3d$ ,  $4d$  or  $5d$  elements, while A is either a rare earth or alkaline earth and controls the valence. There has been enormous activity in the perovskite oxides over the last two decades, starting with the discovery of high  $T_c$  superconductivity, and this has inspired the study of these more complex, and potentially richer, double perovskites.

The large number of possible B, B' combinations indeed leads to a variety of electronic and magnetic phases. For example,  $Sr_2FeMoO_6$  has a high ferromagnetic  $T_c$  (420K), half-metallic behavior, and large low field magnetoresistance (MR).  $La_2NiMnO_6$  has a dielectric anomaly arising from the structural modes, while  $Sr_2CrOsO_6$  and  $Sr_2CrReO_6$  show magneto-optical properties.

The B ions are usually magnetic, Fe, Co, Ni, Cr, or Mn, while B' is typically non-magnetic, *e.g.*, Mo or W. Both B and B' sit at the center of oxygen octahedra, *i.e.*, are coordinated by six oxygen. In the structurally *ordered* double perovskite (DP) the B and B' should alternate along each cubic axis. However, unless the B and B' are very dissimilar ions, there is a significant possibility of mislocation. The B ion can occupy a B' site and *vice versa*. In fact the B-B' ordering tendency has to compete with the entropy gain from mislocation. This aspect is completely absent in the simple perovskites where there is only one kind of ‘B site’. The inevitable ‘antisite disorder’ (ASD) has to be understood in any modeling of the double perovskites. The promise of rich functionality in the double perovskites remains unfulfilled due to this B, B' mislocation.

In the structurally ordered materials the magnetic ordering arises from a com-

bination of strong electron-spin coupling on the B ion and electron delocalisation on the B-O-B' network. The magnetic order, however, is also strongly affected by the local ordering of B and B' ions. Two neighboring B ions, arising from mislocation, usually have an antiferromagnetic (AFM) superexchange between them. This new coupling can drastically affect physical properties, including magnetic order and transport.

The presence of disorder brings up the following broad issues:

1. *Modeling the disorder*: how does one generate structural motifs that involve 'correlated' rather than random mislocations?
2. *Effect on magnetic order*: the effect on ferromagnetic order is relatively easy to analyse; what is the effect on non ferromagnetic states?
3. *Impact on transport*: how are the resistivity and magnetoresistance affected by the antisite disorder and thermal fluctuations?
4. *Inferring the domain pattern*: what can we infer about the domain structure and disorder from spectroscopic tools like neutron scattering?

The first issue is now reasonably well understood, based on recent work at HRI. This thesis involves the study of four problems motivated by issues 2-4 above. They throw some light on existing experimental data, make predictions where experiments do not yet exist, and try to provide a general conceptual advance for disordered metallic magnets. The problems are:

- The impact of correlated antisite disorder on the ferromagnetic state, clarifying the effect on magnetisation, transport, and half-metallicity.
- The effect of antisites on the metallic antiferromagnetic states that are predicted in the electron doped double perovskites.
- The huge *positive* magnetoresistance that emerges in the antiferromagnetic metal, and its survival in presence of disorder.
- The magnon spectrum in the domain ferromagnetic state, and the inference about domain structure from the magnon lineshapes.

**Chapter 1** of the thesis summarises key experimental observations on the double perovskites, emphasising the effects of antisite disorder, and also describes past efforts at modeling these materials. This includes discussions of the following aspects: (i) the spatially correlated nature of ASD as inferred from electron microscopy and x-ray absorption fine structure (XAFS), (ii) the effect of the AFM superexchange, across domain boundaries, on the bulk magnetisation, (iii) the temperature dependence of resistivity including the effect of ASD and grain boundaries, (iv) the magnetoresistance observed in single crystals and polycrystals, (v) the impact of ASD on the electron spin-polarisation, and (vi) the status of the search for non ferromagnetic metallic phases.

**Chapter 2** discusses the construction of our model Hamiltonian incorporating the structural, electronic and magnetic degrees of freedom. We describe the use of a simple “lattice-gas” model for the structural variables which, on poor annealing, generates a domain structure mimicking the antisite pattern. The electronic-magnetic model is defined on this structural motif and solved via a real space Monte Carlo technique involving the “travelling cluster” algorithm (TCA). We also describe the method for transport calculation and the extraction of the spin resolved density of states.

**Chapter 3** is concerned with the impact of ASD on the ferromagnetic phase. We discover that, for antisite disorder with a high degree of short-range correlations, the antiphase boundaries act also as magnetic domain walls in the ferromagnet. Increasing ASD reduces the low-field magnetization, destroys the half-metallicity, and makes the ground state insulating. While these are disadvantages, we also note that the ferromagnetic  $T_c$  is only weakly affected by moderate ASD and the low-field magnetoresistance is dramatically enhanced by disorder. Our real space approach allows an interpretation of these results in terms of the domain pattern, the effective exchange, and the short-range magnetic correlations. They are also consistent with explicit spatial imagery from recent experiments. The “intra-grain” effects highlighted here would be directly relevant to single crystals, and define the starting point for a transport theory of the polycrystalline double perovskites.

**Chapter 4** focuses on the metallic antiferromagnetic phase, and the phase

coexistence window. For spatially correlated antisite disorder the AFM order is affected *much less strongly* than in the FM case. This intriguing result arises from the finite  $\mathbf{Q}$  nature of AFM order which leads to a weaker ‘cancellation’ of the order between domains. For a given structural order parameter  $S$  (which measures the fraction of correctly located sites) the A type AFM structure factor follows  $D_A \sim (1 + S^2)/2$ , in contrast to  $D_F \sim S^2$  in the ferromagnet, while the G type phase follows  $D_G \sim (1 + S)^2/4$ . So, despite the possibility of large antisite disorder in the electron doped double perovskites, there is certainly hope of observing AFM phases. The AFM states are metallic, and the electronic wavefunctions in these phases continue to be spatially extended even at large disorder. Antisite disorder increases the residual resistivity, but, unlike the ferromagnet, we do not observe any insulating regime.

**Chapter 5** discusses the field response in the antiferromagnetic DP metals. While the zero field resistivity is unremarkable in these systems, they have huge *positive* MR. In contrast to elaborate structure factor measurements *etc.*, this is a direct indicator of the metallic AFM system. Beyond a modest field needed for suppression of long range AFM order, the system shows more than *ten-fold* increase in resistivity near  $T_c$  in a structurally ordered system. The ratio continues to be almost *two-fold* even in systems with  $\sim 25\%$  ASD. An applied field suppresses long range AFM order leading to a state with *short range AFM correlations* in the field induced FM background. These AFM fluctuations generate strong electronic scattering and a resistivity that can be much larger than the ordered AFM metal. Although our explicit demonstration is in the context of a two dimensional spin-fermion model of the DPs, the mechanism we uncover is far more general and complementary to the colossal negative MR process. It should operate in other local moment metals that show a field driven suppression of non ferromagnetic order.

**Chapter 6** describes our results on magnons in the antisite disordered ferromagnets. We use an effective Heisenberg model with parameters that match the magnetisation from the parent electronic problem. We obtain the magnon excitations using the spin rotation technique coupled with the Holstein-Primakoff transformation in the large spin limit. To leading order this results in a non-interacting

disordered boson (magnon) problem that can be solved via Bogolyubov transformation. We provide a detailed description of the spin wave excitations of this complex magnetic state with large spin ( $S$ ), obtained within a  $1/S$  expansion, for progressively higher degree of mislocation, *i.e.*, antisite disorder. The results on magnon energy and broadening reveal that even at very large disorder, the existence of domain like structure ensures that the response has a strong similarity to the clean case. We tried out a scheme for inferring the domain size from the spin wave damping so that experimenters can make an estimate of domains without having spatial data, and we find it to be reasonably successful. We also highlight how the common assumption about random antisites, that is widely used in modeling these materials, would lead to a gross overestimate of magnon damping. In summary, dynamical neutron scattering can be a direct probe of the unusual ferromagnetic state in these materials and confirm the presence of correlated antisites.

To summarise, this thesis considers some problems in the antisite disordered double perovskite magnets. We clarify the impact of correlated antisite disorder on both ferromagnetic and antiferromagnetic phases, discover that the antiferromagnet is robust to large disorder, and find that the antiferromagnetic metal has a surprisingly large positive magnetoresistance. Finally, we have provided results on the magnon spectrum in the non trivial domain ferromagnetic phase and provide an interpretation of the spectrum in terms of magnon confinement.



## List of Publications/Preprints

---

1. Antisite Domains in Double Perovskite Ferromagnets: Impact on Magnetotransport and Half-metallicity  
Viveka Nand Singh and Pinaki Majumdar  
Europhys. Lett. **94**, 47004 (2011), arXiv: **1009.1702** (2010).
2. Antiferromagnetic Order and Phase Coexistence in a Model of Antisite Disordered Double Perovskites  
Viveka Nand Singh and Pinaki Majumdar  
Eur. Phys. J. B **83**, 147-155 (2011), arXiv: **1009.1709** (2010).
3. Huge Positive Magnetoresistance in Antiferromagnetic Double Perovskite Metals  
Viveka Nand Singh and Pinaki Majumdar  
arXiv: **1107.0782** (2011).
4. The Magnon Spectrum in the Domain Ferromagnetic State of Antisite Disordered Double Perovskites  
Subrat Kumar Das, Viveka Nand Singh, and Pinaki Majumdar  
arXiv: **1204.1194** (2012).
5. Thermally Fluctuating Inhomogeneous Superfluid State of Strongly Interacting Fermions in an Optical Lattice  
Viveka Nand Singh, Sanjoy Datta, and Pinaki Majumdar  
arXiv: **1104.4912** (2011).

The material in papers 1-4 above is discussed in the thesis.



# Contents

<b>1</b>	<b>Experimental Summary</b>	<b>1</b>
1.1	Introduction . . . . .	1
1.2	Double perovskites . . . . .	2
1.3	Magnetic order . . . . .	3
1.3.1	Ferromagnetic insulating phase . . . . .	3
1.3.2	Antiferromagnetic insulating phase . . . . .	4
1.3.3	Spin glass phase . . . . .	5
1.3.4	Ferromagnetic metallic phase . . . . .	6
1.4	Impact of doping . . . . .	10
1.4.1	Impact of hole doping . . . . .	11
1.4.2	Impact of electron doping . . . . .	11
1.4.3	Isoelectronic doping . . . . .	12
1.5	Antisite disorder . . . . .	12
1.5.1	Spatial nature of mislocation . . . . .	13
1.5.2	Impact on magnetisation . . . . .	14
1.5.3	Impact on spin-polarisation . . . . .	15
1.5.4	Impact on transport properties . . . . .	16
1.6	Non-ferromagnetic metallic phases . . . . .	18
<b>2</b>	<b>Model and Method</b>	<b>25</b>
2.1	Past theoretical studies . . . . .	25
2.1.1	Ordered double perovskites . . . . .	25
2.1.2	Disordered double perovskites . . . . .	29
2.2	Structural motif generation . . . . .	31
2.3	Quantifying antisite disorder . . . . .	36
2.4	Electronic Hamiltonian . . . . .	38

*Contents*

2.5	Monte Carlo method . . . . .	40
2.6	Transport and spin-resolved density of states . . . . .	41
2.6.1	Transport . . . . .	41
2.6.2	Spin resolved density of states . . . . .	42
<b>3</b>	<b>Impact of Antisite Disorder on the Ferromagnetic Phase</b>	<b>45</b>
3.1	Introduction . . . . .	45
3.2	Magnetic domain formation . . . . .	46
3.3	Temperature dependence of magnetisation . . . . .	46
3.4	Temperature dependence of resistivity . . . . .	49
3.5	Field dependence of resistivity . . . . .	52
3.6	Half-metallicity . . . . .	54
3.6.1	Impact of disorder at low temperature . . . . .	55
3.6.2	Temperature dependence . . . . .	55
3.6.3	Polarisation and itinerant moment . . . . .	56
3.7	Discussion . . . . .	57
3.7.1	Role of dimensionality . . . . .	57
3.7.2	Hubbard interactions . . . . .	58
3.7.3	Effect of grain boundaries . . . . .	59
3.8	Conclusion . . . . .	59
<b>4</b>	<b>Impact of Antisites on Antiferromagnetic Order</b>	<b>63</b>
4.1	Introduction . . . . .	63
4.2	Earlier studies on AFM order . . . . .	67
4.3	Disorder configurations . . . . .	69
4.4	AFM order with antisite disorder . . . . .	69
4.4.1	A type order . . . . .	72
4.4.2	G type order . . . . .	73
4.5	Transport with antisite disorder . . . . .	74
4.6	Phase coexistence . . . . .	77
4.7	Discussion . . . . .	78
4.8	Conclusions . . . . .	80

<b>5</b>	<b>Field Response in Antiferromagnetic Metals</b>	<b>83</b>
5.1	Introduction . . . . .	83
5.2	Field response in ordered AFM metal . . . . .	84
5.2.1	Field cooling . . . . .	85
5.2.2	Zero field cooling . . . . .	86
5.3	Response in antisite disordered AFM metals . . . . .	90
5.4	Discussion . . . . .	91
5.4.1	Earlier theory . . . . .	91
5.4.2	Experimental results . . . . .	92
5.4.3	Qualitative analysis . . . . .	92
5.5	Conclusion . . . . .	94
<b>6</b>	<b>Magnon Spectrum in the Domain Ferromagnetic State</b>	<b>97</b>
6.1	Introduction . . . . .	97
6.2	Effective magnetic model . . . . .	99
6.2.1	Structural motif . . . . .	99
6.2.2	Electronic Hamiltonian . . . . .	101
6.2.3	Effective Heisenberg Hamiltonian . . . . .	102
6.3	Spin dynamics . . . . .	103
6.3.1	Spin-wave excitation . . . . .	103
6.3.2	Dynamical structure factor . . . . .	105
6.4	Results and discussion . . . . .	106
6.4.1	Antiferromagnetically coupled domains . . . . .	107
6.4.2	Broadening: impact of domain size . . . . .	108
6.4.3	Contrast with uncorrelated antisites . . . . .	110
6.5	Conclusion . . . . .	112
<b>7</b>	<b>Thesis Summary</b>	<b>115</b>



# Chapter 1

## Experimental Summary

**Chapter summary:** This chapter summarises the key experimental observations on the double perovskites, emphasising the effects of antisite disorder. We highlight the spatially correlated nature of antisite disorder as inferred from electron microscopy and x-ray absorption fine structure (XAFS) studies. We move on to describe the impact of antiferromagnetic superexchange, present across the antiphase boundary, on the bulk magnetisation. We then discuss the temperature dependence of resistivity, including the effect of antisite disorder and grain boundaries, and magnetoresistance in single crystals and polycrystals. Finally, we comment on the impact of antisite disorder on half-metallicity, and the status of the search for non-ferromagnetic metallic phases.

### 1.1 Introduction

Perovskites are materials of the form  $ABO_3$ , where A is an alkaline earth or rare earth cation (Ca, Sr, La *etc.*), and B is an electronically active transition metal cation (Mn, Fe, Co, Ni, V, Cu *etc.*). The B ion sits in an octahedral environment ( $BO_6$ ) while the A cations occupy the vacant space between the corner shared  $BO_6$  octahedra. Perovskite oxides have been intensely studied over the last few decades since they show a rich variety of magnetic, electrical and optical properties. The manganites [1], cuprates [2], vanadates [3], *etc.*, are a few prominent examples. Since our study is mostly concerned with the magnetism in double perovskites, let us start with a quick description of an important ‘simple’ perovskite, the manganites, to set the stage.

Activity on the manganites started with studies of the impact of doping on the properties of  $\text{LaMnO}_3$  [4].  $\text{LaMnO}_3$  is an antiferromagnetic insulator. With Sr doping it goes to a ferromagnetic phase, with transition temperature  $T_c \sim 250\text{K}$  for  $\text{La}_{0.825}\text{Sr}_{0.175}\text{MnO}_3$  [5]. On a wider range of doping and cation combination the magnetic order in manganites vary from ferromagnetic to antiferromagnetic to spin-glass, while the transport character changes from metallic to insulating.

The doping induced ferromagnetic phase shows a spectacularly large decrease in resistivity on application of a magnetic field [6]; this property is also known as colossal magnetoresistance (CMR). The strong coupling of electronic, magnetic, and structural degrees of freedom gives rise to a wide spectrum of properties involving charge, orbital, and magnetic ordering [7]. Doped manganites show CMR effect at relatively low temperature and high magnetic field, which undermine its application in mass storage memory devices. This encouraged further studies on oxide materials with magnetic ordering temperatures substantially higher than the manganites.

## 1.2 Double perovskites

The double perovskite,  $\text{Sr}_2\text{FeMoO}_6$  [8] (SFMO), was found to have several desirable properties. Ordered  $\text{Sr}_2\text{FeMoO}_6$  exhibits pronounced negative magnetoresistance [9] at *lower* magnetic fields and *higher* temperatures compared to the doped manganites. It has a ferrimagnetic ground state with transition temperature  $T_c \sim 420\text{K}$ . It shows half-metallic character, *i.e.*, only one spin channel conducts, which makes it applicable in spintronic devices. Although it does not (yet) have the rich doping induced phase diagram of the manganites, SFMO does show several unusual magnetic and transport properties [8].

This in turn inspired the study of more complex and potentially richer double perovskites: materials of the form  $\text{ABO}_3.\text{AB}'\text{O}_3 \equiv \text{A}_2\text{BB}'\text{O}_6$  (Figure 1.1). They have two kinds of octahedra,  $\text{BO}_6$  and  $\text{B}'\text{O}_6$ , repeating in all three directions, instead of only the  $\text{BO}_6$  octahedra as in perovskite. B and B' are electronically active transition metal cations.

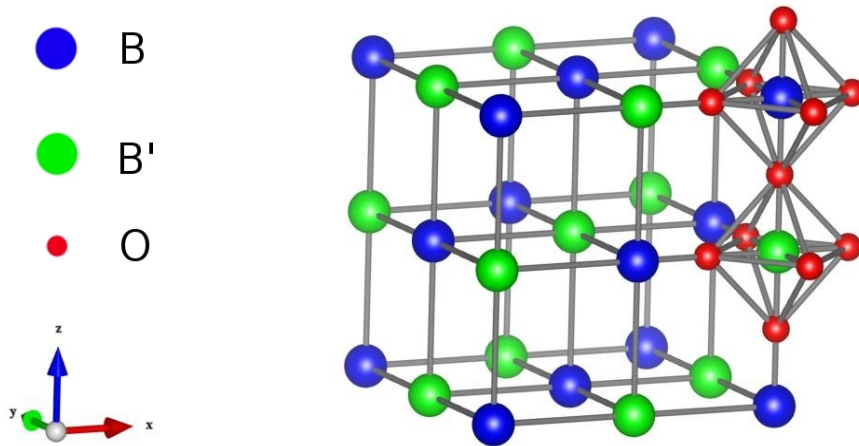


Figure 1.1: Schematic structure of  $A_2BB'O_6$ : for clarity only a few of the oxygen atoms are shown, while the A atoms at the body-center positions (centers of small cubes) are not shown at all.

## 1.3 Magnetic order

The large number of possible B, B' combinations in double perovskites lead to a variety of magnetic phases. As an illustrative list:

- Ferromagnets - listed in Table: 1.1
- Antiferromagnets - listed in Table: 1.2
- Spin glass -  $Sr_2FeCoO_6$  [10],  $Ba_2YMoO_6$  [11]

Apart from the magnetic phases, double perovskites can be superconducting. Partially melted ceramic material  $Sr_2YRu_{0.85}Cu_{0.15}O_6$ , shows superconductivity with an onset temperature of  $T_c \approx 45K$  [12, 13] at ambient pressure.

Let us start our discussion with a brief overview of the ferromagnets. We will consider insulators, since the metallic phase will be discussed in detail later.

### 1.3.1 Ferromagnetic insulating phase

In double perovskites  $A_2BB'O_6$ , each B and B' sits in an octahedral environment ( $BO_6$  and  $B'O_6$ ), due to which there is a crystal-field splitting of  $d$ -states of B and

Table 1.1: Ferromagnetic double perovskites

Material	Crystal structure	Magnetic order $T_c$	Transport property
$\text{Sr}_2\text{FeMoO}_6$	Tetragonal	420K	Half-metallic [14]
$\text{Ba}_2\text{FeMoO}_6$	Cubic	345K	Half-metallic [15]
$\text{Sr}_2\text{FeReO}_6$	Cubic	400K	Half-metallic [16, 17]
$\text{Sr}_2\text{CrReO}_6$	Cubic	635K	Half-metallic [18]
$\text{Ca}_2\text{CrReO}_6$	Monoclinic	360K	Insulating [18]
$\text{Ca}_2\text{FeReO}_6$	Monoclinic	520K	Insulating [17, 19]
$\text{La}_2\text{NiMnO}_6$	Monoclinic	280K	Insulating [20]

$B'$  into  $t_{2g}$  and  $e_g$  manifolds [21]. In  $\text{Ca}_2\text{FeReO}_6$  the small size of Ca induces monoclinic distortion in the structure, which further lifts the degeneracy of  $t_{2g}$  levels on the Re sites (with two  $t_{2g}$  electrons per Re). Due to this monoclinic distortion there is deviation of bond angle (Fe-O-Re) from  $180^\circ$  to  $\sim 156^\circ$ . This reduces the Re-Re overlap, by misaligning the  $t_{2g}$  orbitals. This bond-angle distortion reduces the effective d-electron hopping energy via the reduced hybridization between transition-metal  $d$  and oxygen  $p$  states, leading to the insulating character in  $\text{Ca}_2\text{FeReO}_6$  [17, 22].

$\text{La}_2\text{NiMnO}_6$  is an important member of this family, as it is a promising candidate for technological application. It has a ferromagnetic transition temperature  $T_c \sim 280\text{K}$  [20]. Here Mn-O-Ni superexchange interaction gives rise to ferromagnetism [23]. It shows magnetoresistance and magnetocapacitance effects [24], indicating a coupling between the magnetic, electronic, and dielectric properties, which can be controlled by the application of magnetic fields. The observation of such effects close to the room temperature makes it a strong candidate for practical spintronic applications.

### 1.3.2 Antiferromagnetic insulating phase

Double perovskites show antiferromagnetic insulating character for some combination of B and  $B'$ .  $\text{Sr}_2\text{FeWO}_6$  is one typical member of this family. It has antiferromagnetic transition temperature  $T_N \sim 40\text{K}$ , with  $\text{Fe}^{2+}$  ion in the high-

Table 1.2: Antiferromagnetic insulating double perovskites

Material	Crystal structure	Magnetic order $T_N$
$\text{Sr}_2\text{FeWO}_6$	Monoclinic	40K [25, 26]
$\text{Sr}_2\text{MnMoO}_6$	Tetragonal	13K [27, 28]
$\text{Sr}_2\text{NiMoO}_6$	Tetragonal	71.5K [29, 30]
$\text{Ca}_2\text{NiWO}_6$	Monoclinic	52.5K [31, 32]
$\text{Sr}_2\text{CoWO}_6$	Tetragonal	24K [33]
$\text{Sr}_2\text{YRuO}_6$	Monoclinic	26K [34]

spin state ( $S = 2$ ), and  $\text{W}^{6+}$  ion ( $5d^0$ ) in a non magnetic state. There is a large exchange splitting of the localised electrons at the Fe-site. Strong hybridisation between the W-5d and the O-2p states drives the hybridised states above the  $t_{2g} \downarrow$  level of Fe. The electron is transferred from the W-5d O-2p hybridised state to the Fe 3d level, leading to an insulating compound with formally  $\text{W}^{6+}$  and  $\text{Fe}^{2+}$  states. In absence of any delocalized electrons, the  $\text{Fe}^{2+}$  sites couple via superexchange to give rise to an antiferromagnetic insulator [26, 35]. The magnetic structure with a wave vector  $(0\ 1\ 1)$  can be described as a set of alternating ferromagnetic planes that are coupled antiferromagnetically [25] with each other.

### 1.3.3 Spin glass phase

The spin glass phase arises broadly either due to large B-site disorder (as in  $\text{Sr}_2\text{FeCoO}_6$ ) or due to geometric frustration (as in  $\text{Ba}_2\text{YMoO}_6$ ).

In  $\text{Sr}_2\text{FeCoO}_6$ , using neutron diffraction and subsequent bond valence sum analysis [10], it has been observed that the B site is randomly occupied by Fe and Co in the mixed valence states of  $\text{Fe}^{3+}/\text{Fe}^{4+}$  and  $\text{Co}^{3+}/\text{Co}^{4+}$ . Comparable ionic radii of the B-site cations (Fe and Co) lead to large B-site disorder in the sample. Due to randomly distributed B-site cations, there is a competition between nearest neighbor and next nearest neighbor superexchange interactions giving rise to the local magnetic frustration in the lattice. This magnetic frustration leads to spin glass behavior in  $\text{Sr}_2\text{FeCoO}_6$ .

In contrast,  $\text{Ba}_2\text{YMoO}_6$  crystallizes in face-centered cubic (FCC) lattice struc-

ture. In this compound Mo is in 5+ oxidation state ( $\text{Mo}^{5+}$ ,  $S = \frac{1}{2}$ ) with a singly occupied degenerate  $t_{2g}$  orbital in a cubic crystal field, while  $\text{Y}^{3+}$  ion does not carry a magnetic moment. The  $S = \frac{1}{2}$   $\text{Mo}^{5+}$  moments are located on an FCC lattice and coupled antiferromagnetically. This arrangement is geometrically frustrated, which in conjunction with quantum fluctuations gives rise to spin glass behavior in  $\text{Ba}_2\text{YMoO}_6$ . No magnetic order is observed down to 2K in ac and dc magnetic susceptibility, heat capacity, and muon spin rotation [11] experiments.

### 1.3.4 Ferromagnetic metallic phase

One way to classify the ferromagnetic double perovskites could be in terms of the nature of B and B'. One category would be those where only one of the ions is intrinsically magnetic, the other in which both are magnetic (both 3d elements, say). In the first category would be  $\text{Sr}_2\text{FeMoO}_6$ , while in the second would be  $\text{Sr}_2\text{FeReO}_6$ ,  $\text{Ca}_2\text{FeReO}_6$ , and  $\text{Sr}_2\text{CrReO}_6$ . Since our theoretical work is concerned with double perovskites in which only the B-site is magnetic, we will mainly concentrate on the properties of  $\text{Sr}_2\text{FeMoO}_6$ .

#### **$\text{Sr}_2\text{FeMoO}_6$**

Among the ferromagnetic double perovskites  $\text{Sr}_2\text{FeMoO}_6$  is the most studied due to the following electronic and magnetic properties [8].

- Large saturation moment.
- High ferromagnetic  $T_c \sim 420\text{K}$ .
- Large low field magnetoresistance.
- Half-metallic behavior.
- Non FM metallic phases on La doping.

This compound has surprisingly high ferromagnetic transition temperature  $T_c \sim 420\text{K}$ , indicating a large interatomic (Fe-Fe) exchange coupling. Using site-specific x-ray absorption spectroscopy with linearly polarized light, S. Ray *et al.* [36] have established that the formal valence of Fe in  $\text{Sr}_2\text{FeMoO}_6$  is 3+ ( $3d^5$ ).

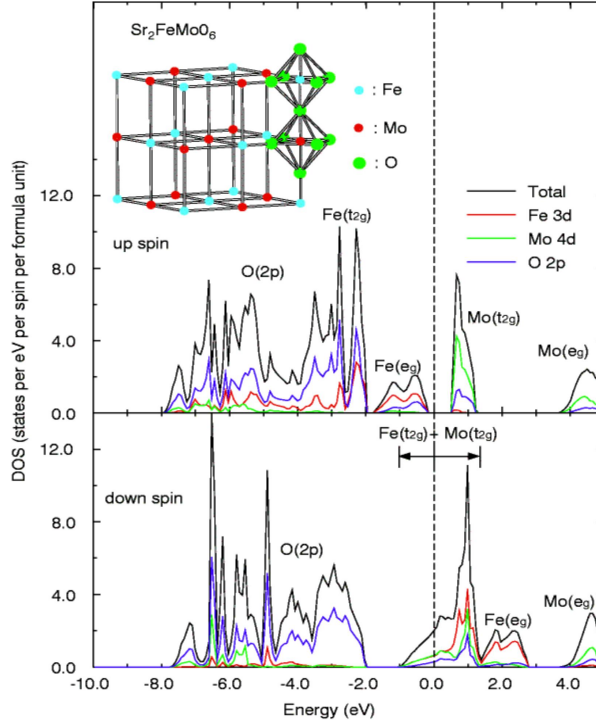


Figure 1.2: Density of states of  $\text{Sr}_2\text{FeMoO}_6$  using the density functional method. It shows the total density of states with majority *up* and minority *down* spins as well as the local density of states for the elements [9].

Detailed investigation of x-ray magnetic circular dichroism data confirms a large moment at the Fe site ( $S = \frac{5}{2}$ ). Mo has the oxidation state of  $5+$  ( $4d^1$ ). In this compound, each of the  $\text{Fe}^{3+}$  ( $S = \frac{5}{2}$ ) and  $\text{Mo}^{5+}$  ( $S = \frac{1}{2}$ ) sublattices are arranged ferromagnetically, while the two sublattices are coupled to each other antiferromagnetically.  $\text{Sr}_2\text{FeMoO}_6$  shows ferrimagnetic spin arrangement with  $4\mu_B$  ( $\frac{5}{2} - \frac{1}{2}$ ) magnetic moment per Fe-Mo unit, in the ideal ordered double perovskite structure.

### Density of states: $\text{Sr}_2\text{FeMoO}_6$

Kobayashi *et al.* [9] have calculated the electronic structure of this ordered perovskite by the density functional method, as shown in Figure 1.2. The ground state of this compound shows half-metallic nature; the density of states for the down-spin band is present at the Fermi level, whereas the up-spin band has a

gap at the Fermi level. The occupied up-spin band is mainly composed of Fe 3d electrons hybridized with oxygen 2p states (corresponding to the  $3d^5$  up-spin configuration) and much less of the Mo 4d electrons. The nominal Mo  $t_{2g}$  and  $e_g$  up-spin bands are above the Fermi level. By contrast, the down-spin band is mainly occupied by oxygen 2p states and the states around the Fermi level are shared by the Mo 4d  $t_{2g}$  and Fe 3d  $t_{2g}$  electrons, which are strongly hybridized with oxygen 2p states. Such a half-metallic nature gives rise to 100% spin-polarized charge carriers in the ground state. In view of the fairly high  $T_c$  and high spin polarization, ordered SFMO is suitable for spintronic applications.

### **Magnetoresistance: $Sr_2FeMoO_6$**

Kobayashi *et al.* [9] have shown that the ordered double perovskite  $Sr_2FeMoO_6$  exhibits pronounced negative magnetoresistance (Figure 1.3 ) at *lower* magnetic fields and *higher* temperatures compared to the doped manganites. The saturation magnetization at 4.2K is  $3\mu_B$  per formula unit. This small deviation from ideal value of  $4\mu_B$  is due to the mis-site-type imperfection of the B-site order, which was partly confirmed by the Rietveld analysis (giving 87% order on the B-site). The magnetization at 300K nearly saturates around  $2.2\mu_B$  per formula unit, indicating a high spin polarization (above 60%). The magnetoresistance magnitude at 7 T is as large as 42% and 10%, at 4.2K and 300K, respectively.

### **Resistivity: $Sr_2FeMoO_6$**

$Sr_2FeMoO_6$  is very sensitive to oxidation and its resistivity is strongly dominated by electron scattering at the grain boundaries. At high temperature (between 300K and 900K), when the oxygen atoms placed at the grain boundaries are removed, it undergoes two metal-insulator transitions. Below 405K, it is metallic and magnetically ordered, and above 590K it again shows metallic behavior [37]. However in the intermediate temperature range, the system presents a possible Anderson localization of the carriers with semiconducting behavior.

Upon application of high pressure, intrinsic negative magnetoresistance is unaffected in single crystals and gets suppressed in polycrystalline samples, particularly at low field [38]. Large pressure effects on the tunneling magnetoresistance

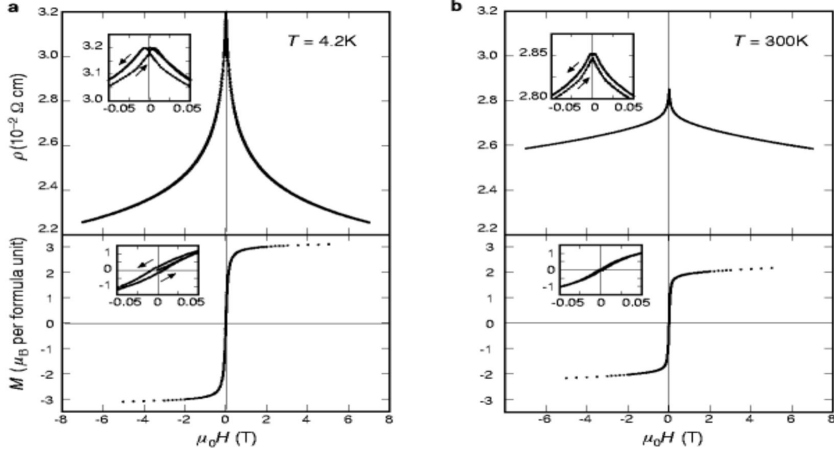


Figure 1.3: Isothermal magnetoresistance (upper panels) and magnetization  $M$  curves (lower panels) for polycrystalline ceramics of  $\text{Sr}_2\text{FeMoO}_6$ . (a) at 4.2K; (b) at 300K [9]. The insets show a magnification of the field- hysteretic magnetoresistance (upper panels) corresponding to the magnetic hysteresis (lower panels) in a low-field region.

originate from the spin-polarized tunneling at grain boundaries in the polycrystalline sample, in sharp contrast to the behavior for a single crystal. The connectivity between grains is enhanced by pressure to give rise to a suppression of the magnitude of the tunneling magnetoresistance.

### **$\text{Sr}_2\text{FeReO}_6$ : double moment ferrimagnet**

Contrary to a single magnetic moment present in  $\text{Sr}_2\text{FeMoO}_6$ , both B-sites possess a magnetic moment in  $\text{Sr}_2\text{FeReO}_6$ . Here, significant orbital moment of Re plays a crucial role in determining the magnetic properties.  $\text{Sr}_2\text{FeReO}_6$  bears a close resemblance to  $\text{Sr}_2\text{FeMoO}_6$  in terms of magnetic and transport properties.  $\text{Sr}_2\text{FeReO}_6$  has half-metallic ferrimagnetic magnetic ground state with a transition temperature  $\sim 400\text{K}$  [39]. Polycrystalline ceramics of  $\text{Sr}_2\text{FeReO}_6$  exhibits significant intergrain tunneling magnetoresistance even at room temperature (Figure 1.4). The magnitude of intergrain tunneling magnetoresistance with a magnetic field of 7 T at 4.2K and 300K is as large as 21% and 7%, respectively, reflecting high spin polarization of carriers.

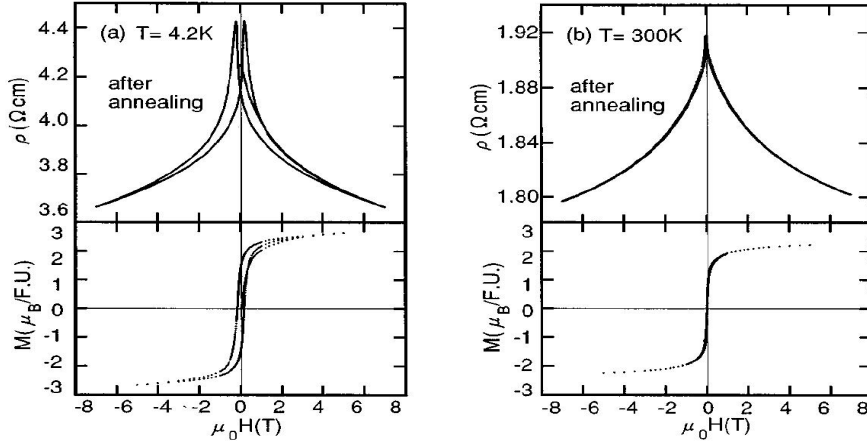


Figure 1.4: Isothermal magnetoresistance  $\rho(H)$  (upper panels) and magnetisation  $M$  curves (lower panels) for polycrystalline ceramics of  $\text{Sr}_2\text{FeReO}_6$  at 4.2K (a) and 300K (b) [39].

### **$\text{Ca}_2\text{FeReO}_6$ and $\text{Sr}_2\text{CrReO}_6$**

In the  $\text{A}_2\text{FeReO}_6$  series,  $\text{Ca}_2\text{FeReO}_6$  shows insulating behavior with the maximum  $T_c$  of 520K. Optical and x-ray absorption spectroscopy combined with density functional theory studies [40] have established the presence of subtle interplay of spin-orbit coupling, electron correlation, and lattice distortion in this compound.

In the  $\text{Sr}_2(\text{Fe}_{1-x}\text{Cr}_x)\text{ReO}_6$  series,  $\text{Sr}_2\text{CrReO}_6$  is nearly half-metallic with the maximum  $T_c$  of 625K, which is the highest  $T_c$  in an oxide compound without Fe. Re, being a 5d transition metal with substantially large spin moment, is expected to bear substantial spin-orbit coupling. Full-potential band-structure calculations including spin-orbit coupling [41] found that the magneto-optic spectra show substantially large Kerr rotations, suggesting potential application as read heads or optical data storage devices.

## **1.4 Impact of doping**

The properties of the parent double perovskites change significantly upon hole and electron doping. We will discuss this impact using the example of  $\text{Sr}_2\text{FeMoO}_6$ .

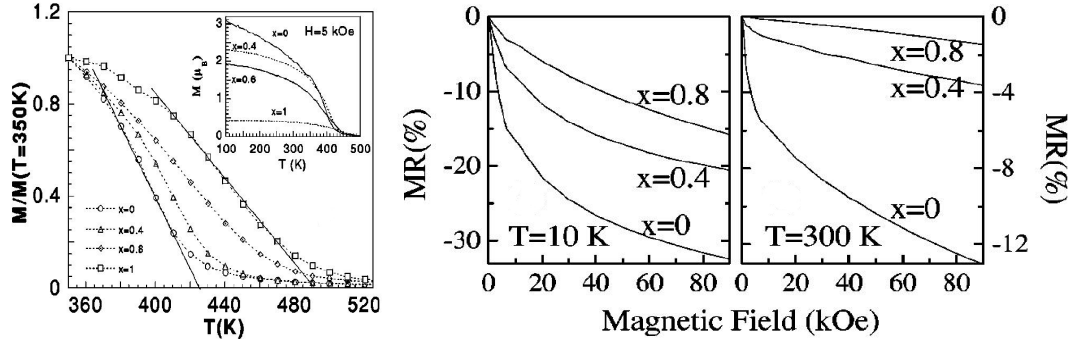


Figure 1.5: Left panel: reduced magnetization  $M(T, 5\text{kOe})/M(350\text{K}, 5\text{kOe})$  vs. temperature for  $\text{Sr}_{2-x}\text{La}_x\text{FeMoO}_6$  ( $x = 0, 0.4, 0.8,$  and  $1$ ) samples. Inset: Temperature-dependent magnetization. Right Panels: Field dependence of resistance  $\rho(H)/\rho(H=0)$  at  $10\text{K}$  and  $300\text{K}$  for  $x = 0, 0.4,$  and  $0.8$  samples [44].

### 1.4.1 Impact of hole doping

Upon partially substituting W for Mo in SFMO ( $\text{Sr}_2\text{FeMo}_x\text{W}_{1-x}\text{O}_6$ ), which is equivalent to hole doping, it shows a metal-insulator transition [42]. Compounds with  $1.0 \geq x \geq 0.3$  show metallic behavior, while for  $0.2 \geq x \geq 0$  they are insulating. All compounds with  $1.0 \geq x \geq 0.2$  are ferrimagnetic, while  $\text{Sr}_2\text{FeWO}_6$  ( $x = 0$ ) is antiferromagnetic with a Néel temperature  $T_N \approx 37\text{K}$  [43]. All samples with  $x \geq 0.3$  show a significant negative magnetoresistance.

### 1.4.2 Impact of electron doping

The properties of the ferromagnetic and metallic double perovskites  $\text{Sr}_2\text{FeMoO}_6$  change significantly upon electron doping, *i.e.*, substituting divalent Sr with trivalent La. Upon doping,  $T_c$  can rise upto  $70\text{K}$  above that of SFMO [44]. This is accompanied by a substantial reduction of the saturation magnetization, mainly due to increase in antisite disorder [45]. There is also a decrease in the magnetoresistance (Figure 1.5), which affects the functionality of the material. By analysing the magnetotransport data for different electron-doped double perovskites, D. Rubi *et al.* [46] argue that a gradual loss of spin polarization of the conduction electrons is responsible for the decrease in the magnetoresistance.

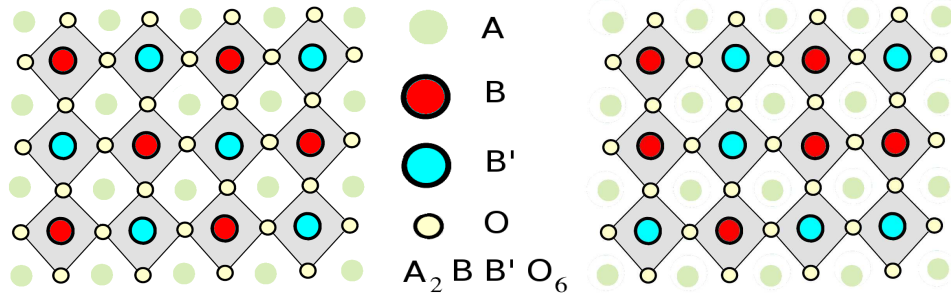


Figure 1.6: Two dimensional model of double perovskite. Left panel: ideal structure; right panel: random antisite disorder

### 1.4.3 Isoelectronic doping

If we dope  $\text{Sr}_2\text{FeMoO}_6$  with a small amount of Ba or Ca on the Sr sites, it increases the magnitude of magnetoresistance significantly [47]. There is drastic enhancement of low-field magnetoresistance in the Ba doping region with the optimization of low-field magnetoresistance at  $\text{Sr}_{0.4}\text{Ba}_{1.6}\text{FeMoO}_6$ . And Ca doped sample is optimized at  $\text{Sr}_{1.9}\text{Ca}_{0.1}\text{FeMoO}_6$ , which also has an enhanced ferrimagnetic transition temperature.

## 1.5 Antisite disorder

The promise of rich functionality in the double perovskites remains unfulfilled due to inevitable B, B' mislocation. The similar location of B and B' ions promotes tendency towards defect formation. In order to understand this disorder properly, let us consider a 2D version of  $\text{Sr}_2\text{FeMoO}_6$ , for ease of visualization. Ordered structure will refer to alternation of B and B' octahedra in each direction. By antisite disorder we mean replacing some B ion by B'. Thus, two similar octahedra (B-B or B'-B') will now be nearest neighbor, as shown in Figure 1.6 .

This interchange of B-B' ions in principle can happen in a random manner. However, as we will see in the next section, this antisite disorder is spatially correlated instead of being random. There will be locally ordered regions, phase slipped with respect to one another.

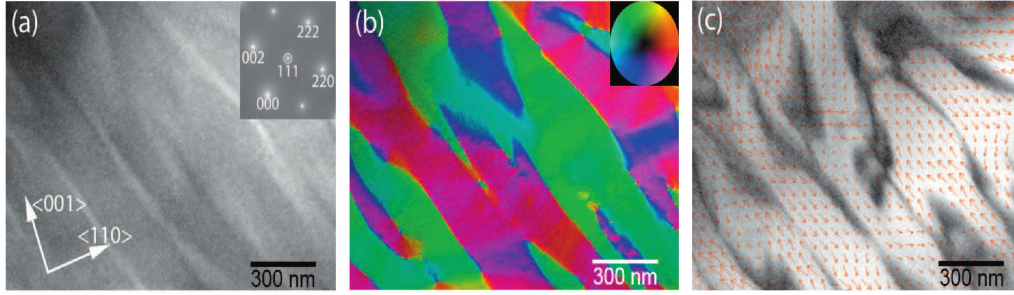


Figure 1.7: Magnetic and antiphase domain structures in  $\text{Ba}_2\text{FeMoO}_6$ . (a) Fresnel image: bright and dark lines represent magnetic domain walls. (b) Magnetisation distribution map derived by the transport-of-intensity equation method. (c) Dark lines and areas indicate the antiphase boundaries. The small red arrows represent local magnetisation [48].

### 1.5.1 Spatial nature of mislocation

In this section we will describe some of the experimental observation of the spatially correlated antisite disorder. Using transmission electron microscopy [48] of a single crystal of an ordered double perovskite  $\text{Ba}_2\text{FeMoO}_6$ , Asaka *et al.* (Figure 1.7) have established the presence of crystallographic domains, *i.e.*, regions having high degree of short range order. They have also investigated the relation between magnetic and crystallographic domains. Magnetic domain walls perfectly coincide with the crystallographic antiphase domain boundaries. Spins across a domain wall are antiferromagnetically aligned.

Similarly, using high-resolution electron microscopy (HREM) Navarro *et al.* [49] have studied  $\text{Sr}_2\text{FeMoO}_6$  ceramics samples (Figure 1.8 : left panel) and they have found the existence of antiphase domains. Using Fourier reconstruction, they have clearly established the presence of antiphase boundary in the sample. In the schematic illustration of the atomic structure at the antiphase boundary they have shown that two similar entities (either Fe-Fe or Mo-Mo) sit next to each other at the antiphase boundary.

In a separate study, using x-ray absorption fine structure in conjunction with synchrotron radiation x-ray diffraction, Meneghini *et al.* [50] have studied the nature of disorder in the polycrystalline double perovskite  $\text{Sr}_2\text{FeMoO}_6$ . Figure

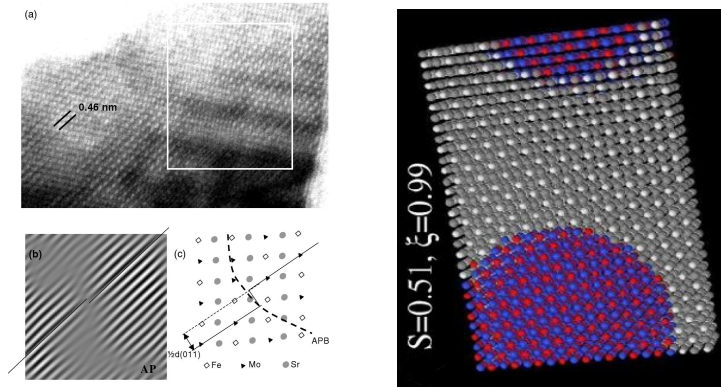


Figure 1.8: Left panel: (a) HREM image [49]: atomic structure, (b) Fourier reconstruction, clearly revealing an antiphase boundary (APB), (c) Schematic illustration of the atomic structure at the APB. Right panel : Slices of 3D models of Fe/Mo cubic lattices [50].

1.8 (right panel) shows a slice of 3D models of Fe/Mo cubic lattices, where light and dark grey sites represent Fe and Mo ordered positions, red (blue) sites being Fe (Mo) on the Mo (Fe) sublattice, with degree of long range order  $S = 0.51$  and large antiphase regions with degree of short range order  $\xi=0.99$ . Samples with varying degree of disorder reveal that a very high degree of short range order is preserved even in samples with highly reduced long range chemical order.

Overall, the experiments clearly establish the presence of antisite disorder and indicate that it is spatially correlated rather than being random. Hence, even though antisite disorder suppresses long range structural order, there is still a high degree of short range order that survives.

## 1.5.2 Impact on magnetisation

In double perovskites, we get correlated domains of locally ordered patches. At the antiphase boundary, we have two similar atoms (B-B or B'-B') sitting next to each other and inside a domain we have dissimilar neighboring atoms in all three directions. At antiphase boundary two spins have antiferromagnetic superexchange coupling which makes two neighboring domains antiparallel [49] (Figure. 1.9). Magnetic domain walls seems to perfectly coincide with the crystallographic

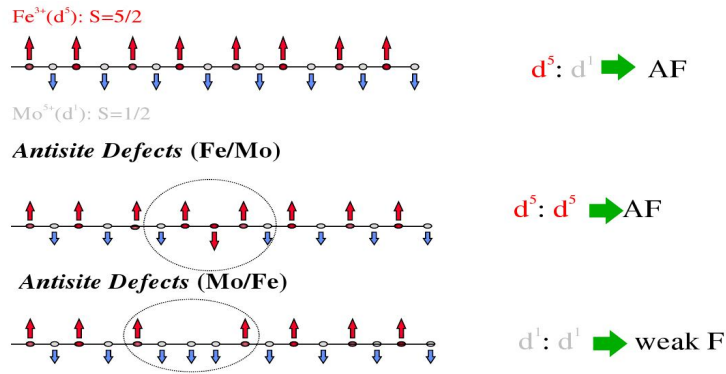


Figure 1.9: Schematic of magnetic coupling in disordered  $\text{Sr}_2\text{FeMoO}_6$  [49]. F/AF stands for ferromagnetic/antiferromagnetic interactions.

domain boundaries [48] (Figure 1.7).

In antisite disordered samples, bulk saturation magnetization reduces from  $4 \mu_B$  per formula unit, expected in the ordered case. Suppression in the saturation moment is large for the sample with large antisite disorder. The magnetic effects of antisite disorder are similar in both single crystals [14] and polycrystals [9, 51], shown in Figure 1.10 .

### 1.5.3 Impact on spin-polarisation

Ordered  $\text{Sr}_2\text{FeMoO}_6$  has a ferrimagnetic spin arrangement with large Hund's coupling on the magnetic (Fe) sites. Thus, only electrons oppositely oriented to the core magnetic ions will be able to conduct leading to a half-metallic state. In the correlated antisite disordered systems (Figure 1.7 ), magnetic domains coincide with the crystallographic antiphase domains [48]. Spins in the adjacent domains are oppositely oriented. Within each domain the conduction electron has only one spin polarisation at low temperature, but averaged over the system both up and down electrons have finite density of states at the Fermi level. A local probe with area smaller than typical domain size will allow only spin polarised tunneling, while a probe averaging over domains will see both spin polarisation. Thus, antisite disorder destroys the half-metallicity.

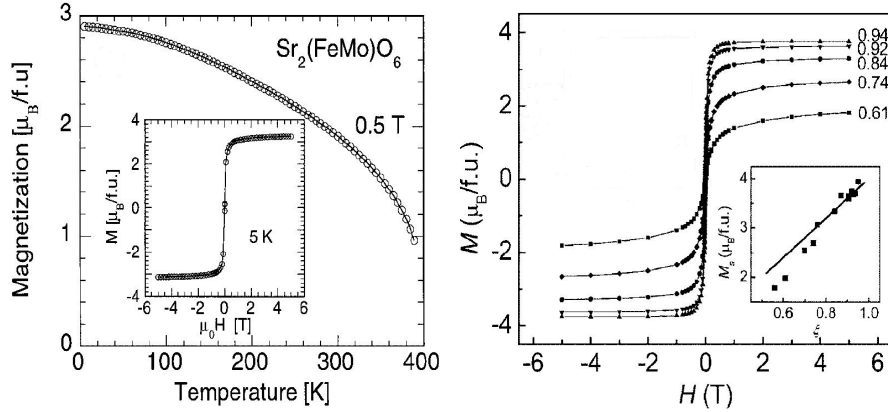


Figure 1.10: Left panel: Magnetisation of single crystals of  $\text{Sr}_2\text{FeMoO}_6$  [14] with 8% ASD taken at 0.5 T. Inset : Hysteresis curve at 5K. Right panel: Hysteresis loops at 5K of polycrystalline  $\text{Sr}_2\text{FeMoO}_6$  series [51]. Inset: Saturation magnetisation  $M_s$  at 5K with varying disorder. Line represents  $M_s/\xi = 4 \mu_B/\text{f.u.}$

## 1.5.4 Impact on transport properties

### Temperature dependence

Behavior of resistivity is widely different between single crystals and polycrystals as shown in Figure 1.11 . Let us start by discussing the impact of antisite disorder on transport of a single crystal. Single crystals [14] show residual resistivity  $\rho \sim 0.1 \text{ m}\Omega\text{cm}$ , and metallic behavior,  $d\rho/dT > 0$ . Unfortunately to best of our knowledge, systematic study of resistivity with varying degree of antisite disorder is not available.

On the contrary, polycrystalline samples have been studied for a wide range of antisite disorder [49, 51–55]. The transport in these materials is also affected by the grain boundary resistance. The residual resistivity in these samples [51] range from  $\sim 0.5 \text{ m}\Omega\text{cm}$  for low antisite disorder ( $M/M_{max} \sim 1.0$ ) to  $\sim 10 \text{ m}\Omega\text{cm}$  at high antisite disorder ( $M/M_{max} \sim 0.5$ ). Ordered polycrystals show  $d\rho/dT > 0$ , while less ordered ones show  $d\rho/dT < 0$  [51, 52].

Even in a single crystal, for a given fraction of mislocated sites, there can be widely varying degree of short range order. For example, the mislocated sites

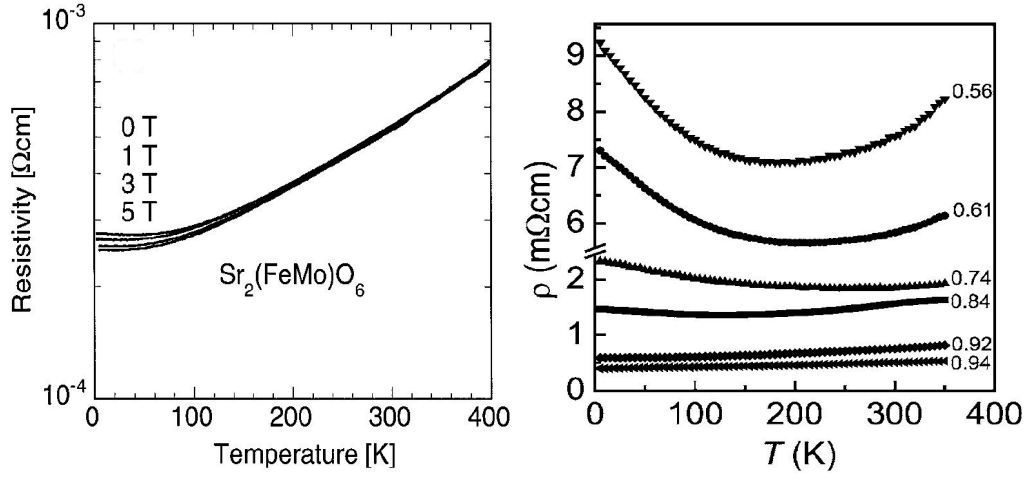


Figure 1.11: Temperature profiles of resistivity for  $\text{Sr}_2\text{FeMoO}_6$  samples. Left panel: Single crystals in several magnetic fields with 8% ASD [14]. Right panel: Polycrystals at zero-field with varying degree of disorder [51].

can arrange themselves in a few large domains or in many smaller domains. The degree of short range correlation would also affect the transport properties. There is no experiment yet which clarifies this issue. Grain boundary effects add to the complexity of the problem in polycrystalline samples. The effects of antisite disorder and grain boundaries on the resistance have not been deconvolved yet in polycrystalline samples.

### Magnetic field dependence

In a single crystal measurement Y. Tomioka *et al.* [14] (Figure 1.7) have measured the temperature profiles of resistivity in several magnetic field for single crystals of  $\text{Sr}_2\text{FeMoO}_6$  with 8% ASD. The magnetoresistance is weak ( $< 10\%$ ) at low temperature at a field of 5T. Unfortunately, magnetoresistance of single crystal with systematic variation of antisite disorder is not available.

For polycrystalline samples the grain boundary effect is also present, as we have seen above. The magnetoresistance can be large ( $\sim 40\%$ , Figure 1.12) at low temperature and at a field of 5T [52], and seems to be dominated by grain

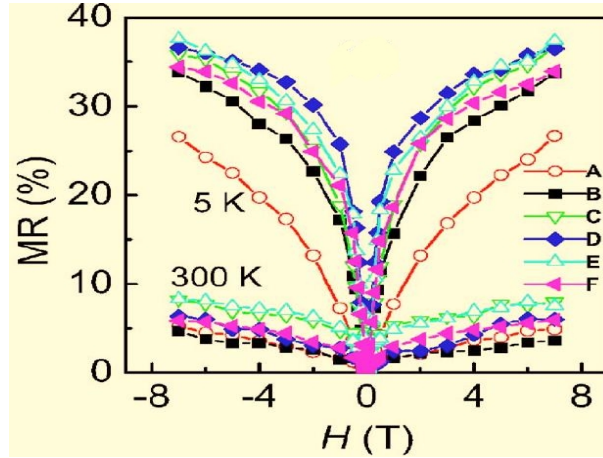


Figure 1.12: MR ratio as a function of applied field at 5K and 300K for the polycrystalline  $\text{Sr}_2\text{FeMoO}_6$  samples with decreasing disorder (A-F) [52].

boundary effects [54, 55]. Some results indicate a decrease [52] in magnetoresistance with increasing antisite disorder, while others show an increase [49]. Here again, effects of antisite disorder and grain boundaries on magnetoresistance have not been deconvolved yet.

## 1.6 Non-ferromagnetic metallic phases

In addition to the well known ferromagnetism, double perovskites are also expected to exhibit non-ferromagnetic order on sufficient electron doping, driven by electron delocalisation. Even *simple perovskite* transition metal oxides - the cuprates, manganites, or cobaltates, have a rich phase diagram [56], with a strong dependence on the doping level. The manganites, for instance, exhibit not just ferromagnetism, but also the CE-type magnetic order and A, C, and G type antiferromagnetic phases [57], depending on the hole doping level. Non-ferromagnetic phases have been predicted also for double perovskites using *ab initio* calculations with simple collinear arrangement of the *core spins* [58, 59].

Clear experimental indication of such antiferromagnetic order is limited, possibly because of increase in the antisite disorder with doping [44]. Samples have

indeed been synthesised with large La doping on  $\text{Sr}_2\text{FeMoO}_6$  [60, 61]. Low field magnetisation gets suppressed with increasing doping, which is an indication of increase in the disorder with doping (Figure 1.5). Using different magnetic and spectroscopic tools Jana *et al.* [61], have studied in detail the electronic and magnetic structures of  $\text{La}_x\text{Sr}_{2-x}\text{FeMoO}_6$  double perovskites with ( $1.0 \leq x \leq 1.5$ ). This reveals that the compound settles in an unusual antiferromagnetic metallic ground state for  $x \geq 1.4$ . The cross-over from ferromagnetic to antiferromagnetic behavior is largely dominated by the electronic changes, which establishes the role of kinetic energy driven mechanism [62].

There is unfortunately no detailed understanding of the role of antisite disorder in these samples yet, or data on resistivity and magnetoresistance.

# Bibliography

- [1] M. B. Salamon and M. Jaime, *Rev. Mod. Phys.* **73**, 583 (2001).
- [2] E. Dagotto, *Rev. Mod. Phys.* **66**, 763 (1994).
- [3] M. Imada, A. Fujimori, and Y. Tokura, *Rev. Mod. Phys.* **70**, 1039 (1998).
- [4] G. H. Jonker, and J. H. Van Santen, *Physica* **16**, 337 (1950).
- [5] A. Urushibara, Y. Moritomo, T. Arima, A. Asamitsu, G. Kido, and Y. Tokura, *Phys. Rev. B* **51**, 14103 (1995).
- [6] R. von Helmolt, J. Wecker, B. Holzappel, L. Schultz, and K. Samwer, *Phys. Rev. Lett.* **71**, 2331 (1993).
- [7] C. N. R. Rao and R. Mahesh, *Curr. Opin. Solid State Mater Sci.* **2**, 32 (1997); C. N. R. Rao and A. Arulraj, *Curr. Opin. Solid State Mater Sci.* **3**, 23 (1998); S. von Molnar and J. M. D. Coey, *Curr. Opin. Solid State Mater Sci.* **3**, 171 (1998).
- [8] For reviews, see D. D. Sarma, *Current Op. Solid State Mat. Sci.* **5**, 261 (2001); D. Serrate, J. M. de Teresa, and M. R. Ibarra, *J. Phys. Cond. Matt.* **19**, 023201 (2007).
- [9] K.-I. Kobayashi, T. Kimura, H. Sawada, K. Terakura, and Y. Tokura, *Nature* **395**, 677 (1998).
- [10] R. Pradheesh, H. S. Nair, C. M. N. Kumar, J. Lamsal, R. Nirmala, P. N. Santhosh, W. B. Yelon, S. K. Malik, V. Sankaranarayanan, and K. Sethupathi, *J. Appl. Phys.* **111**, 053905 (2012).

- [11] M. A. de Vries, A. C. Mclaughlin, and J.-W. G. Bos, Phys. Rev. Lett. **104**, 177202 (2010).
- [12] H. A. Blackstead, J. D. Dow, D. R. Harshman, W. B. Yelon, M. X. Chen, M. K. Wu, D. Y. Chen, F. Z. Chien, and D. B. Pulling, Phys. Rev. B **63**, 214412 (2001).
- [13] E. Galstyan, Y. Xue, M. Iliev, Y. Sun, and C.-Wu Chu, Phys. Rev. B **76**, 014501 (2007).
- [14] Y. Tomioka, T. Okuda, Y. Okimoto, R. Kumai, K.-I. Kobayashi, and Y. Tokura, Phys. Rev. B **61**, 422 (2000).
- [15] S. B. Kim, B. W. Lee, and C. S. Kim, Journal of Magnetism and Magnetic Materials **242-245 Part 2**, 747 (2002).
- [16] H. Kato, T. Okuda, Y. Okimoto, Y. Tomioka, K. Oikawa, T. Kamiyama, and Y. Tokura, Phys. Rev. B **69**, 184412 (2004).
- [17] J. Gopalakrishnan, A. Chattopadhyay, S. B. Ogale, T. Venkatesan, R. L. Greene, A. J. Millis, K. Ramesha, B. Hannoyer, and G. Marest, Phys. Rev. B **62**, 9538 (2000).
- [18] H. Kato, T. Okuda, Y. Okimoto, Y. Tomioka, Y. Takenoya, A. Ohkubo, M. Kawasaki, and Y. Tokura, Appl. Phys. Lett. **81**, 328 (2002).
- [19] W. Westerburg, O. Lang, C. Ritter, C. Felser, W. Tremel, and G. Jakob, Solid State Comm. **122**, 201 (2002).
- [20] R. I. Dass, J.-Q. Yan, and J. B. Goodenough, Phys. Rev. B **68**, 064415 (2003).
- [21] A. Chainani, M. Mathew, and D. D. Sarma, Phys. Rev. B **48**,14818 (1993); D. D. Sarma, N. Shanthi, and P. Mahadevan, Phys. Rev. B **54**, 1622 (1996).
- [22] H. Kato, T. Okuda, Y. Okimoto, Y. Tomioka, K. Oikawa, T. Kamiyama, and Y. Tokura, Phys. Rev. B **65**, 144404 (2002).

- [23] D. Haskel, G. Fabbris, N. M. Souza-Neto, M. van Veenendaal, G. Shen, A. E. Smith, and M. A. Subramanian, *Phys. Rev. B* **84**, 100403(R) (2011).
- [24] N. S. Rogado, J. Li, A. W. Sleight, and M. A. Subramanian, *Adv. Mater.* **17**, 2225 (2005).
- [25] A. K. Azad, S.-G. Eriksson, A. Møllergård, S. A. Ivanov, J. Eriksen, and H. Rundlöf, *Mat. Res. Bull.* **37**, 1797 (2002).
- [26] F. Bardelli, C. Meneghini, S. Mobilio, S. Ray, and D. D. Sarma, *J. Phys. Cond. Mat.* **21**, 195502 (2009).
- [27] A. K. Azad, S. Ivanov, S. -G. Eriksson, H. Rundlöf, J. Eriksen, R. Mathieu, and P. Svedlindh, *Journal of Magnetism and Magnetic Materials* **237**, 124 (2001).
- [28] M. Itoh, I. Ohta, and Y. Inaguma, *Mat. Sci. and Eng. B* **41**, 55 (1996).
- [29] L. Brixner, *J. Phys. Chem.* **64**, 165 (1960).
- [30] S. Nomura and T. Nakagawa, *J. Phys. Soc. Japan*, **21**, 1068 (1966).
- [31] C. A. López, J. Curiale, M. del C. Viola, J. C. Pedregosa, and R. D. Sánchez, *Physica B* **398**, 256 (2007).
- [32] M. J. Martínez-Lope, J. A. Alonso, M. T. Casais, and M. T. Fernández-Díaz, *Zeitschrift für Naturforschung. B* **58**, 127 (2003).
- [33] M. C. Viola, M. J. Martínez-Lope, J. A. Alonso, J. L. Martínez, J. M. De Paoli, S. Pagola, J. C. Pedregosa, M. T. Fernández-Díaz, and R. E. Carbonio, *Chem. Mater.* **15**, 1655 (2003).
- [34] P. D. Battle and W. J. Macklin, *J. Solid State Chem.* **52**, 138 (1984).
- [35] Z. Fang, K. Terakura, and J. Kanamori, *Phys. Rev. B* **63**, 180407(R) (2001).
- [36] S. Ray, A. Kumar, D. D. Sarma, R. Cimino, S. Turchini, S. Zennaro, and N. Zema, *Phys. Rev. Lett.* **87**, 097204 (2001).

- [37] D. Niebieskikwiat, R. D. Sanchez, A. Caneiro, L. Morales, M. Vasquez-Mansilla, F. Rivadulla, and L. E. Hueso, *Phys. Rev. B* **62**, 3340 (2000).
- [38] S. Kaji, G. Oomi, Y. Tomioka, and Y. Tokura, *Phys. Rev. B* **75**, 024430 (2007).
- [39] K.-I. Kobayashi, T. Kimura, Y. Tomioka, H. Sawada, and K. Terakura, Y. Tokura, *Phys. Rev. B* **59**, 11159 (1999).
- [40] B. C. Jeon, C. H. Kim, S. J. Moon, W. S. Choi, H. Jeong, Y. S. Lee, J. Yu, C. J. Won, J. H. Jung, N. Hur, and T. W. Noh, *J. Phys. Cond. Matt.* **22**, 345602 (2010).
- [41] H. Das, M. D. Raychaudhury, and T. Saha-Dasgupta, *Appl. Phys. Lett.* **92**, 201912 (2008).
- [42] S. Ray, A. Kumar, S. Majumdar, E. V. Sampathkumaran, and D. D. Sarma, *J. Phys. Cond. Matt.* **13**, 607 (2001).
- [43] H. Kawanaka, I. Hase, S. Toyama, and Y. Nishihara, *Physica B* **518**, 281 (2000).
- [44] J. Navarro, C. Frontera, Ll. Balcells, B. Martnez, and J. Fontcuberta, *Phys. Rev. B* **64**, 092411 (2001).
- [45] E. K. Hemery, G. V. M. Williams, and H. J. Trodahl, *Phys. Rev. B* **74**, 054423 (2006).
- [46] D. Rubi and J. Fontcuberta, *J. Phys. Cond. Matt.* **18**, 7991 (2006).
- [47] Bog-Gi Kim, Yew-San Hor, and S.-W. Cheong, *Appl. Phys. Lett.* **79**, 388 (2001).
- [48] T. Asaka, X. Z. Yu, Y. Tomioka, Y. Kaneko, T. Nagai, K. Kimoto, K. Ishizuka, Y. Tokura, and Y. Matsui, *Phys. Rev. B* **75**, 184440 (2007).
- [49] J. Navarro, L. Balcells, F. Sandiumenge, M. Bibes, A. Roig, B. Martnez, and J. Fontcuberta, *J. Phys. Cond. Matt.* **13**, 8481 (2001).

- [50] C. Meneghini, S. Ray, F. Liscio, F. Bardelli, S. Mobilio, and D. D. Sarma, Phys. Rev. Lett. **103**, 046403 (2009).
- [51] Y. H. Huang, M. Karppinen, H. Yamauchi, and J. B. Goodenough, Phys. Rev. B **73**, 104408 (2006).
- [52] Y. H. Huang, H. Yamauchi, and M. Karppinen, Phys. Rev. B **74**, 174418 (2006).
- [53] J. Navarro, J. Nogues, J. S. Munoz, and J. Fontcuberta, Phys. Rev. B **67**, 174416 (2003).
- [54] D. D. Sarma, S. Ray, K. Tanaka, M. Kobayashi, A. Fujimori, P. Sanyal, H. R. Krishnamurthy, and C. Dasgupta, Phys. Rev. Lett. **98**, 157205 (2007).
- [55] D. Niebieskikwiat, F. Prado, A. Caneiro, and R. D. Sanchez, Phys. Rev. B **70**, 132412 (2004).
- [56] E. Dagotto, Science **309**, 257 (2005).
- [57] Y. Tokura, Rep. Prog. Phys. **69**, 797 (2006).
- [58] P. Sanyal, H. Das, and T. Saha-Dasgupta, Phys. Rev. B **80**, 224412 (2009).
- [59] T. K. Mandal, C. Felser, M. Greenblatt, and J. Kuble, Phys. Rev. B **78**, 134431 (2008).
- [60] D. Sanchez, J. A. Alonso, M. Garcia-Hernandez, M. J. Martinez-Lopez, M. T. Casais, and J. L. Martinez, J. Mater. Chem. **13**, 1771 (2003).
- [61] S. Jana, C. Meneghini, P. Sanyal, S. Sarkar, T. Saha-Dasgupta, O. Karis, and S. Ray, arXiv: **1204.3378** (2012).
- [62] D. D. Sarma, P. Mahadevan, T. Saha-Dasgupta, S. Ray, and A. Kumar, Phys. Rev. Lett. **85**, 2549 (2000).

# Chapter 2

## Model and Method

**Chapter summary:** We start with a review of the past theoretical attempts to model the clean and antisite disordered double perovskites. We then describe the use of a *lattice gas* model for generating the structural motifs that mimic the correlated antisites in the experiments. The electronic-magnetic model is defined on this background and solved via a real space Monte Carlo technique. We end with a discussion of the method for transport calculation and extraction of the spin resolved density of states.

### 2.1 Past theoretical studies

Studies of the double perovskite family gathered momentum after the discovery by Kobayashi *et al.* [1] of large negative magnetoresistance in  $\text{Sr}_2\text{FeMoO}_6$  (SFMO) at high temperature and low magnetic field. This system has been studied using both density functional theory and the model Hamiltonian approach. Let us start with the discussion of the past work on *ordered* SFMO before moving on to the modeling of antisites.

#### 2.1.1 Ordered double perovskites

##### **Ab initio studies**

Using the density functional method, Kobayashi *et al.* [1] have calculated the electronic structure of SFMO, as shown in Figure 2.1. The ground state of SFMO is half-metallic; the down spin density of states is finite at the Fermi level, while

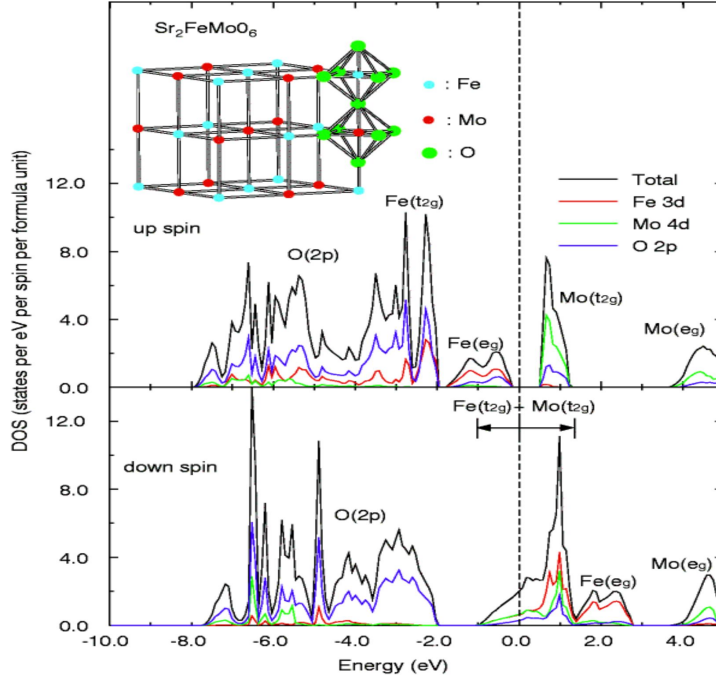


Figure 2.1: Density of states of  $\text{Sr}_2\text{FeMoO}_6$  using the density functional method. It shows the total density of states with majority *up* and minority *down* spins as well as the local density of states for the elements [1].

the up-spin band has a gap. The occupied up-spin band is mainly composed of Fe  $3d$  electrons hybridized with oxygen  $2p$  states (corresponding to the  $3d^5$  up-spin configuration) and much less of the Mo  $4d$  electrons. The nominal Mo  $t_{2g}$  and  $e_g$  up-spin bands are above the Fermi level. By contrast, the down-spin band is mainly occupied by oxygen  $2p$  states strongly mixed, around the Fermi level, with both the Mo  $4d$   $t_{2g}$  and Fe  $3d$   $t_{2g}$  states. In this compound  $\text{Fe}^{3+}$  ( $3d^5$ ,  $S = \frac{5}{2}$ ) and  $\text{Mo}^{5+}$  ( $4d^1$ ,  $S = \frac{1}{2}$ ) ions alternate along all three cubic axes. Ions within the Fe sublattice and the Mo sublattice are ferromagnetically coupled, while Fe and Mo have an effective antiferromagnetic coupling. This gives rise to the magnetization of  $4\mu_B$  ( $= \frac{5}{2} - \frac{1}{2}$ ) per Fe-Mo unit.

This ferrimagnetic spin ordering between the localised Fe electrons and the delocalised electrons presupposes a large spin splitting of the delocalised band, derived from the Mo  $d$  and oxygen  $p$ -states. Sarma *et al.* [2] have used a linear muffin-tin method with a generalized gradient approximation to propose a novel

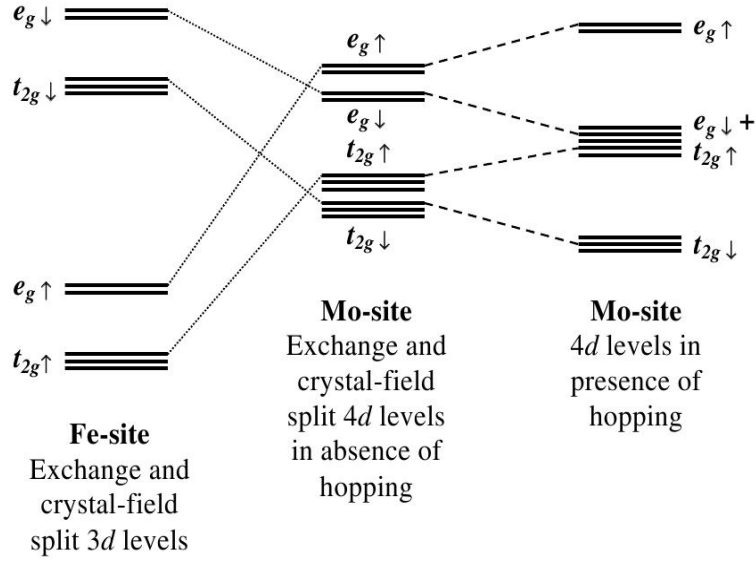


Figure 2.2: Energy level diagram expected at the Fe (left) and Mo (center) sites from an ionic picture. Energy levels at Mo are modified in the presence of Fe-Mo hopping interactions (right) [2].

mechanism for this order. The mechanism can be understood with the help of the schematics shown in the Figure 2.2, where only the relevant energy levels have been shown.

The  $\text{Fe}^{3+}$  ( $3d^5$ ) configuration is known to have a large exchange splitting of the  $d$  level in spin-up  $3d \uparrow$  and spin-down  $3d \downarrow$  states. In addition to this, there is crystal-field splitting of the  $3d$  levels into  $t_{2g}$  and  $e_g$  states in the octahedral symmetry of the Fe ions [3]; the crystal-field splitting in the case of  $\text{Fe}^{3+}$  is considerably smaller than the exchange splitting (left panel in Figure 2.2), while the situation is reversed for the Mo site (central panel in Figure 2.2). In presence of hopping interactions between the Fe states and the delocalised states derived from the Mo  $4d$ -O  $2p$  states, there is a finite coupling between the states of the same symmetry at the Fe and the Mo sites, leading to shifts in the bare energy levels. The delocalised  $t_{2g} \uparrow$  states gets pushed up and the  $t_{2g} \downarrow$  states gets pushed further down by hybridisation with the corresponding Fe states, as shown in the Figure 2.2. The opposite shifts of the up and down-spin conduction states, therefore, induce a spin-polarisation of the mobile electrons due to purely

hopping interactions between the localised electrons and the conduction states. This kinetic energy driven mechanism obviously leads to an antiferromagnetic coupling between the localised and the conduction electrons, since the energy is lowered by populating the down-spin conduction band with respect to the majority spin orientation of the localised electrons. There is a strong enhancement of the intra-atomic exchange strength at the Mo site, and an antiferromagnetic coupling between Fe and Mo sites [2].

### Model Hamiltonian studies

Theoretical attempts using the model Hamiltonian approach are based on the kinetically driven double exchange mechanism.

Using the model Hamiltonian approach, Phillips *et al.* [4] have analyzed the magnetic transition temperature and optical conductivity of double perovskites such as  $\text{Sr}_2\text{FeMoO}_6$ . The Hamiltonian describing the low-lying electronically active degrees of freedom consists of a tight-binding part arising from the band structure, an interaction part (Hund's coupling on the Fe site) and the Fe-Mo site energy difference. This Hamiltonian has been studied using the dynamical mean-field approximation. However, using parameters consistent with band calculations based local spin-density approximation the computed transition temperatures are lower than observed, and in particular decrease dramatically as band filling is increased, in contradiction to the experimental observation. There are no results on the non-ferromagnetic states that can emerge at high electron filling.

Brey *et al.* [5] have developed a mean-field theory for double perovskites *e.g.*,  $\text{Sr}_{2-x}\text{La}_x\text{FeMoO}_6$ , within a minimal effective model (similar model as above) including the strong Hund's coupling on the Fe sites and the kinetic energy of electron hopping between  $t_{2g}$  orbitals through the Mo sites. It gives a reasonable semiquantitative description of the observed Curie temperature in the double perovskites for the *undoped* ( $x = 0$ ) system. However, for the doped double perovskites ( $x \neq 0$ ), this mean-field theory predicts a decrease in the critical temperature with increase in the electron doping. They found that this double exchange-like model (i) stabilizes the ferromagnetic state, (ii) shows half-metallicity, and (iii) shows large saturation magnetization. However, it fails to

correctly describe the dependence of transition temperature on the band filling. This discrepancy can be corrected if we include the Hubbard interaction on the Mo sites. This widens the ferromagnetic window and brings the result in closer correspondence with experiments.

In a spin-wave analysis of an effective *Kondo-like* Hamiltonian, treated within the large-S expansion, Jackeli [6] has found that depending on the value of the carrier density, the ground state of double perovskite compounds is either a half-metallic ferrimagnet or a layered antiferromagnet. The transition to antiferromagnetic phase is first order, accompanied with a regime of phase separation.

### 2.1.2 Disordered double perovskites

The theoretical effort till now [7–11] has focused on uncorrelated antisite disorder, and quantified its impact on magnetic properties.

In a study Alonso *et al.* [7] have analyzed the magnetic phase diagram of the doped double perovskites of the type  $\text{Sr}_{2-x}\text{La}_x\text{FeMoO}_6$ , with uncorrelated antisite disorder. Their microscopic model has the usual couplings of the ordered double perovskite, with following modifications: (i) a strong antiferromagnetic coupling among the core Fe spins located next to each other and (ii) the kinetic energy corresponding to Fe-Fe hopping through oxygen orbitals, for nearest-neighbor Fe ions. The following phases emerge, Figure 2.3.

- The ferrimagnetic (FI) phase, where all Fe spins are parallel, and the spins of the electrons in the conduction band are antiparallel to the Fe spins,
- An AFM phase, where the Fe spins in neighboring (1,1,1) planes are antiparallel,
- A different ferrimagnetic (FIP) phase where the Fe spins are aligned ferromagnetically if the Fe ions are in the correct positions, and antiferromagnetically if the Fe ions occupy Mo sites.

Phase-separation regions are found between the FI and AFM phases as in upper panel, and between the FIP and AFM phases (middle and lower panel). Antisite disorder induces significant changes in the phase diagram. Antiferromagnetism at finite dopings is suppressed. The saturation magnetization in the FIP phase

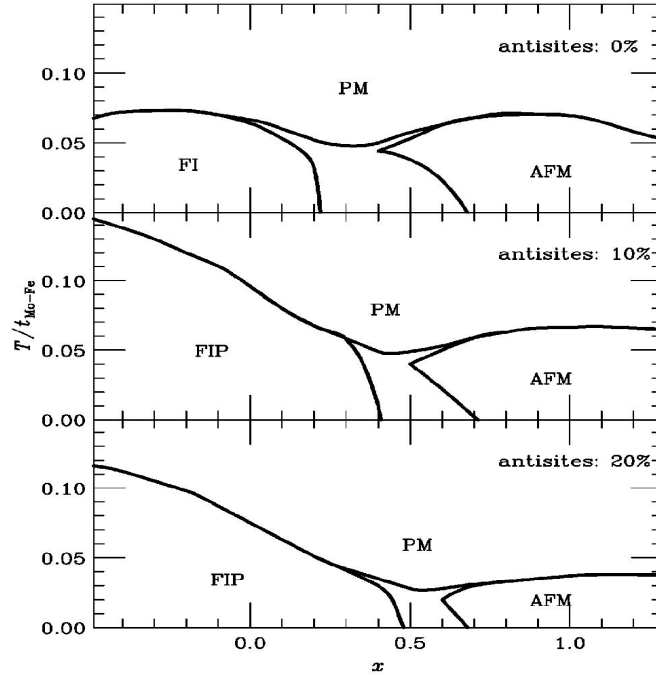


Figure 2.3: Phase diagram of  $\text{Sr}_{2-x}\text{La}_x\text{FeMoO}_6$  as function of  $x$  and temperature for different concentrations of antisite defects. Negative  $x$  means  $\text{Sr}_{2-|x|}\text{K}_{|x|}\text{FeMoO}_6$  [7].

is reduced, although the Curie temperature tends to increase with the number of Fe in Mo positions, due to the direct antiferromagnetic exchange between Fe ions which are nearest neighbors.

Frontera *et al.* [8] have used a classical spin model that takes into account the origin of the ferromagnetic interactions between Fe ions in  $\text{Sr}_2\text{FeMoO}_6$  double perovskites, and studied the critical properties. Using Monte Carlo simulation they have studied it for different amounts of antisite disorder. The model reproduces some of the experimental results found in these compounds (listed below).

- Reduction of the saturation magnetization and decrease in the susceptibility maximum with increase in antisite disorder.
- Systematic decrease of  $T_c$  with disorder.
- Critical properties have been studied and the critical exponents are consistent with experimental observations.

Although the model reproduces the experimental trend of  $T_c$  with disorder, it underestimates the broadening of the ferromagnetic transition with large antisite disorder. This could be a consequence of considering the random distribution of antisite disorder. In real systems there is a certain distribution (correlated) of antisite disorder concentration which leads to a distribution of  $T_c$ . This distribution of antisite concentration can also contribute to the loss of criticality, experimentally found at a large amount of disorder.

Apart from above studies, there are few other model Hamiltonian approaches [9–11], that have investigated the impact of antisite disorder in double perovskites. Allub *et al.* [9] have used renormalized perturbation expansion and studied how it affects density of states and determined the variation of the critical temperature in the low disorder regime. Aguilar *et al.* [10] have treated disorder within the dynamical mean-field approach, and studied how disorder affect density of states and spin polarization. Erten *et al.* [11] have a novel proposal whereby excess Fe can compensate for the loss of mobile carriers by La substitution on the Sr site. This should enhance  $T_c$  without sacrificing spin polarization.

All these calculations set the reference for magnetic properties, but have the limitation that:

1. they treat the antisites as randomly located,
2. they do not clarify the electronic properties,
3. localisation effects and MR remains unexplored.

## 2.2 Structural motif generation

Electronic properties (specially transport) are sensitive to the nature of disorder, particularly the presence of spatial correlations. To capture the correct electronic properties of double perovskite one has to first model this correlated antisite disorder. A model for double perovskites should incorporate the interplay of structural, electronic and magnetic variables.

We will first construct the correlated structural motif for double perovskite ( $A_2BB'O_6$ ) and define it via a variable  $\eta_i$ . Let us consider B as the *magnetic* ion

and B' as the *non-magnetic* one. We define the binary variable  $\eta_i$  such that  $\eta_i = 1$  when a site has a B ion, and  $\eta_i = 0$  when a site has a B' ion. Thus,  $\eta_i$  encode the atomic positions. On this structural motif, we set up the electronic-magnetic problem. The total Hamiltonian, including all degrees of freedom, would be:

$$H_{tot} = V_{at}\{\eta\} + H\{\eta\} \quad (2.1)$$

Here,  $V_{at}\{\eta\}$  represents the direct interaction between the ions (Lennard-Jones, say). There is also an *indirect* interaction via the electronic-magnetic degrees of freedom in  $H\{\eta\}$ . We do not enter into the detailed nature of  $H$  right now: we will do so later in this chapter. It basically involves electrons coupled to classical magnetic moments and moving in a background defined by  $\{\eta\}$ . If the atomic ordering problem is to be isolated from this, one should *trace out* the electronic and magnetic variables. The effective potential  $V_{eff}\{\eta\}$  controlling atomic order is

$$V_{eff}\{\eta\} = -\frac{1}{\beta} \log \int \mathcal{D}\mathbf{S}_i \text{Tr}_{\{f,m\}} e^{-\beta H_{tot}}$$

Computing  $V_{eff}$  and updating atomic positions accordingly is a computationally demanding task, the Monte Carlo (MC) equivalent of a Car-Parinello simulation. There is limited information about  $V_{at}$ , and the *trace* is technically difficult, so we construct a simple  $V_{eff}\{\eta\}$  that is consistent with the phenomenology, rather than attempt an elaborate *first principles* calculation.

Double perovskite have an inherent ordering tendency for B and B' atoms. The ideal structure is simply an alternation of B and B' ions along all three directions. However, in imperfectly annealed systems, there will be antisite defect regions where this ordering is reversed, and two B atoms or two B' atoms sit adjacent to each other. The ordering of the B-B' is in general neither perfect nor random, it is the result of an annealing process. While samples with high degree of order have been grown [12], indicating that the atomic order in the structural ground state should be perfect, recent experiments reveal an interesting trend in the degree of order as a function of annealing temperature.

In an experiment on  $\text{Sr}_2\text{FeMoO}_6$ , Sarma *et al.* [13] observed that there is a non-monotonic dependence of the degree of Fe-Mo ordering on the annealing temperature,  $T_{ann}$ , as shown in Figure 2.4. Different samples were taken from the same parent material (synthesised at high temperature and quenched to a low

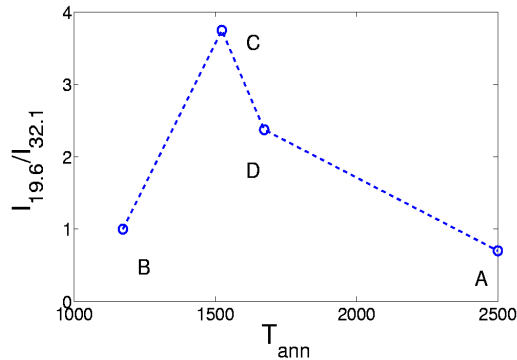


Figure 2.4: Experimental data for ordering vs annealing temperature (in Kelvin), obtained by Sarma *et al.* [13]. Y-axis shows the ratio of the XRD intensity of the supercell (101) reflection at  $19.6^\circ$ , to that of the normal reflection at  $32.1^\circ$ . This is a measure of the degree of ordering.

temperature), heated to a temperature  $T_{ann}$ , and annealed there for a duration  $\tau_{ann}$ , say.

If there is indeed a B-B' ordering tendency in the DPs, the extent of order *at equilibrium* would be highest at low  $T_{ann}$ , progressively falling off at higher  $T_{ann}$  where the order is expected to be small. The downturn at low annealing temperature is a consequence of insufficient equilibration. Our model below and results are based on the assumption that: (i) there is an intrinsic B-B' ordering tendency in the DPs, (ii) given long equilibration time, the DPs would indeed show a high degree of order at low  $T$ , but (iii) under typical synthesis conditions/annealing protocol the system only manages to generate correlated configurations with short range order. The annealing temperature and annealing time are therefore key to quantifying the structural order.

Since the structural (dis)order seems to be *frozen* at temperature,  $T \sim 1000\text{K}$ , much above the temperature for magnetic order ( $\sim 400\text{K}$ ), the qualitative issues in atomic ordering can be understood by ignoring the electronic-magnetic variables in an effective model, discussed below.

In the absence of detailed microscopic knowledge about  $V_{eff}\{\eta\}$ , we used a binary lattice gas model [14] that has the same ordering tendency as the real materials, *viz.*, B-B' alternation, or equivalently a *checkerboard* pattern. In terms

of the variables  $\eta_i$ , the simplest such model is :

$$V_{eff}\{\eta\} = V \sum_{\langle ij \rangle} \eta_i(1 - \eta_j) \quad (2.2)$$

with  $V > 0$  being a measure of the ordering tendency. The ground state in this model would correspond to  $\eta = 1, 0, 1, 0, \dots$  (B, B', B, B'...) along each axis. Notice that this approach tries to incorporate the effect of complex interactions between the A, B, B' and O ions (as also the electrons) into a single parameter.

Since one is interested in exploring the non-equilibrium effects due to poor annealing one has to use a Monte Carlo technique to anneal the  $\{\eta\}$  variables. Most of our studies involve a protocol where we start with a completely random B-B' configuration (as if quenched from very high T), and then anneal it at a temperature  $T_{ann}$ , for a MC run of duration  $\tau_{ann}$  Monte Carlo steps (MCS). Since the number of B and B' atoms is fixed we update our configurations by (i) moving to some site  $\mathbf{R}_i$ , (ii) attempting an *exchange* of the atom at  $\mathbf{R}_i$ , with another randomly picked within a box of size  $L_C^2$  centred on  $\mathbf{R}_i$ , and (iii) accepting or rejecting the move based on the Metropolis algorithm.

Even within this simple framework of lattice-gas type models, Sanyal *et al.* [14] were able to address several experimentally observed issues including non-monotonic dependence of the degree of order on annealing temperature [13], and the rapid decrease of order upon overdoping with either B or B' species.

In order to quantify the ordering tendency we have calculated the structure factor,  $S_{latt}(\mathbf{q})$ . We can imagine the B and B' system in terms of Ising spins. B is represented by an up-spin and B' by a down-spin. So, an ordered system is equivalent to an antiferromagnetic spin arrangement. The structure factor  $S_{latt}(\mathbf{q})$  of given spin configuration is calculated by

$$S_{latt}(\mathbf{q}) = \frac{1}{N^2} \sum_{i,j} S_i S_j e^{i\mathbf{q}\cdot(\mathbf{r}_i - \mathbf{r}_j)} \quad (2.3)$$

where N is the total number of atoms in the system. Here  $S_i$  represents the Ising *spin* at the i'th site with position vector  $\mathbf{r}_i$ . For the antiferromagnetic spin arrangement  $S_{latt}(\mathbf{q})|_{\mathbf{q}=(\pi,\pi)} = 1$ .

In systems with equal number of B and B' ions, where perfect order is in principle possible, one starts with a random initial configuration at some temperature

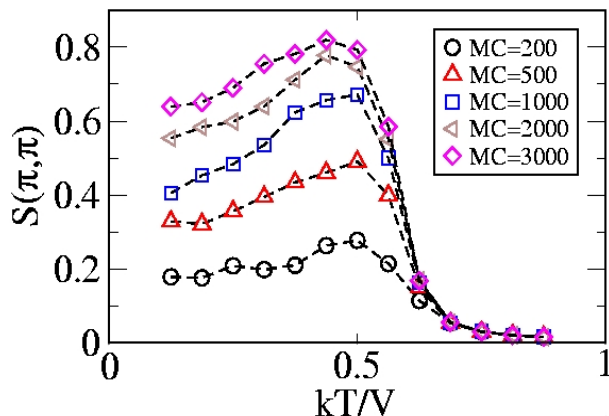


Figure 2.5:  $\pi - \pi$  structure factor vs annealing temperature for different annealing time for a  $20 \times 20$  lattice [14].

$T_{ann}$  and anneal for some time  $\tau_{ann}$ . The structure factor  $S_{latt}(\mathbf{q})$  at the ordering wavevector,  $\{\pi, \pi\}$ , is averaged over 40 such initial configurations. The extent of order, quantified by the peak in  $S_{latt}(\mathbf{q})$ , is shown in Figure 2.5 for a lattice size  $20 \times 20$ .

The non-monotonic behavior of  $S_{latt}(\pi, \pi)$  with  $T_{ann}$  that was observed in experiments shows up in the lattice gas simulation. The downturn in  $S_{latt}(\pi, \pi)$  at low  $T_{ann}$  is due to the inability of the system to achieve equilibrium at short annealing time, when one starts with a random initial configuration. With increasing annealing time there is an increase in the extent of order (for given  $T_{ann}$  and  $L$ ). There is a strong size dependence of the peak in  $S_{latt}(\pi, \pi)$ , varying almost by a factor of 4 between  $L = 20$  and  $L = 40$ . The origin of this strong size dependence becomes apparent when we examine a typical configuration (Figure 2.6) at low  $T_{ann}$ , generated by a short annealing run,  $\tau_{ann} = 500$  MCS.

This system has imperfect ordering as suggested by  $S_{latt}(\pi, \pi)$ . Actually this system consists of a few large ordered clusters with *phase slip* between them. Locally these domains are well ordered. The total  $S_{latt}(\pi, \pi)$  arises from the interfering contributions of large domains. This *cancellation* depends strongly on the system size  $L$ . In smaller systems,  $S_{latt}(\pi, \pi)$  is decided by the larger domain, and as domains proliferate with increasing  $L$ , there is an increasingly better cancellation between the out of phase domains, and hence  $S_{latt}(\pi, \pi)$  falls.

Using the method of Sanyal *et al.*, we have generated our antisite disordered

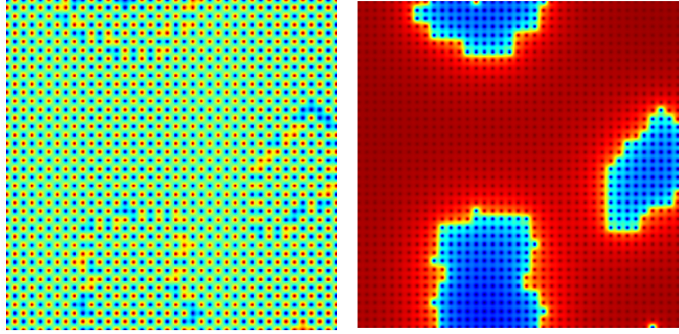


Figure 2.6: Left panel: Non-equilibrium B-B' configuration for  $T_{ann}/V=1.2$  and  $\tau_{ann} = 500$ , on a  $40 \times 40$  lattice; Right panel: We have plotted  $g(\mathbf{r}_i) = (\eta_i - \frac{1}{2})e^{i\pi(x_i+y_i)}$ . For a perfectly ordered structure  $g(\mathbf{R}_i)$  is constant ( $= \frac{1}{2}$ ), shown by red dots. Those regions which are displaced with respect to the ordered structure has value  $-\frac{1}{2}$ , shown by blue dots.

configurations. Although we have studied both 2D and 3D situations we will mostly concentrate on 2D, since it allows access to large sizes and is easier to visualise. Since the actual *defects* are at the interface of two ordered (but phase slipped) clusters, we will show the domains and domain walls, rather than the detailed atomic configuration.

Below an ordering temperature  $T_{ord} \sim 0.7V$  (in 2D) the model exhibits long range B-B' order provided one anneals long enough. We quench the system from high temperature (random B, B') to  $T_{ann} < T_{ord}$  (so that the net order is non zero), but deliberately annealed it for a short time, preventing equilibration. We have chosen four families (Figure 2.7) with increasing disorder generated via successively poorer annealing of the lattice-gas model, to study the electronic properties.

## 2.3 Quantifying antisite disorder

One can variously characterise the B-B' structures that emerge. To keep a correspondence with recent experimental work [15]. we use the following indicators:

1. The fraction,  $x$ , of B (or B') atoms that are on the wrong sublattice. The

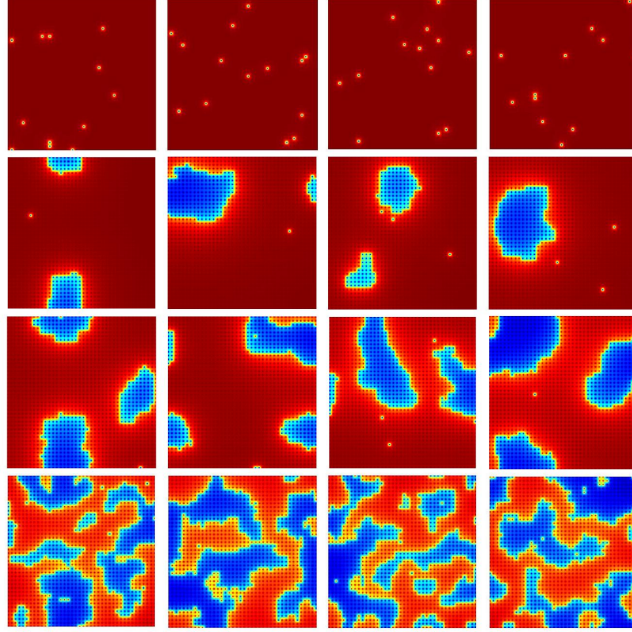


Figure 2.7: Four families of antisite disordered configurations (top to bottom) generated via successively poorer annealing of the lattice gas model. We plot  $g(\mathbf{r}_i) = (\eta_i - \frac{1}{2})e^{i\pi(x_i+y_i)}$ . The patterns along a row are different realisations of ASD within each family. The average structural order parameter (see next section) has values  $S = 0.98, 0.76, 0.50$  and  $0.08$  as we move from top to bottom. Lattice size  $40 \times 40$ .

structural *order parameter*  $S = (1 - 2x)$ .

2. The degree of short range order, characterised by the probability  $p$ , of having nearest neighbor pairs that are B-B'. In a perfectly ordered sample this would be 1 (the B and B' alternate), while in a completely disordered sample this is 0.5. For an uncorrelated B, B' distribution this would be  $p = p_{uncorr} = x^2 + (1 - x)^2 = \frac{1}{2}(1 + S^2)$ . The two terms,  $x^2$  and  $(1 - x)^2$ , arise from having both atoms on the *wrong* sublattice or *right* sublattice respectively. For us  $p > p_{uncorr}$ .
3. The correlation length  $\xi$  associated with the domain structures is inferred from a Lorentzian fit to the B-B' structure factor of the form

$$S_{latt}(\mathbf{q}) \sim \frac{\xi^{-1}}{(q_x - \pi)^2 + (q_y - \pi)^2 + \xi^{-2}}$$

For our study we have chosen four families with increasing disorder, as shown in Figure 2.7. These families have a fraction of mislocated sites:  $x = 0.01, 0.12, 0.25, 0.46$ . The patterns, however, are strongly correlated. Even in the most disordered samples (lowest row in Figure 2.7) where the likelihood of any site being B or B' is  $\sim 0.5$ , if a site is B, say, there is a high likelihood that its neighbors will be B' (and vice versa). While  $p = p_{uncorr} = 0.98, 0.79, 0.63, 0.50$ , the values that actually emerge from our correlated patterns, are  $p_{corr} \sim 0.98, 0.97, 0.95, 0.86$ . Even the most disordered samples have a high degree of short range order. A Lorentzian fit to the B-B' structure factor yields,  $\xi \sim 6.6, 5.9, 4.8, 3.6$ .

The disorder in these systems should be characterised in terms of *two variables*:  $S$ , which is a gross measure of order, and  $p$  (or  $\xi$ ) which quantify short range correlation. In general, *physical properties would depend on both  $S$  and  $p$*  and not simply on  $S$ .

## 2.4 Electronic Hamiltonian

For any specified  $\{\eta\}$  background the electronic-magnetic model has the form

$$H = H_{loc}\{\eta\} + H_{kin}\{\eta\} + H_{mag}\{\eta\} - h \sum_i S_{iz} - \mu \hat{N} \quad (2.4)$$

Where

$$\begin{aligned} H_{loc}\{\eta\} &= \epsilon_B \sum_{i,\sigma} \eta_i f_{i\sigma}^\dagger f_{i\sigma} + \epsilon_{B'} \sum_{i,\sigma} (1 - \eta_i) m_{i\sigma}^\dagger m_{i\sigma} \\ H_{kin}\{\eta\} &= -t_1 \sum_{\langle ij \rangle, \sigma} \eta_i \eta_j f_{i\sigma}^\dagger f_{j\sigma} - t_2 \sum_{\langle ij \rangle, \sigma} (1 - \eta_i)(1 - \eta_j) m_{i\sigma}^\dagger m_{j\sigma} \\ &\quad - t_3 \sum_{\langle ij \rangle, \sigma} (\eta_i + \eta_j - 2\eta_i \eta_j) (f_{i\sigma}^\dagger m_{j\sigma} + h.c.) \\ H_{mag}\{\eta\} &= J \sum_{i,\alpha\beta} \eta_i \mathbf{S}_i \cdot f_{i\alpha}^\dagger \vec{\sigma}_{\alpha\beta} f_{i\beta} + J_{AF} \sum_{\langle ij \rangle} \eta_i \eta_j \mathbf{S}_i \cdot \mathbf{S}_j \end{aligned}$$

Here,  $H_{loc}$  is the onsite term with  $\epsilon_B$  and  $\epsilon_{B'}$  as the level energies, respectively, at the B and B' sites,  $\Delta = \epsilon_B - \epsilon_{B'}$  is the *charge transfer* energy. For the present study we have set [16] the *effective* charge transfer energy  $\epsilon_B - J/2 - \epsilon_{B'} = 0$ .  $f$  is the electron operator referring to B site and  $m$  is that of B' site.  $H_{kin}$  is the nearest neighbor (NN) hopping term. For simplicity, we set all the NN

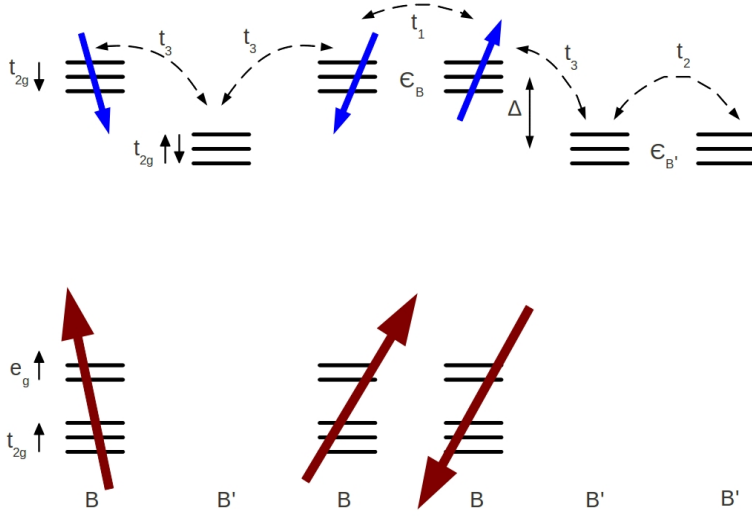


Figure 2.8: Schematic diagram showing the parameters of the model for the antiferromagnetic disordered double perovskite in the paramagnetic state. B site has a large localized core spin, treated as classical spins within our model.

hopping amplitudes to be same  $t_1=t_2=t_3=t$ .  $H_{mag}$  is magnetic interaction term which consists of the Hund's coupling  $J$  on B sites, and the AFM superexchange coupling  $J_{AF}$  between two NN magnetic B sites. Thus, our microscopic model has usual couplings of ordered double perovskite and antiferromagnetic coupling, when two B ions are nearest neighbor. Here,  $\mathbf{S}_i$  is the classical core spin on the B site at  $\mathbf{r}_i$  with  $|\mathbf{S}_i| = 1$ . We have taken  $J/t \gg 1$  with  $J > 0$ . When the *up spin* core levels are fully filled, as for Fe in  $\text{Sr}_2\text{FeMoO}_6$ , the conduction electron is forced to be *antiparallel* to the core spin. We have used  $J > 0$  to model this situation.

Much of the physics of these materials arises from the competition between delocalisation driven ferromagnetic exchange and B-B antiferromagnetic superexchange. We set  $J_{AF}S^2/t = 0.08$ , based on the  $T_N$  scale in  $\text{SrFeO}_3$ .  $h$  is an applied magnetic field in the  $\hat{z}$  direction. The chemical potential  $\mu$  is used to control the electron density, and  $\hat{N}$  is the total electron density operator. We have ignored the next nearest neighbor hopping and orbital degeneracy.

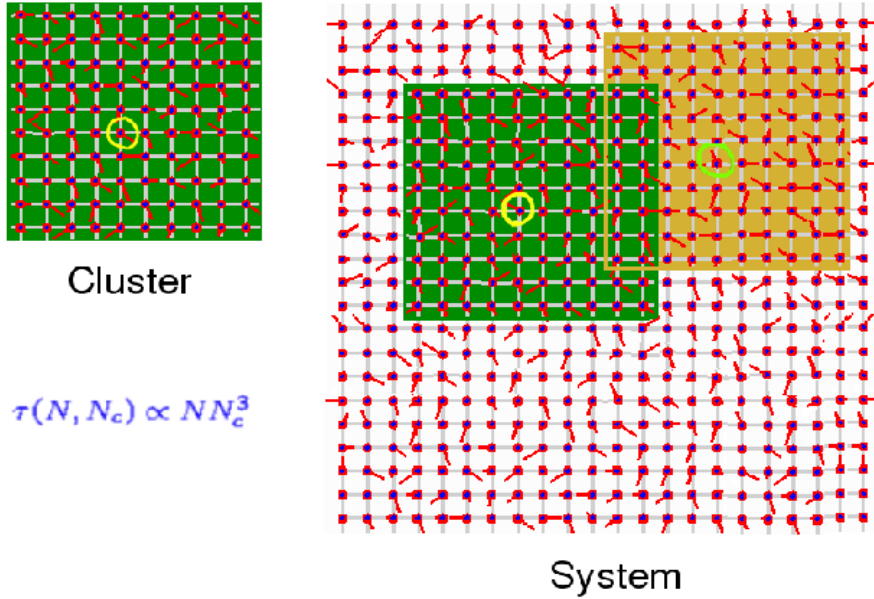


Figure 2.9: Travelling Cluster Approximation schematic

## 2.5 Monte Carlo method

For a given  $\{\eta_i\}$  configuration we need to solve for the magnetic and electronic properties. Since the background involves strong disorder, and the electron-spin coupling,  $J$ , is large, we use an exact diagonalization based Monte Carlo technique. This uses the Metropolis algorithm where a spin update,  $\mathbf{S}_i \rightarrow \mathbf{S}'_i$  is accepted or rejected depending on  $\Delta E/k_B T$ , where  $\Delta E = E(\mathbf{S}'_i) - E(\mathbf{S}_i)$ . In principle, we should diagonalise the full system every time an update is attempted. The cost, for a large system, is prohibitive. In order to access large system sizes, we have augmented it by a *travelling cluster* (TCA) [17] Monte Carlo technique, where we diagonalize the cluster Hamiltonian built around the update site. We update a spin using Monte Carlo scheme employing Metropolis algorithm.

Normally one iteratively diagonalises the full Hamiltonian for a system of  $N$  sites with computation time  $\tau_N \sim N^4$ . This limits achievable sizes to  $N \sim 100$ . In TCA, the energy cost of a MC update is computed from the Hamiltonian of a cluster, of size  $N_c$ , constructed around the reference site, and embedded in the larger system. In TCA,  $\tau_N \sim NN_c^3$ . Cost of simulation decreases significantly, hence we can access larger system size. Our results are obviously exact when

$N_c = N$ , and converge quickly to this asymptote with increasing  $N_c$ . Accuracy improves in systems where the effective disorder seen by the fermions is large, i.e., where the fermion wave-functions are more localized. Electronic properties are calculated after equilibration by diagonalizing the *full system*.

## 2.6 Transport and spin-resolved density of states

### 2.6.1 Transport

In the linear response regime, the Kubo formula can be used to calculate the conductivity of a system. The general expression [18], involving matrix elements between many body states, simplifies significantly for non-interacting systems. This *Kubo-Greenwood* result can be computed purely in terms of single particle eigenfunctions and energies. For disordered non-interacting systems, the Kubo formula [19], at  $T=0$  is:

$$\sigma(\omega) = \frac{A}{N} \sum_{\alpha,\beta} (n_\alpha - n_\beta) \frac{|f_{\alpha\beta}|^2}{\epsilon_\beta - \epsilon_\alpha} \delta(\omega - (\epsilon_\beta - \epsilon_\alpha)) \quad (2.5)$$

where the constant  $A = \pi e^2 / \hbar a_0$ ,  $a_0$  is the lattice spacing, and the occupation factor  $n_\alpha = \theta(\mu - \epsilon_\alpha)$ . Here  $f_{\alpha\beta} = \langle \psi_\alpha | \hat{j}_x | \psi_\beta \rangle$  are matrix element of current operator  $\hat{j}_x$  between exact single particle eigenstates  $|\psi_\alpha\rangle, |\psi_\beta\rangle$  etc., for a given realisation of disorder and  $\epsilon_\alpha, \epsilon_\beta$  etc., are corresponding eigenvalues. The current operator for the tight-binding model is given by  $\hat{j}_x = it \sum_{i,\sigma} (c_{i+xa_0,\sigma}^\dagger c_{i,\sigma} - c_{i,\sigma}^\dagger c_{i+xa_0,\sigma})$ .

The conductivity defined above is prior to the disorder averaging. Notice that the  $\delta$ -function constraint cannot be satisfied for arbitrary frequency in a finite system. So we can neither calculate the dc conductivity,  $\sigma_{dc}$  directly, nor estimate  $\sigma(\omega)$  at some arbitrary externally specified frequency. However, we can still calculate the *average conductivity* over a frequency interval  $\Delta\omega$  and calculate  $\sigma_{dc}$  using following strategy. The average of  $\sigma(\omega)$  over the interval  $[0, \Delta\omega]$  (dc conductivity) is defined as

$$\sigma_{av}(\Delta\omega, \mu, N) = \frac{1}{\Delta\omega} \int_0^{\Delta\omega} \sigma(\omega, \mu, N) d\omega \quad (2.6)$$

$\Delta\omega$  can be set independent of  $N$ , but we will relate them by fixing  $\Delta\omega = B/N$ , where  $B$  is a constant fixed by setting  $\Delta\omega=0.04$  for  $N = 1000$ . The mean finite size

gap is  $12/1000 \sim 0.01$ , in 3D, much smaller than  $\Delta\omega$ . The chemical potential  $\mu$  is set to target the required electron density  $n$ .  $\sigma_{av}$  is averaged over  $N_r$  realisations of disorder, to generate  $\bar{\sigma}_{av}(\Delta\omega, \mu, N)$ . The *noise* in  $\bar{\sigma}_{av}(\Delta\omega, \mu, N)$  falls slowly, as  $1/\sqrt{N_r}$ .

## 2.6.2 Spin resolved density of states

$D_{dos}^\sigma$  is calculated using following expression

$$D_{dos}^\sigma(\omega) = -\frac{1}{\pi} \text{Im} (G_{ii}^{\sigma\sigma}(\omega)) \quad (2.7)$$

where  $G_{ii}^{\sigma\sigma}(\omega)$  is the Fourier transform of retarded Green's function (written below) with respect to time.

$$G_{ii}^{\sigma\sigma}(t) = -i\theta(t) \langle \Omega | [c_{i\sigma}(t), c_{i\sigma}^\dagger(t)]_+ | \Omega \rangle \quad (2.8)$$

On simplification, the above expression for spin resolved density of states reduces to

$$D_{dos}^\sigma(\omega) = \sum_m |{}_N \langle \Omega | c_{i\sigma} | m \rangle_{N+1}|^2 \delta(\omega + E_0 - E_{N+1}^m) \\ + \sum_n |{}_N \langle \Omega | c_{i\sigma}^\dagger | n \rangle_{N-1}|^2 \delta(\omega - E_0 + E_{N-1}^n)$$

where  $|\Omega\rangle_N$  is  $N$ -particle ground state of the system with eigenvalue  $E_0$ , whereas  $|m\rangle_{N+1}$  and  $|n\rangle_{N-1}$  represents all  $(N+1)$  and  $(N-1)$ -particle states of the system with energy  $E_{N+1}^m$  and  $E_{N-1}^n$  respectively. Instead of calculating  $D_{dos}^\sigma(\omega)$  in real space basis, we go to the eigenbasis of the system and write  $c_{i\sigma}^\dagger$  and  $c_{i\sigma}$  operators in terms of operators that corresponds to the eigenbasis of single particle Hamiltonian.

# Bibliography

- [1] K.-I. Kobayashi, T. Kimura, H. Sawada, K. Terakura, and Y. Tokura, *Nature* **395**, 677 (1998).
- [2] D. D. Sarma, P. Mahadevan, T. Saha-Dasgupta, S. Ray, and A. Kumar, *Phys. Rev. Lett.* **85**, 2549 (2000).
- [3] A. Chainani, M. Mathew, and D. D. Sarma, *Phys. Rev. B* **48**,14818 (1993);  
D. D. Sarma, N. Shanthi, and P. Mahadevan, *Phys. Rev. B* **54**, 1622 (1996).
- [4] K. Phillips, A. Chattopadhyay, and A. J. Millis, *Phys. Rev. B* **67**, 125119 (2003).
- [5] L. Brey, M. J. Calderón, S. D. Sarma, and F. Guinea, *Phys. Rev. B* **74**, 094429 (2006).
- [6] G. Jackeli, *Phys. Rev. B* **68**, 092401 (2003).
- [7] J. L. Alonso, L. A. Fernandez, F. Guinea, F. Lesmes, and V. Martin-Mayor, *Phys. Rev. B* **67**, 214423 (2003).
- [8] C. Frontera and J. Fontcuberta, *Phys. Rev. B* **69**, 014406 (2004).
- [9] R. Allub, O. Navarro, M. Avignon and B. Alascio, *Physica B* **320**, 13 (2002).
- [10] B. Aguilar, O. Navarro and M. Avignon, *Eur. Phys. Lett.* **88**, 67003 (2009).
- [11] O. Erten, O. N. Meetei, A. Mukherjee, M. Randeria, N. Trivedi, and P. Woodward, *Phys. Rev. Lett.* **107**, 257201 (2011).
- [12] K.-I. Kobayashi, T. Kimura, H. Sawada, K. Terakura and Y. Tokura, *Nature* **395**, 677 (1998).

- [13] D. D. Sarma, S. Ray, K. Tanaka, M. Kobayashi, A. Fujimori, P. Sanyal, H. R. Krishnamurthy, and C. Dasgupta, Phys. Rev. Lett. **98**, 157205 (2007).
- [14] P. Sanyal, S. Tarat, and P. Majumdar, Eur. Phys. J. B **65**, 39 (2008).
- [15] C. Meneghini, S. Ray, F. Liscio, F. Bardelli, S. Mobilio, and D. D. Sarma, Phys. Rev. Lett. **103**, 046403 (2009).
- [16] In SFMO  $(\epsilon_B - J/2) - \epsilon_{B'} \sim 5t$ , and we have checked that this B, B' energy mismatch mainly serves to enhance the resistivity without affecting the trends we observe.
- [17] S. Kumar and P. Majumdar, Eur. Phys. J. B **50**, 571 (2006).
- [18] G. D. Mahan, Quantum Many Particle Physics (Plenum Press, New York) (1990).
- [19] S. Kumar and P. Majumdar, Eur. Phys. J. B **46**, 237 (2005).

# Chapter 3

## Impact of Antisite Disorder on the Ferromagnetic Phase

**Chapter summary:** This chapter presents our results on the impact of antisite disorder on the ferromagnetic phase. For antisite disorder with a high degree of short-range correlation, the antiphase boundaries also act as magnetic domain walls. Increasing antisite disorder reduces the low-field magnetisation, destroys half-metallicity, and finally makes the ground state insulating. While these are disadvantages, we also notice that the ferromagnetic  $T_c$  is only weakly affected by moderate antisite disorder and the low-field magnetoresistance is dramatically enhanced by disorder. Our real space approach allows an interpretation of these results in terms of the antisite domains and the intra and inter domain magnetic correlations and are consistent with the spatial imagery from recent experiments. The intra-grain effects highlighted here would be directly relevant to the single crystals. They also define the starting point for incorporating grain boundary effects in a theory of polycrystalline materials.

### 3.1 Introduction

Several double perovskite materials [1] of the form  $A_2BB'O_6$  exhibit high ferromagnetic  $T_c$  and significant low-field magnetoresistance. They are also a candidate source of spin-polarized electrons. The potential usefulness of these materials is, however, frustrated by inevitable mislocation of the B and B' ions, which do not organise themselves in the ideal alternating structure. This results in a

strong dependence of physical properties on the preparative conditions, reducing the magnetisation and destroying the half-metallicity. In this chapter we provide results on the impact of spatially correlated antisite disorder (ASD), as observed experimentally [2–4], on the ferromagnetic double perovskites. The antisite domains not only suppress magnetism and half-metallicity, as already known from studies of uncorrelated disorder, but also lead to an enhancement of the low-field magnetoresistance (MR). The properties depend not only on the gross degree of disorder (fraction of mislocated sites), but also on the degree of short range correlation.

## 3.2 Magnetic domain formation

In order to study the impact of correlated antisite disorder on the ferromagnetic phase, we have chosen four sets of disordered configurations, with increasing degree of mislocation, generated using a simple lattice-gas model [5], discussed in detail in the last chapter. On this correlated background, we have used a real space spin-fermion Monte Carlo method to solve the magnetic problem and study [6] the magnetic order, half-metallicity, transport, *etc.*

To get the ground state spin configuration, we anneal the electron-spin system down to very low temperature on a given structural motif, top row in Figure 3.1. Bottom row of Figure 3.1 shows the ground state magnetic snapshot. We have plotted the spin overlap factor  $g_i = \mathbf{S}_0 \cdot \mathbf{S}_i$ , where  $\mathbf{S}_0$  is a reference spin (left-lower-corner) in the lattice. For all disorder families, we find that structural and magnetic domains coincide with each other. This is consistent with the experimental observation by Asaka, *et al.* (Figure 1.7 ). Using transmission electron microscopy [7] of a single crystal of  $\text{Ba}_2\text{FeMoO}_6$  they have established that magnetic domain walls coincide with the crystallographic antiphase boundaries and the spins across the domain wall are antiferromagnetically aligned.

## 3.3 Temperature dependence of magnetisation

Let us examine the effect of the antisite disorder on the magnetic properties. Since rotation invariance, in the absence of an applied field, can lead to precession of the

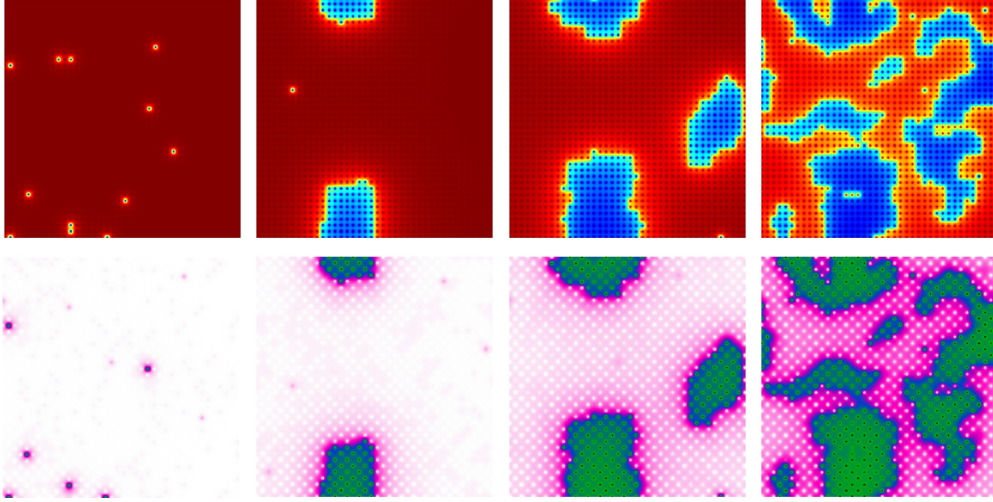


Figure 3.1: Structural and magnetic domains: Top row shows ASD configurations, one from each disorder family with  $S = 0.98, 0.76, 0.50, 0.08$ . Bottom row shows the corresponding ground state spin overlap factor  $g_i$ , in a Monte Carlo snapshot.  $g_i = \mathbf{S}_0 \cdot \mathbf{S}_i$ , where  $\mathbf{S}_0$  is the left lower corner spin in the lattice. Lattice size  $40 \times 40$ .

direction of the total magnetisation,  $\vec{M}$ , we prefer to calculate  $\langle M^2 \rangle$ , where  $\vec{M} = (1/N_s) \sum_i \mathbf{S}_i$ .  $\langle \rangle$  represents thermal average over equilibrium spin configurations and  $N_s$  is the number of B sites. This is related to the structure factor  $D(\mathbf{Q})$ : the Fourier transform of the correlation function of the spins at the B sites.

$$D(\mathbf{Q}) = \frac{1}{N_s^2} \sum_{i,j} \langle \mathbf{S}_i \cdot \mathbf{S}_j \rangle e^{i\mathbf{Q} \cdot (\mathbf{R}_i - \mathbf{R}_j)}$$

At  $\mathbf{Q} = (0, 0)$ ,  $D(\mathbf{Q})$  breaks up into two decoupled sums and is simply  $\langle M^2 \rangle$ .

Suppose the fraction of mislocated B, B' sites is  $x$ , and the structure is organised into domains such that the ratio of “perimeter” to “bulk” sites of the domains is small, *i.e.*, there is a high degree of short range correlation present in the system. The antiferromagnetic coupling between adjoining domains would polarise them antiparallel, and the net moment at  $T = 0, h = 0$  would be proportional to the volume difference of up and down domains. We should have  $M(T = 0, h = 0) \sim (1 - x) - x = 1 - 2x = S$ , so  $M^2 = S^2$ . Given our structural order parameter,  $S^2 = 0.96, 0.58, 0.25, 0.01$  in almost perfect correspondence with the  $T \rightarrow 0$  values in Figure 3.2 . The elaborate calculation arrives at an obvious answer.

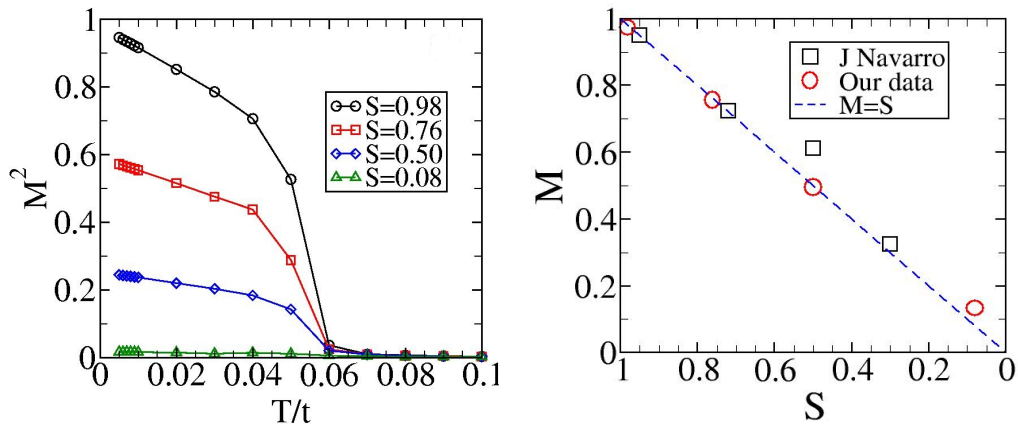


Figure 3.2: Left panel- The ferromagnetic peak in the structure factor,  $M^2$ , for different degrees of antisite disorder. Results are on a  $40 \times 40$  lattice, averaged thermally and over 10 copies of disorder. Right panel- Comparison of our saturation magnetisation (at  $T = 0$ ) with experimental measurement by Navarro *et al.* [8].

This behavior of  $M(T)$  can also be described by an *effective* Heisenberg model

$$H_{eff} = \sum_{\{ij\}} J_{ij} \mathbf{S}_i \cdot \mathbf{S}_j$$

where  $\{ \}$  represents the set of nearest neighbor and next nearest neighbor sites.  $J_{ij}$  is the effective coupling (FM/AFM) between the local moments at  $\mathbf{r}_i$  and  $\mathbf{r}_j$  sites. In our two dimensional ASD configurations  $J_F/t = -0.04$  operates between two local moments when they are at the next nearest neighbor position and  $J_{AF}/t = 0.065$  is active when the moments are at the nearest neighbor position (a B-O-B arrangement). The Heisenberg result for the ferromagnetic structure factor  $S(0,0)$  as a function of temperature matches very well, shown in Figure 6.2, with the electronic Hamiltonian result for all antisite disordered configurations. This is discussed in Chapter-6 in detail.

The *onset temperature* for magnetic order seems to be insensitive to the ASD, *i.e.*, the intra-domain order sets in at  $T \sim$  the bulk  $T_c$ . Note that for an  $O(3)$  model in 2D, the  $T_c$  vanishes in the infinite volume limit. We should ideally speak of a size dependent ‘correlation temperature’ but will not make this distinction.

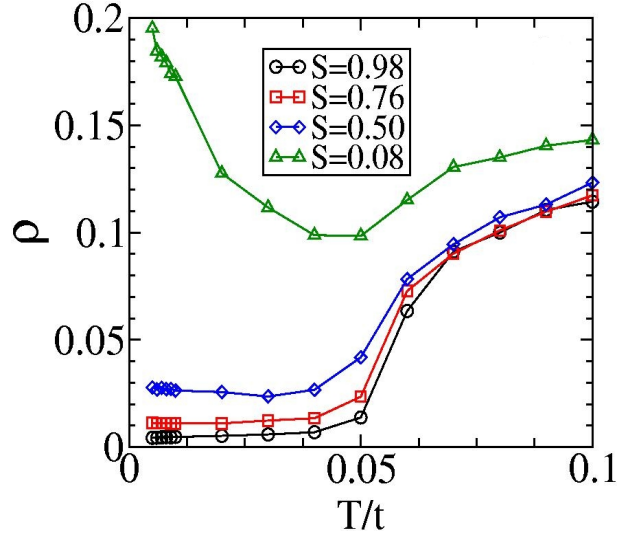


Figure 3.3: The *d.c.* resistivity,  $\rho(T)$ , for varying antisite disorder. Results are on a  $40 \times 40$  lattice, averaged thermally and over 10 copies of disorder.

Experimental measurement also shows a small variation in  $T_c$  with increasing antisite disorder upto  $S = 0.3$  [8]. While our answer for the suppression of magnetisation is  $M \sim (1 - 2x)$ , a 3D calculation, with uncorrelated disorder, had found [9]  $M \sim (1 - 1.9x)$ .

### 3.4 Temperature dependence of resistivity

We have studied the transport behavior on this correlated ASD background as shown in the Figure 3.3. The temperature dependence of resistivity  $\rho(T)$  remains similar from weak to intermediate disorder, with a sharp drop near  $T_c$ . The only effect of increasing disorder is an increase in the residual resistivity. It is as if there is a temperature independent *structural* scattering that gets added to the temperature dependent magnetic scattering. However, at large antisite disorder this correspondence breaks down: the low temperature resistivity is very large (and grows with growing system size) and  $d\rho/dT < 0$ . There seems to be a metal-insulator transition (between  $S = 0.50$  and  $S = 0.08$ ), in this two dimensional model, driven by antisite disorder.

To create an understanding of this let us focus on  $T = 0$ , where the magnetic

configuration is simple (collinear). The down spin electrons inhabit the up core spin domains and *vice versa*. The conductance arises from the inter-penetrating parallel channels for up and down spin electrons. One could call it *complementary percolation*. Let us identify up spin electrons with the *majority* phase and down spin with the *minority* phase. The net conductivity is  $\sigma_{tot}(S) = \sigma_{maj}(S) + \sigma_{min}(S)$ , which reduces monotonically with reducing S, as shown in Figure 3.3 . At fixed S one could increase  $\sigma_{tot}$  systematically by increasing  $p_{corr}$ , *i.e.*, reducing the fragmentation of the conduction paths. Thus, this insulating state at low temperature is different from the usual disorder induced insulating state like Anderson localization *etc.*, rather it arises due to the fragmentation of conduction path with increase in antisite disorder. Weak localisation effects, *etc.*, in two dimensions could show up at much longer lengthscales.

Since the antisite disorder configuration is temperature independent, the primary sources of temperature dependence in transport are:

1. weakening of the antiferro locking across the domain boundaries, and
2. fluctuations about the ferromagnetic state *within a domain*.

The first effect enhances the conductivity, while the second serves as a source of scattering. Their relative importance depends on zero temperature conductivity. For weak disorder (large S) the fragmentation is weak and the increase in resistivity due to intra-domain magnetic scattering is larger than the decrease from inter-domain tunneling. However, by the time  $S=0.50$ , there is already a weak upturn in  $\rho$  as  $T \rightarrow 0$ , the intra-domain effect is visible, and this becomes the dominant effect as  $S \rightarrow 0$ . An analysis of the spin-spin correlations illustrates the antiferro locking of domains at low temperature and how this weakens with increasing temperature.

The first column in Figure 3.4 reproduces one set of antisite disorder configurations from Figure 2.7 (first column). The next three columns show the the magnetic overlap  $g_i = \mathbf{S}_0 \cdot \mathbf{S}_i$ , where  $\mathbf{S}_0$  is the lower left corner spin in each configuration, for a Monte Carlo snapshot at  $T/t=0.03, 0.05, 0.07$ . These pictures would correspond to *magnetic domains*, if the patterns survive even after thermal averaging. The antiphase boundary (APB) and the magnetic domain wall (MDW) pattern coincide at  $T/t = 0.03$ . However at  $T/t=0.05$  (close to the

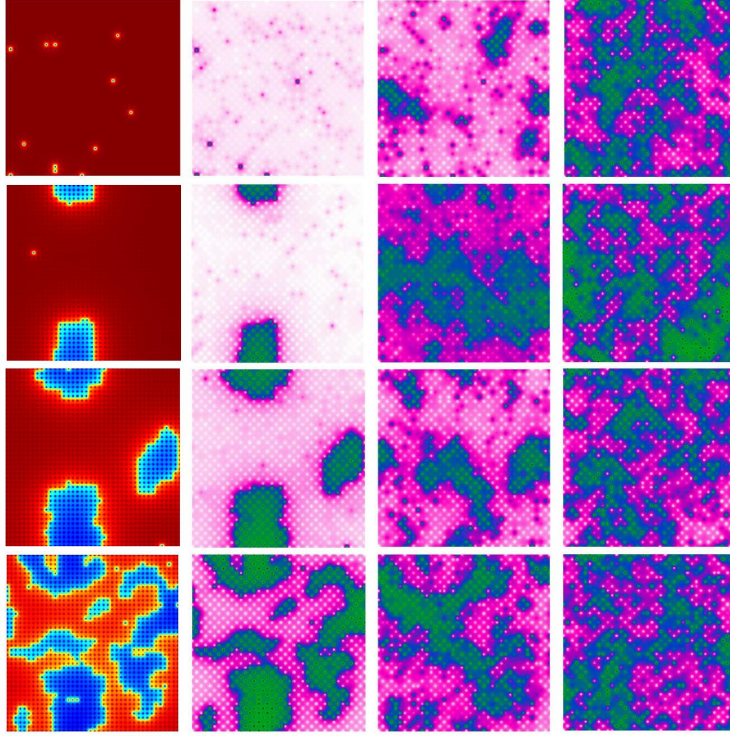


Figure 3.4: Temperature dependence of short range magnetic correlations. The left column shows ASD configurations, one from each disorder family.  $S=0.98, 0.76, 0.50$  and  $0.08$ , top to bottom. The 2nd, 3rd and 4th panel along each row is a map of a spin overlap factor,  $g_i$ , in a Monte Carlo snapshot.  $g_i = \mathbf{S}_0 \cdot \mathbf{S}_i$ , where  $\mathbf{S}_0$  is the left lower corner spin in the lattice. The temperatures are  $T/t = 0.03, 0.05, 0.07$ .

bulk  $T_c$ ), there is no correlation between the APB and the  $g_i$  pattern. There is *significant core spin overlap* across the boundary, and large fluctuation, overall, in spin orientation. This bears out the transport mechanism we suggested in the preceding section.

Our results above are relevant to the effect of ASD on single crystals. Single crystalline  $\text{Sr}_2\text{FeMoO}_6$  [10] shows a residual resistivity  $\rho \sim 0.1 \text{ m}\Omega\text{cm}$ , and metallic behavior  $d\rho/dT > 0$  but we have not been able to locate single crystal data for varying degree of ASD. Polycrystalline samples [11] (Figure 1.11 ) show a trend similar to ours but transport in these materials is also affected by the grain boundary resistance apart from antisite disorder. The residual resistivity in

these samples ranges from  $\sim 0.5$  m $\Omega$ cm for low antisite disorder ( $M/M_{max} \sim 1.0$ ) to  $\sim 10$  m $\Omega$ cm at high antisite disorder ( $M/M_{max} \sim 0.5$ ). Ordered polycrystals show  $d\rho/dT > 0$ , while less ordered ones show  $d\rho/dT < 0$  [11, 12].

### 3.5 Field dependence of resistivity

The field dependence of magnetisation and resistivity is shown in Figure 3.5 , at relatively low temperature ( $T/t=0.03$ ) in (a)-(b) and at high temperature ( $T/t=0.07$ ) in (c)-(d). Three energies play out when  $h \neq 0$  :

1. the bulk Zeeman cost of the *minority* domains  $\sim hV_{min}$ , where  $V_{min}$  is the volume of the minority phase,
2. the interfacial antiferromagnetic energy  $\sim J_{AF}V(1-p_{corr})$ , where  $(1-p_{corr})$  is the fraction of antiferro bonds on the lattice,
3. the *gain in electronic kinetic energy* on removal (or rotation) of MDW's.

Here, the first and third prefer domain alignment while the second prefers to retain domain walls. In a ‘spin only’ model the third would be absent. This delocalisation energy gain serves to reduce the field at which domain rotation can occur. At low temperature, Figure 3.5 (a)-(b), the ordered samples have a high degree of magnetic order, so the field induced increase in  $M$  and the decrease  $\Delta\rho/\rho(0)$ , is quite small, where  $\rho(0)=\rho(h)|_{h=0}$  and  $\Delta\rho = \rho(0) - \rho(h)$ . However, the low temperature low field response is dramatic for low  $S$  samples. These samples have  $M(h=0) \sim 0$  and a large  $\rho(0)$  due to the fragmented (spin selective) conduction path. A field as small as  $h/t \sim 0.001$  leads to  $M^2 \sim 0.1$ , so  $M \sim 0.3$ . The corresponding impact on spin correlations is shown in the lowest row in Figure 3.6 , where the MDW pattern is strongly affected by  $h$ . While the domain rotation effect is visible for both  $S = 0.50$  and  $S = 0.08$ , the less disordered sample had a larger conductivity at  $h = 0$ , so the fractional change is much larger for  $S = 0.08$ . At high temperature, Figure 3.5 (c)-(d), the domains cease to exist and conductance gain from domain rotation is irrelevant. In the large  $S$  samples there are few antiferro links so the applied field just suppresses the magnetic fluctuations leading to large  $\Delta\rho/\rho(0)$ . In the most disordered samples

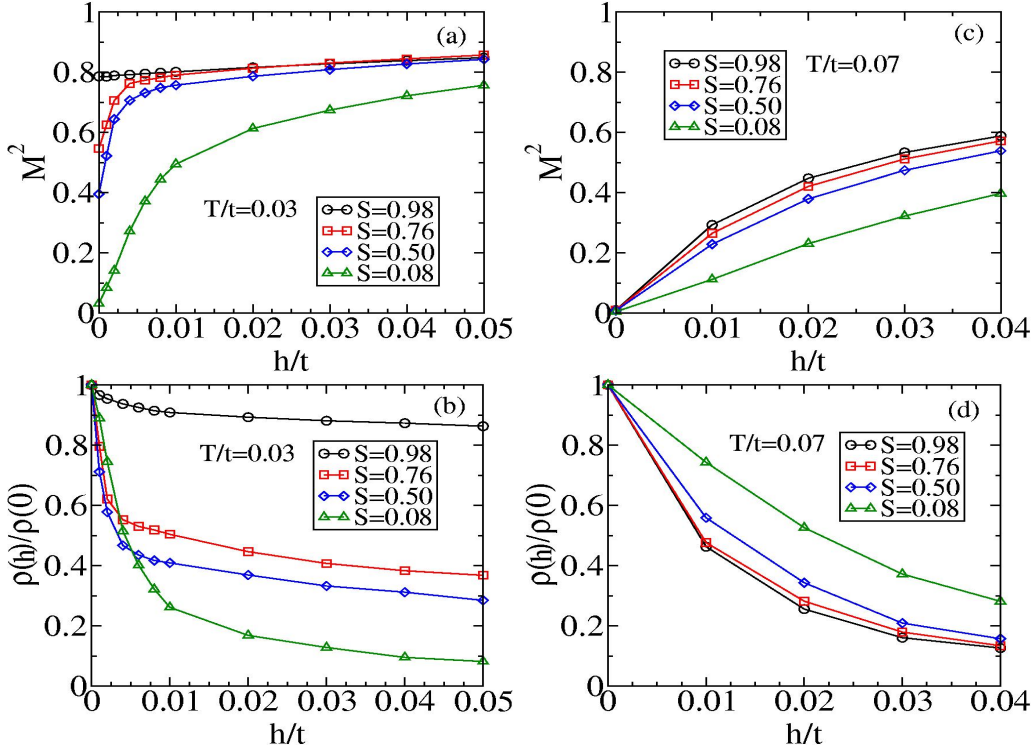


Figure 3.5: (a),(c) Field dependence of magnetisation,  $M^2$ ; (b),(d) field dependence of the resistivity, normalised to  $h = 0$ . Left panel is at low temperature ( $T/t=0.03$ ), and right is at high temperature ( $T/t=0.07$ ).

there are  $(1 - p_{corr})/2 \sim 7\%$  of antiferro bonds. Although there are no domains, these act as a source of scattering. The gain in conductivity is slower in the disordered samples compared to the more ordered ones.

This dramatic enhancement of the low-field magnetoresistance for low  $S$  samples is different from the large magnetoresistance observed in polycrystalline samples, where the magnetoresistance is derived from the magnetic polarization of grain-boundary regions acting like spin valves, and dominant mechanism is inter-grain tunneling across physical grain boundaries [13].

In a single crystal measurement Tomioka *et al.* [10] (Figure 1.11) have measured the temperature profiles of resistivity in several magnetic fields for a antite disordered  $\text{Sr}_2\text{FeMoO}_6$  crystal with  $S = 0.84$ . The MR is weak ( $< 10\%$ ) at low temperature at a field of 5T. Unfortunately, the MR of single crystals with systematic variation of ASD is not available. For polycrystalline samples

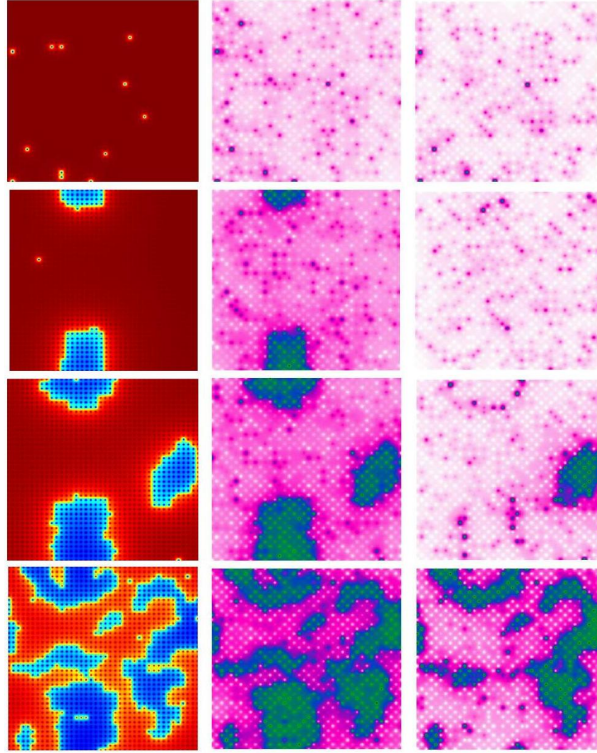


Figure 3.6: Field dependence of magnetic spatial correlations. We show the usual  $g_i = \mathbf{S}_0 \cdot \mathbf{S}_i$ , defined earlier. The left column shows the ASD domains, the central column shows  $g_i$  at  $h/t = 0$ , and the right column is for  $h/t=0.001$ . The temperature is  $T/t=0.03$ .

the grain boundary effect is also present, as we have seen above. The MR can be large,  $\sim 40\%$  (Figure 1.12), at low temperature and at a field of 5T [12], and seems to be dominated by grain boundary effects [13,14]. Some results indicate a decrease [12] in MR with increasing antisite disorder, while others show an increment [15]. Similar to the temperature dependence of resistivity, the effects of antisite disorder and grain boundaries on MR have not been deconvolved yet.

### 3.6 Half-metallicity

Ordered  $\text{Sr}_2\text{FeMoO}_6$  has ferrimagnetic spin arrangement with large positive Hund's coupling on the magnetic (Fe) sites. Thus, only those electrons which are oppositely oriented to the core magnetic ions are able to conduct. Since it allows

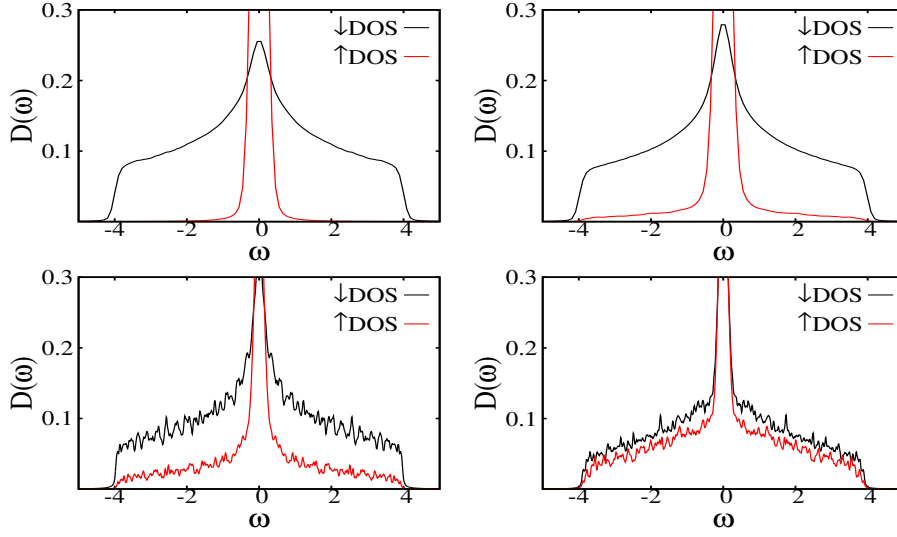


Figure 3.7: Spin resolved density of states at low temperature with increasing antisite disorder. For the top row :  $S = 1.0$  and  $0.76$ ; for the bottom row :  $S = 0.50$  and  $0.08$ , as we move from left to right.

only one spin channel to conduct, it is half-metallic. Antisite disorder destroys the half-metallicity. We have studied the impact of antisite disorder on the spin resolved density of states and its thermal evolution.

### 3.6.1 Impact of disorder at low temperature

Figure 3.7 shows the spin resolved density of states at low temperature with increasing antisite disorder. Left column of the top row is for the ordered double perovskite. Here up-spin electrons are localized and only down-spin electrons conduct. Hence, at low temperature it shows half-metallic behavior. But this potentially useful property gets destroyed by the antisite disorder. As we can see in the right column of the top row that antisite disorder  $\sim 12\%$  has already created density of states for the minority electrons.

### 3.6.2 Temperature dependence

Figure 3.8 shows the thermal evolution of spin resolved density of states at weak and moderate antisite disorder ( $S = 0.98$  and  $0.50$ ) at temperatures ranging be-

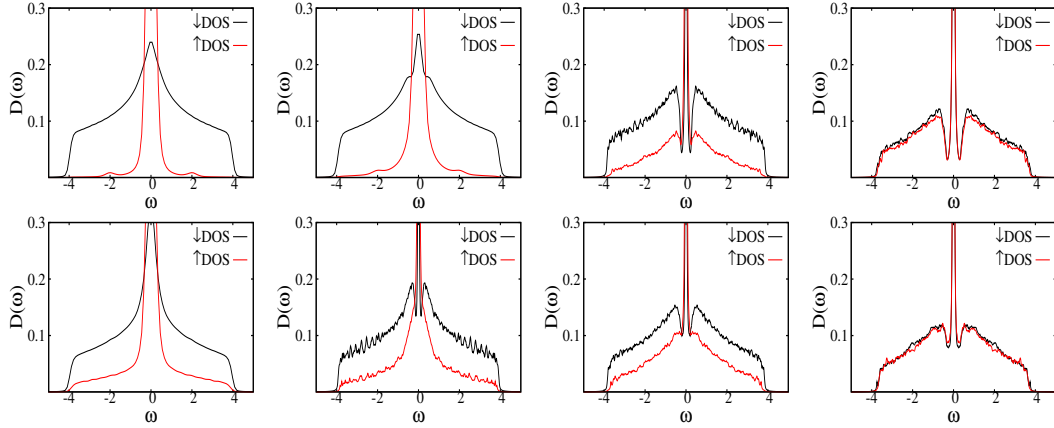


Figure 3.8: Top: thermal evolution of spin resolved density of states at weak antisite disorder  $S = 0.98$ . Bottom: same at strong disorder  $S = 0.50$ . Temperatures  $T/t = 0.01, 0.03, 0.05, 0.07$  from left to right.

tween 0.01 and 0.07. Upon increasing the temperature, the up-spin density of states gets broader due to the thermal fluctuation of spins around the ferromagnetic state. At high temperature ( $T/t = 0.07$ ) up and down-spin density of states become similar. Here we observe a dip in the density of states around  $\omega = 0$  due to the band narrowing (hopping suppression) effect of spin disorder. This dip is weaker in the moderately disordered case due to the competing band broadening effect of structural disorder.

### 3.6.3 Polarisation and itinerant moment

These systems are unusual because at  $T = 0$  within each domain the conduction electron has only one spin polarisation, but averaged over the system both up and down electrons have density of states present at  $\epsilon_F$ . A local probe, with probe area  $\ll \xi^2$ , where  $\xi$  is the typical domain size, will allow only spin polarised tunneling, while a probe averaging over domains will see both  $D_{\uparrow}(\epsilon_F)$  and  $D_{\downarrow}(\epsilon_F)$ . Figure 3.9 shows polarisation  $P = \frac{D_{\uparrow}(\epsilon_F) - D_{\downarrow}(\epsilon_F)}{D_{\uparrow}(\epsilon_F) + D_{\downarrow}(\epsilon_F)}$  and itinerant moment  $\mu = \frac{n_{\uparrow} - n_{\downarrow}}{n_{\uparrow} + n_{\downarrow}}$ , as a measure of half-metallicity. These are unity only in the absence of ASD at  $T = 0$ , and in general have a behavior that broadly mimics the behavior of the core spin magnetisation, (Figure 3.2), in its disorder and temperature dependence.

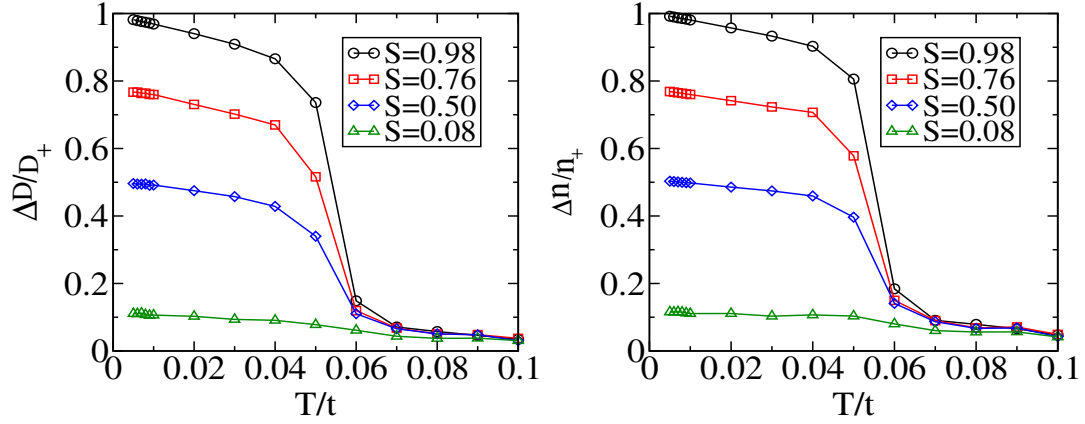


Figure 3.9: Half-metallicity, estimated as  $\frac{D_{\uparrow}(\epsilon_F) - D_{\downarrow}(\epsilon_F)}{D_{\uparrow}(\epsilon_F) + D_{\downarrow}(\epsilon_F)}$  and  $\frac{(n_{\uparrow} - n_{\downarrow})}{(n_{\uparrow} + n_{\downarrow})}$ , for varying temperature and different degrees of antisite disorder.

## 3.7 Discussion

Unlike the simple perovskite oxides, the double perovskite oxides possess inevitable B-site antisite disorder, due to similar sizes of B-site cations. The disorder has a high degree of short-ranged correlation. In order to completely characterise the sample one has to specify the gross degree of disorder (*i.e.*, fraction of mislocated sites  $x$ ) and the degree of short-ranged correlation  $p$  in it. The magnetisation, and the half-metallicity are not strongly affected by this correlated disorder. The domain structure of antisites makes the most difference in the transport: there is a rise in the resistivity at low temperature due to transmission blocking at antiferro domain boundaries, and large low field magnetoresistance due to domain rotation. There are three issues we want to touch upon, to relate our work to the real double perovskites.

### 3.7.1 Role of dimensionality

We have concentrated on two dimensions since we wanted to study large system sizes. This helps in capturing the impact of antisite disorder correctly and also aids visualisation. It is well known that localisation effects are stronger in 2D compared to 3D, so we performed the entire calculation on a  $16^3$  system to check out the trends in transport. We solved the same model as discussed earlier in 3D

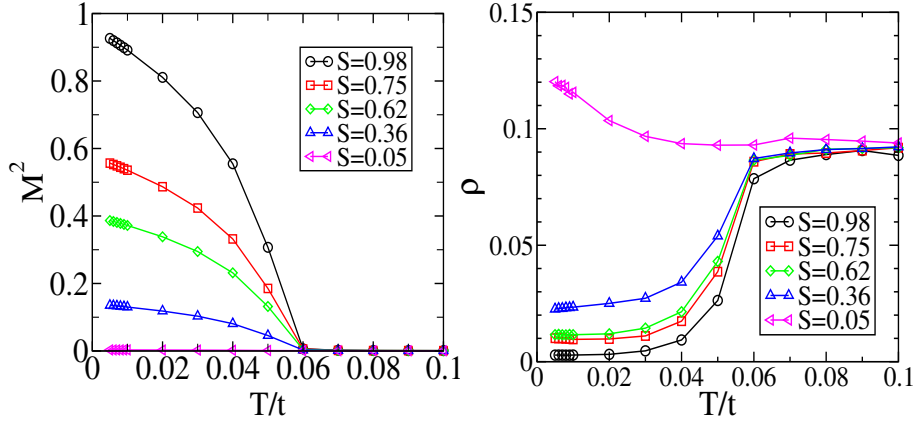


Figure 3.10: Left panel - The ferromagnetic peak in the structure factor  $M^2$ , where  $M$  is the magnetisation, for different degrees of antsite disorder. Right panel - The *dc* resistivity,  $\rho(T)$  for varying antsite disorder. Results are on a  $16^3$  lattice, averaged thermally and over 10 copies of disorder.

antsite disordered backgrounds on lattice sizes upto  $16^3$  [16]. In that case both the kinetic energy and magnetic ordering have a 3D character. The results on magnetisation and resistivity are shown in Figure 3.10. The trends in both  $M^2$  and  $\rho(T)$  are similar to what we have obtained in 2D case as shown in the Figure 3.2 and 3.3 respectively. There is a sharp increase in the  $T = 0$  resistivity (although possibly no insulating phase) with increasing antsite disorder. The low-temperature upturn in  $\rho(T)$  is also present, but weaker, in 3D. The trends in magnetoresistance are also similar between 2D and 3D.

### 3.7.2 Hubbard interactions

The primary mechanism behind magnetism in the double perovskites is a variant of *double exchange*, driven by the large Hund's coupling on the B site. This is adequate in a one band context. When band degeneracy is considered, as is true of the real material, the inter-orbital Hubbard effect on the B (magnetic) site, and weaker correlation effects on the B' (nonmagnetic) site would be needed for a quantitative theory of the itinerant moment. However, comparison of our data [16] with existing results [17] shows that the qualitative trends in disorder

dependence remain the same. Although we are mainly interested in the disorder dependence, the correlations effects also need to be included to understand results like photoemission in  $\text{Sr}_2\text{FeMoO}_6$  [18].

### 3.7.3 Effect of grain boundaries

In the absence of a chemical characterisation of the grain boundary material, and an electronic model for the grain boundary, it is hard to construct a comprehensive theory. However, since grain size,  $l_G \gg \xi$  (where  $\xi$  is the structural correlation length), it should be possible to study the role of antiphase boundaries and magnetic domain walls via probes that focus on a single grain.

The *intra-grain* effects highlighted here would be directly relevant to single crystals, and define the starting point for a transport theory of the polycrystalline double perovskites.

## 3.8 Conclusion

We have studied a double perovskite model on antisite disordered backgrounds with a high degree of short-range correlation. In this situation, the antiphase boundaries coincide with the  $T=0$  magnetic domain walls. Growing ASD reduces the low-field magnetisation, destroys the half-metallicity, and leads to a low-temperature metal-insulator transition. While these are disadvantages, we also note that the ferromagnetic  $T_c$  is only weakly affected by moderate ASD and the low-field magnetoresistance is dramatically enhanced by disorder. Our real space results allow an interpretation of these in terms of the domain pattern, the effective exchange, and the short-range magnetic correlations. They are also consistent with explicit spatial imagery from recent experiments. The “intra-grain” effects highlighted here would be directly relevant to single crystals, and define the starting point for a transport theory of the polycrystalline double perovskites.

# Bibliography

- [1] For reviews, see D. D. Sarma, *Current Op. Solid State Mat. Sci.* **5**, 261 (2001); D. Serrate, J. M. de Teresa, and M. R. Ibarra, *J. Phys. Cond. Matt.* **19**, 023201 (2007).
- [2] T. Asaka, X. Z. Yu, Y. Tomioka, Y. Kaneko, T. Nagai, K. Kimoto, K. Ishizuka, Y. Tokura, and Y. Matsui, *Phys. Rev. B* **75**, 184440 (2007).
- [3] J. Navarro, L. Balcells, F. Sandiumenge, M. Bibes, A. Roig, B. Martnez, and J. Fontcuberta, *J. Phys. Cond. Matt.* **13**, 8481 (2001).
- [4] C. Meneghini, S. Ray, F. Liscio, F. Bardelli, S. Mobilio, and D. D. Sarma, *Phys. Rev. Lett.* **103**, 046403 (2009).
- [5] P. Sanyal, S. Tarat, and P. Majumdar, *Eur. Phys. J. B* **65**, 39 (2008).
- [6] V. N. Singh and P. Majumdar, *Europhys. Lett.* **94**, 47004 (2011).
- [7] T. Asaka, X. Z. Yu, Y. Tomioka, Y. Kaneko, T. Nagai, K. Kimoto, K. Ishizuka, Y. Tokura and Y. Matsui, *Phys. Rev. B*, **75**, 184440 (2007).
- [8] J. Navarro, J. Nogués, J. S. Muñoz, and J. Fontcuberta, *Phys. Rev. B* **67**, 174416 (2003).
- [9] J. L. Alonso, L. A. Fernandez, F. Guinea, F. Lesmes, and V. Martin-Mayor, *Phys. Rev. B* **67**, 214423 (2003).
- [10] Y. Tomioka, T. Okuda, Y. Okimoto, R. Kumai, K.-I. Kobayashi, and Y. Tokura, *Phys. Rev. B* **61**, 422 (2000).
- [11] Y. H. Huang, M. Karppinen, H. Yamauchi, and J. B. Goodenough, *Phys. Rev. B* **73**, 104408 (2006).

- [12] Y. H. Huang, H. Yamauchi, and M. Karppinen, *Phys. Rev. B* **74**, 174418 (2006).
- [13] D. D. Sarma, S. Ray, K. Tanaka, M. Kobayashi, A. Fujimori, P. Sanyal, H. R. Krishnamurthy, and C. Dasgupta, *Phys. Rev. Lett.* **98**, 157205 (2007).
- [14] D. Niebieskikwiat, F. Prado, A. Caneiro, and R. D. Sanchez, *Phys. Rev. B* **70**, 132412 (2004).
- [15] J. Navarro, L. Balcells, F. Sandiumenge, M. Bibes, A. Roig, B. Martnez, and J. Fontcuberta, *J. Phys. Cond. Matt.* **13**, 8481 (2001).
- [16] V. N. Singh and P. Majumdar, unpublished.
- [17] B. Aguilar, O. Navarro and M. Avignon, *EPL*, **88**, 67003 (2009).
- [18] M. Kobayashi, K. Tanaka, A. Fujimori, S. Ray, and D. D. Sarma, *Phys. Rev. Lett.* **98**, 246401 (2007).



# Chapter 4

## Impact of Antisites on Antiferromagnetic Order

**Chapter summary:** This chapter focuses on the metallic antiferromagnetic phase, and the phase coexistence window. For spatially correlated antisite disorder antiferromagnetic order is affected *much less strongly* than ferromagnetism. This intriguing result arises from the finite  $\mathbf{Q}$  nature of antiferromagnetic order which leads to a weaker cancellation of the order between domains. For a given structural order parameter  $S$  (which measures the fraction of correctly located sites) the A type antiferromagnetic structure factor follows  $D_A \sim (1 + S^2)/2$ , in contrast to  $D_F \sim S^2$  in the ferromagnet, while the G type phase follows  $D_G \sim (1 + S)^2/4$ . So, despite the possibility of large antisite disorder there is certainly hope of observing antiferromagnetic phases. The antiferromagnetic states are metallic, and the electronic wavefunctions in these phases continue to be spatially extended even at large disorder. Antisite disorder increases the residual resistivity but we did not observe any insulating regime.

### 4.1 Introduction

The “simple perovskite” transition metal oxides - the cuprates, manganites, or cobaltates, have a rich phase diagram [1], with a strong dependence on the doping level. The manganites, for instance, exhibit not just ferromagnetism (FM), but also CE-type magnetic order and A, C, and G type antiferromagnetic (AFM) phases [2], depending on the hole doping level.

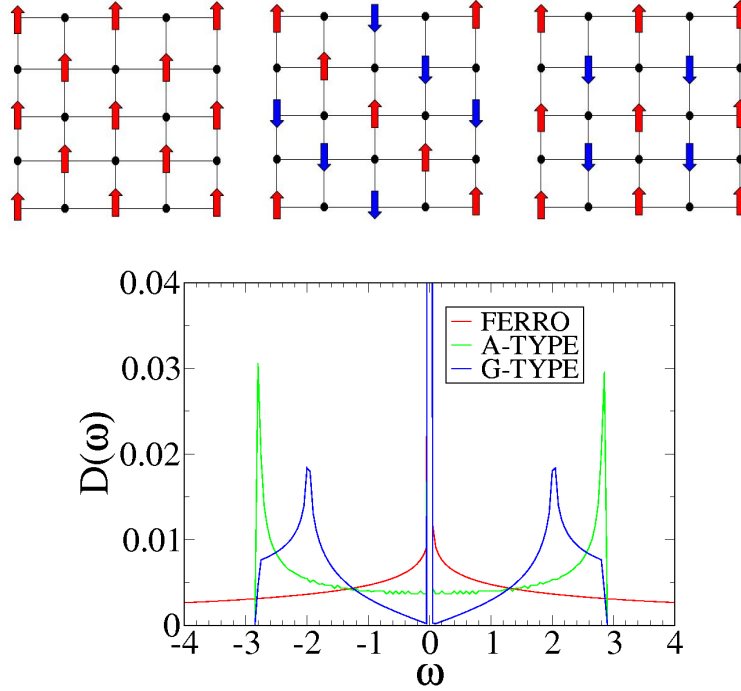


Figure 4.1: Top panel : Three magnetic phases in the structurally ordered 2D double perovskite model. Left- ferromagnet, center- A type antiferromagnet, right- G type antiferromagnet. Bottom panel : Electronic density of states for the ferromagnetic, A and G type ordered phases in the structurally ordered background.

Similarly one may also expect the double perovskites to exhibit non ferromagnetic order upon significant electron doping. This has been seen in model Hamiltonian studies [3–6] and confirmed via *ab initio* calculations [7,8]. The antiferromagnetic phases should occur, for example, on sufficient electron doping of materials like  $\text{Sr}_2\text{FeMoO}_6$  (SFMO) via La substitution for Sr. Clear experimental indication of such antiferromagnetic order is limited [9,10], possibly because of increase in antisite disorder with La doping on  $\text{Sr}_2\text{FeMoO}_6$ , although intriguing signatures of non-ferromagnetic behavior are seen.

The phase diagram mapping out the occurrence of antiferromagnetic phases in the *clean* limit in two dimensions has been established earlier [3]. The top panel of Figure 4.1 shows the three magnetic phases in a structurally ordered

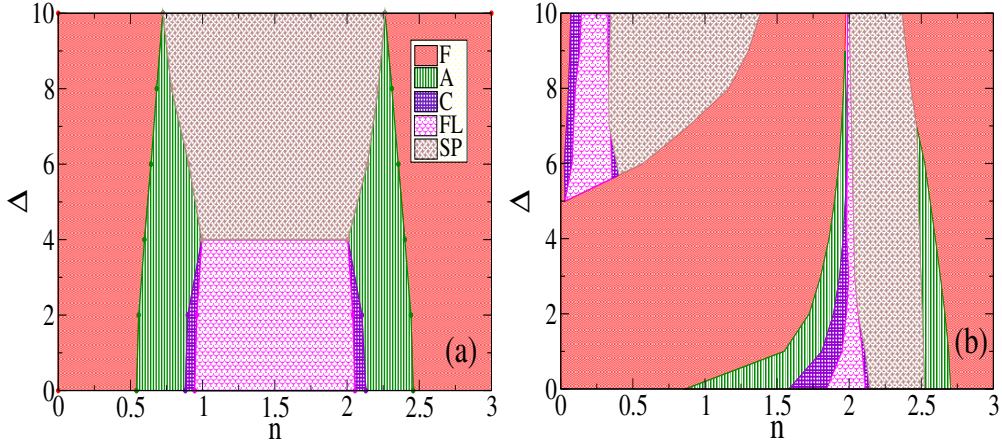


Figure 4.2: Magnetic ground state for varying electron density,  $n$ , and effective B-B' level separation,  $\Delta$ . (a): Phase diagram with only BB', *i.e.*, nearest neighbor, hopping. (b): Phase diagram when an additional B'-B' hopping,  $t'/t = -0.3$ , is included. The labels are: F (ferromagnet), A (planar phase), C (line like), FL (flux) and SP (spiral). This figure does not show the narrow windows of phase separation in the model. The phase diagrams are generated via a combination of Monte Carlo and variational calculations on lattices of size upto  $20 \times 20 \times 20$  [4].

background in a two dimensional double perovskite model. These occur with increasing electron density. The moments are on the B sites. We have not shown the induced moments on the B' sites.

At low electron density a ferromagnetic alignment of the core spins is favored since it leads to the maximum bandwidth. However, at sufficiently large band filling, antiferromagnetic states with A or G type order successively become favored, as shown in the bottom panel of Figure 4.1. While these spin configurations lead to smaller electronic bandwidth they have a higher density of band edge states compared to the ferromagnet.

In contrast to the two dimensional case, where the effective magnetic lattice is bipartite, the three dimensional lattice has a geometrically frustrated face centered cubic structure. This promotes various non-collinear spiral states and “flux” like phases in addition to collinear antiferromagnetic ordered phases, studied in

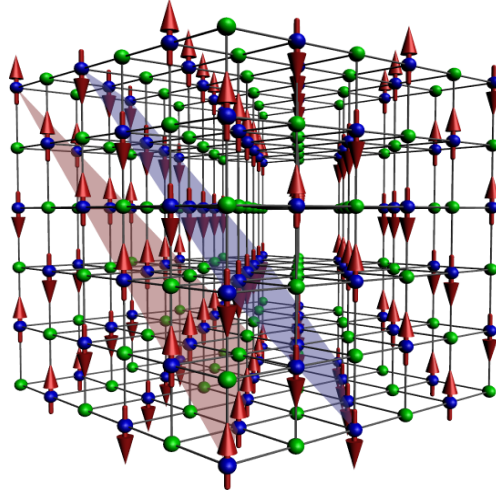


Figure 4.3: Spin configuration for A type order. The spins are parallel within the 111 planes (shown) and are antiparallel between neighboring planes. The delocalisation is effectively two dimensional [4].

detail elsewhere [4]. Figure 4.2 shows, at large Hund's coupling, the possible magnetic phases for varying electron density, level separation  $\epsilon_B - \epsilon_{B'}$ , and the crucial B'-B' (next neighbor) hopping  $t'$ . In addition to FM, and collinear A and C type order, the phase diagram includes large regions of non-collinear flux and spiral phases and windows of phase separation. Modest B'-B' hopping leads to significant shift in the phase boundaries, and particle-hole asymmetry.

Figure 4.3 shows the spin configuration for A type order in three dimension. The spins are parallel within the 111 planes (shown) and are antiparallel between neighboring planes. The conduction path gets divided into two sub-lattices, such that each spin channel gets to delocalise in one sub-lattice. In one such sub-lattice, only one of the up or down spin electrons can delocalise, the other remains localised. The roles of up and down are reversed in going from one sub-lattice to other, as a result one gets spin-degenerate localised and dispersive bands for antiferromagnetic phases. The delocalisation is effectively two dimensional. This A type order in three dimension is analogous to the A type antiferromagnet phase in two dimension (top panel of Figure 4.1 ), with the ferromagnetic planes being equivalent to the ferromagnetic stripes.

In order to get to these phases we have to electron dope the system. In real material this leads to an increase in the amount of antisite disorder. To understand this situation we have studied [11] the survival of electronically driven antiferromagnetism in the presence of spatially correlated antisite disorder in a two dimensional model. We have worked in two dimensions for ease of visualisation and to access large system size, and will comment on the three dimensional situation at the end. We have focussed on a couple of electron densities, one each in the A type and G type window, respectively.

## 4.2 Earlier studies on AFM order

Early studies using model Hamiltonians for double perovskites had observed the instability [5] of the ferromagnetic state, without exploring the competing phase that emerges. A subsequent variational study [6] did identify non-ferromagnetic phases. More recent studies using both simple models [3] and realistic DFT calculations [7,8] indicate that the ferromagnet becomes unstable to an A type phase on increasing electron density. In  $\text{Sr}_{2-x}\text{La}_x\text{FeMoO}_6$ , for example, this is expected to happen for  $x \gtrsim 1$ . The DFT studies have employed supercells for a few commensurate doping levels. Using a three band model Hamiltonian with parameters inferred from the DFT, the same authors have explored [7] a more continuous variation of La doping level and confirmed the DFT trends. The crossover to a non-ferromagnetic ordered state is, therefore, not an artifact of a single band model or two dimensionality that earlier studies employed.

Regarding the effect of antisite disorder on the non-ferromagnetic phases, we are aware of only one study involving uncorrelated antisite defects [6]. It is more focused on the doping dependence, and explores mainly the magnetism, but the trends are consistent with what we observe here.

Samples have indeed been synthesised with large La doping on  $\text{Sr}_2\text{FeMoO}_6$  [9,10]. The main observations are (i) a suppression [9] of the low field magnetisation with increasing  $x$  (may be related to increase in antisite defects), and (ii) signature of an antiferromagnetic metallic ground state in heavily electron doped  $\text{Sr}_2\text{FeMoO}_6$  [10]. There is unfortunately no detailed understanding of the impact of antisite disorder in these samples yet, or any data on resistivity and

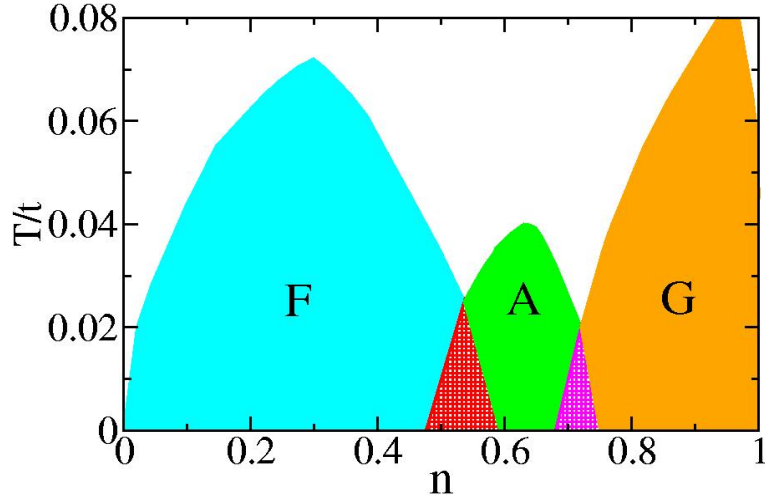


Figure 4.4: Phase diagram for the non disordered double perovskite. We only show the region  $n = [0, 1]$ . From  $n = 1$  to  $n = 2$  one populates the non-dispersive B' level, and the magnetic state is G type. The  $n = [2, 3]$  window is a symmetric version of the  $n = [1, 2]$  region. The regions between the phases indicate phase separation. The results are obtained via Monte Carlo on a  $40 \times 40$  lattice [3].

magnetoresistance.

Let us describe the phase diagram of the two dimensional model in the clean limit before considering disorder. In the absence of antisite disorder, there are no AFM superexchange interactions in the system, and the magnetic order is decided by minimisation of the electronic energy. For Hund's coupling much much greater than hopping amplitude the model supports three collinear phases. The FM state gives way to A type (line like) order with increasing electron density, and finally to a G type state. These have been discussed earlier [3]; we reproduce the magnetic configurations in the top panel, and the electronic density of states in the bottom panel of Figure 4.1 . The ferromagnetic state is preferred at low density,  $n$ , since it has the largest bandwidth. The A type state has lower bandwidth, but with large density of states near the band edge. The FM becomes unstable at  $n \sim 0.45$ . The A type state is stable for  $n \geq 0.58$ , and between these we have a phase separation window. Similarly the A to G transition involves a phase

separation window. The phase separation windows narrow with increasing  $T$  and vanish as  $T \rightarrow T_c$ . The thermal transitions and the phase separation windows are shown in Figure 4.4.

Broadly, the task would be to extend this phase diagram to finite antisite disorder. Instead of attempting to map out the disorder dependence at *all densities* we choose two representative densities,  $n \sim 0.65$  in the A type window, and  $n \sim 0.95$  in the G type region, to clarify the impact of disorder. We also explore the effect of antisite disorder on the phase separation window, between the ferromagnet and the A type phase, since it would be encountered in any attempt to electron dope the ferromagnet.

### 4.3 Disorder configurations

We study four families, with progressively increasing antisite disorder as discussed earlier (Figure 2.7). A representative configuration from each family is shown in the top row in Figure 4.5. They have *structural order parameter*  $S = 0.98, 0.76, 0.50, 0.08$  as we move from left to right. The red and blue colours indicate internally ordered domains but with a phase slippage between them. We plot  $(\eta_i - 1/2)e^{i\pi(x_i+y_i)}$ .

The middle row shows the A type antiferromagnetic phase on this structural motif, while the bottom row shows the G type phase. The magnetic correlations are characterised via the overlap factor  $g_i = \mathbf{S}_0 \cdot \mathbf{S}_i$ , where  $\mathbf{S}_0$  is the left lower corner spin in the lattice. As mentioned earlier, our disorder average for magnetic and electronic properties is performed typically over 10 configurations within each family.

### 4.4 AFM order with antisite disorder

In the ferromagnetic case it is simple to see that the presence of antiferromagnetic superexchange at the antiphase boundary would tend to align spins in opposite directions across an antiphase boundary. The system breaks up into up and down spin domains. Suppose the *up spin* domains correspond to the correctly located sites and are the *majority*. The net magnetisation is proportional to the volume

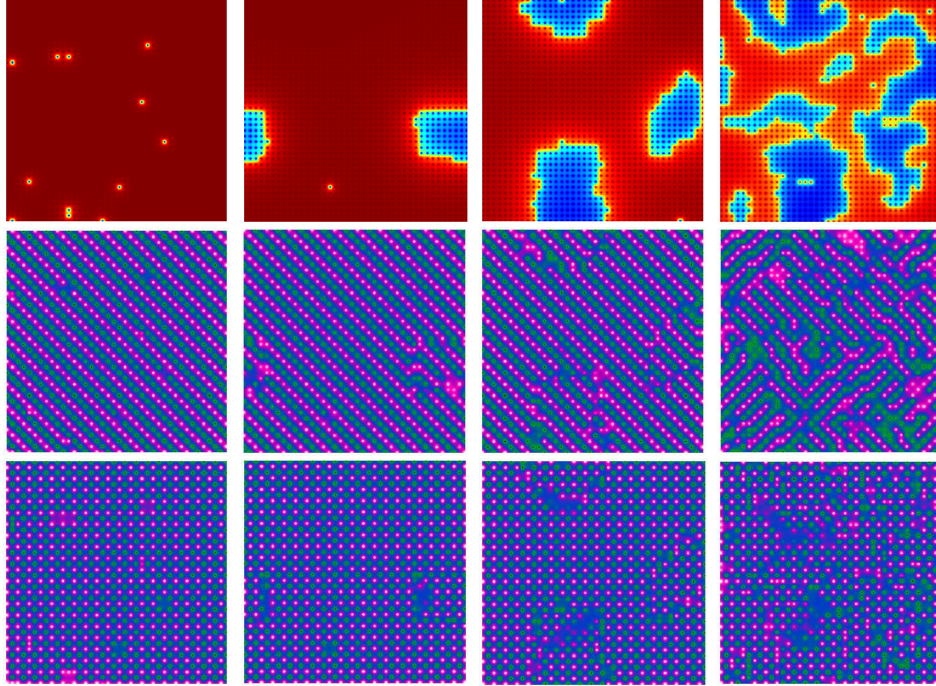


Figure 4.5: Antiphase domains and corresponding antiferromagnetic phases. The top row shows the domain pattern in the ASD background, with increasing disorder. The middle row shows the A type antiferromagnetic phase on this structural motif, while the bottom row shows the G type phase.

difference between the correctly located and *mislocated* regions. If the degree of mislocation is  $x$ , then the normalised magnetisation  $M = (1-x) - x = 1 - 2x = S$ . In the magnetic structure factor  $D(\mathbf{q})$ , the ferromagnetic peak is at a pair of wave-vectors,  $\mathbf{Q}_{F1} = \{0, 0\}$  and  $\mathbf{Q}_{F2} = \{\pi, \pi\}$ . We have set the lattice spacing  $a_0 = 1$  on the DP lattice. A pair of wave-vectors is required to characterise an ordered state since half the sites (the B') are non magnetic and hence *zeroes* of the spin field. Since  $D(\mathbf{Q}_{F1})$  is simply  $M^2$ , the domain argument, above, yields  $D(\mathbf{Q}_{F1}) \sim S^2$ . This dependence is well established experimentally [12], and also observed by us [13].

For the A type phase, studied on the same antisite structures as the ferromagnet, the nature of local magnetic order is more subtle. For the clean

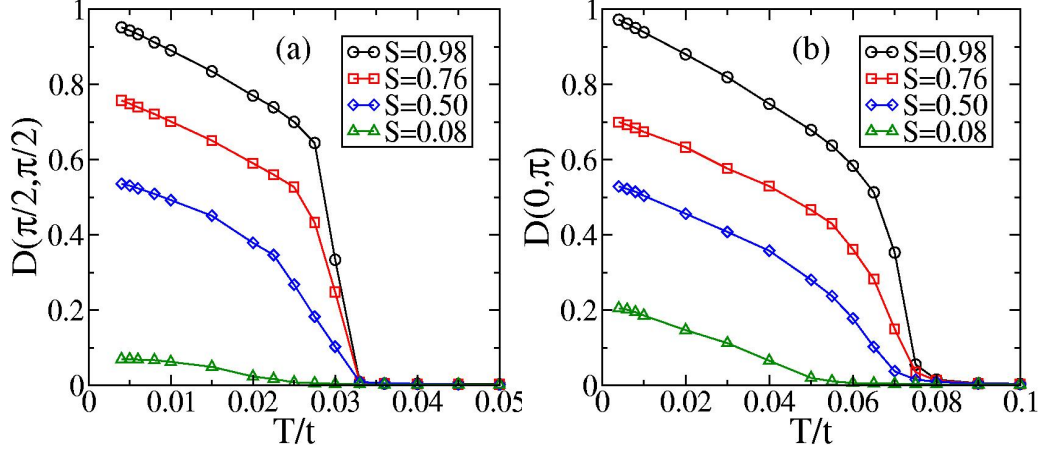


Figure 4.6: Magnetic order in the A type and G type phases with ASD. The results are based on Monte Carlo on  $40 \times 40$  systems, and averaged typically over 10 configurations for each value of  $S$ .

A type antiferromagnetism the order is at *two possible pairs* of wavevectors,  $\mathbf{Q}_{A1} = \{\pi/2, \pi/2\}$  and  $\mathbf{Q}_{A2} = \{3\pi/2, 3\pi/2\}$ , or  $\mathbf{Q}_{A3} = \{\pi/2, 3\pi/2\}$  and  $\mathbf{Q}_{A4} = \{3\pi/2, \pi/2\}$ . The two sets arise due to the two possible diagonals along which the ferromagnetic stripes can order. Within each set there are two  $\mathbf{Q}$  values because half the sites in the double perovskite lattice are non-magnetic, and the spin field has to have nodes there. In the clean system either  $\{\mathbf{Q}_{A1}, \mathbf{Q}_{A2}\}$  or  $\{\mathbf{Q}_{A3}, \mathbf{Q}_{A4}\}$  are picked. In a disordered system all four can show up, as in the middle row, last column, in Fig.3. For the G type phase the order is at the single pair:  $\mathbf{Q}_{G1} = \{\pi, 0\}$  and  $\mathbf{Q}_{G2} = \{0, \pi\}$ , there is no degeneracy.

The middle and bottom rows in Figure 4.5 show A type and G type order, respectively, for progressively increasing antisite disorder. Figure 4.6 quantifies the suppression of the ordering peak in  $D(\mathbf{q})$ , after disorder averaging over copies with roughly fixed degree of mislocation.

We will analyse the structure factor,  $D(\mathbf{q})$ , in terms of the domain pattern.  $D(\mathbf{q})$  is related to the Fourier transform of the spin configuration:

$$D(\mathbf{q}) = \frac{1}{V^2} |\vec{f}(\mathbf{q})|^2$$

$$\vec{f}(\mathbf{q}) = \sum_{\mathbf{r}_i} \mathbf{S}_i e^{i\mathbf{q} \cdot \mathbf{r}_i}$$

where  $V$  is the total volume of the system.

For collinear order, where the spin projection is only on the  $z$  axis, the spin vector can be replaced by  $S_i$ . If we imagine the spin configuration to be broken up into domains, indexed by a label  $\alpha$ , say, then, for collinear phases,  $\vec{f}(\mathbf{q}) = \hat{z}f(\mathbf{q})$  and :

$$f(\mathbf{q}) = \sum_{\alpha} \sum_{\mathbf{r}_i^{\alpha} \in \alpha} S_i e^{i\mathbf{q} \cdot \mathbf{r}_i^{\alpha}} = \sum_{\alpha} f_{\alpha}(\mathbf{q}) \quad (4.1)$$

where the sum runs over the domains, and the  $\mathbf{r}_i^{\alpha}$  are coordinates within a domain  $\alpha$ . This shows that  $f(\mathbf{q})$  gets additive contributions from various domains, with phase factors that we will soon clarify. The formulation above holds as long as (a) there is no significant non collinearity and (b)  $\xi \gg 1$ , *i.e.*, we can ignore *interfacial* spins which may be hard to assign to any particular domain.

#### 4.4.1 A type order

For weak to moderate antisite disorder we observe that the system prefers ferromagnetic stripes along any single diagonal, albeit with phase slippage between the stripes to accommodate the effect of  $J_{AF}$ . This is true for  $S = 0.98, 0.76$  and  $0.50$ , the first three columns in the middle row in Figure 4.5 . Domains which are translated with respect to the reference domain have relative displacement  $\delta\mathbf{r}_{\alpha} = \hat{x}a_0$  or  $\hat{y}a_0$ . The order *within* all domains is similar. So, the contribution of each domain at the ordering wavevector,  $\mathbf{Q}$ , will be proportional to the domain volume  $V_{\alpha}$ , and involve a phase factor, *i.e.*,

$$f_{\alpha}(\mathbf{Q}) = V_{\alpha} e^{i\mathbf{Q} \cdot \delta\mathbf{r}_{\alpha}} f_0(\mathbf{Q})$$

where  $f_0(\mathbf{Q})$  is the normalised reflection in the perfectly ordered system. For the  $\mathbf{Q} = \mathbf{Q}_{A1} = \{\pi/2, \pi/2\}$  peak, the phase factor is  $e^{i\pi/2}$  irrespective of whether the domain is  $x$  displaced or  $y$  displaced. So, all the *mislocated* sites, grouped into domains, contribute  $V_{mis} e^{i\pi/2} f_0(\mathbf{Q})$ , where  $V_{mis}$  is the total volume of mislocated regions.

Adding the contribution from the majority domains, which are undisplaced, we obtain:

$$f(\mathbf{Q}_{A1}) = ((V - V_{mis}) + V_{mis} e^{i\pi/2}) f_0(\mathbf{Q}_{A1})$$

Remembering that  $V_{mis}/V = x$ , the volume normalised structure factor peak is

$$D(\mathbf{Q}_{A1}) = |(1-x) + e^{i\pi/2}x|^2 = \frac{1}{2}(1+S^2)$$

This is roughly consistent with the  $S$  dependence of the  $T \rightarrow 0$  structure factor in Figure 4.6 (a). It is *distinctly slower* than the suppression of order in the ferromagnet, where  $D(\mathbf{Q}_F) \sim S^2$ .

At larger ASD however, the system has short stripes oriented along *both* diagonals, see middle row last column in Figure 4.5. These domains have magnetic peaks at  $\mathbf{Q}_{A3}, \mathbf{Q}_{A4}$  and not at  $\mathbf{Q}_{A1}, \mathbf{Q}_{A2}$ . Even assuming that the *majority* domains all contribute  $(1-x)f_0(\mathbf{Q}_{A1})$ , we notice that the mislocated regions require classification into two groups: those contributing at  $\mathbf{Q}_{A1}, \mathbf{Q}_{A2}$  with volume fraction  $y$ , say, and those at  $\mathbf{Q}_{A3}, \mathbf{Q}_{A4}$  with volume fraction  $x-y$ . In that case the peak at  $\mathbf{Q}_{A1}$  would be

$$D(\mathbf{Q}_{A1}) = |(1-x) + e^{i\pi/2}y|^2$$

The  $(x-y)$  fraction makes no contribution to the peak, and that weight is *lost*. Notice that  $x \geq y \geq 0$ , and it is not possible to write  $D(\mathbf{Q}_{A1})$  purely in terms of  $S$ . We could write the expressions for the structure factor at the other three  $\mathbf{Q}$  as well, and they will all depend on both  $x$  and  $y$ . This is a general feature of magnetic states where the order can locally pick out different orientations.

We can make some headway in the strong disorder limit,  $x = 1/2, S = 0$ , by assuming that there are four kinds of domains, with roughly equal area. There would be two families of  $\{\mathbf{Q}_{A1}, \mathbf{Q}_{A2}\}$  domains, each with 1/4 the system volume, and a relative phase shift  $\pm\pi/2$ . Similarly there would be two families of  $\{\mathbf{Q}_{A3}, \mathbf{Q}_{A4}\}$  domains, each with volume 1/4, and relative phase shift  $\pm\pi/2$ . In this case the  $\mathbf{Q}_{A1}$  peak, for example, in  $D(\mathbf{Q})$  will be:

$$D(\mathbf{Q}_{A1}) = |1/4 + e^{i\pi/2}/4|^2 = 1/8$$

This is not very far from  $D(\mathbf{Q}_{A1}) \sim 0.1$  that we obtain from the Monte Carlo. Other peaks, at  $\mathbf{Q}_{A2}, \mathbf{Q}_{A3}$ , *etc*, would have similar magnitude.

#### 4.4.2 G type order

G type order occurs at the combination  $\{\mathbf{Q}_{G1}, \mathbf{Q}_{G2}\} : \{\{0, \pi\}, \{\pi, 0\}\}$ . As before the relative displacement of the domains can be only  $\hat{x}a_0$  or  $\hat{y}a_0$ . Suppose we are

computing the structure factor at  $\mathbf{Q}_{G1}$  then all domains will contribute, but with following phase factors: zero if the domain is not mislocated ( $\delta\mathbf{r} = 0$ ), zero again if the domain is  $\hat{x}$  displaced, and  $e^{i\pi} = -1$  if the domain is  $\hat{y}$  displaced.

In *two domain* systems, as in the second column in Figure 4.5 , the mislocated domain is either  $x$  displaced or  $y$  displaced. For copies with  $x$  displacement the contribution at  $\mathbf{Q}_{G1}$  will be  $|(1 - x) + x|^2 = 1$ , while for  $y$  displacement it will be  $|(1 - x) + e^{i\pi}x|^2 = (1 - 2x)^2 = S^2$ . Averaging the *structure factor* over copies would lead to  $D(\mathbf{Q}_{G1}) = (1/2)(1 + S^2)$ . This is roughly what we observe in our Figure 4.6 (b) at  $T = 0$ .

In large systems, where there will be many domains, we can assume that half the mislocated domains are  $x$  displaced and half  $y$  displaced. In that case the structure factor would be

$$D(\mathbf{Q}_{G1}) = |(1 - x) + x/2 + e^{i\pi}x/2|^2.$$

Using  $1 - 2x = S$  this leads to

$$D(\mathbf{Q}_{G1}) = (1/4)(1 + S)^2.$$

For  $S \rightarrow 0$  this gives 0.25, not far from  $\sim 0.20$  that we obtain from our configurations.

This reveals that for both A and G type order even when *half the sites are mislocated, i.e.*, one has maximal antisite disorder, there is a surviving peak in the structure factor. All these of course assumed that the structural pattern had a high degree of spatial correlation so that one can meaningfully talk of domains. We should have  $1 - p \ll 1$ , or structural correlation length  $\xi \gg a_0$ . If the structures were fragmented to a random alloy then the results above would not hold. We have checked this explicitly.

## 4.5 Transport with antisite disorder

All the three phases, ferromagnetic, A type, and G type, in the 2D double perovskite model are metallic in the clean limit. The electronic states are extended, and there is a finite density of states at the Fermi level. In the absence of antisite disorder the resistivity,  $\rho(T)$ , in all three have similar temperature dependence.

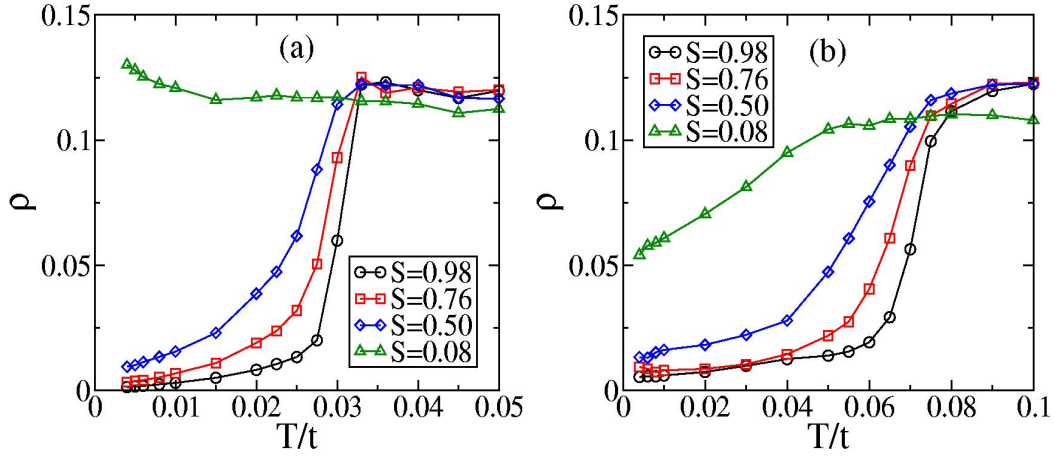


Figure 4.7: Resistivity in the A type and G type phases with antisite disorder. The results for each  $S$  are averaged over 10 realisations of disorder.

The resistivity increases rapidly as temperature increases towards  $T_c$ , Figure 4.7 and our earlier work [13] on the ferromagnet, and *saturates* at high temperature. A Fisher-Langer type [14] phenomenology can qualitatively describe the transport.

Weak disorder leads to an increase in the residual resistivity of the A and G type phases, see Figure 4.7, as observed earlier for the ferromagnetic case. The sharp resistive transition observed in the clean limit ( $S = 0.98$ ) is also gradually broadened. There is however a key difference with respect to the ferromagnetic phase when we move to strong disorder.

In the 2D case our results [13] on the ferromagnet suggest an insulating  $T = 0$  state beyond a critical disorder, with  $d\rho/dT < 0$ . At the highest disorder,  $S = 0.08$ ,  $\rho(T)$  in the A type antiferromagnet remains essentially flat down to  $T = 0$ , while in the G type phase there is still a low temperature *downturn*. While these are finite size results, we argue below why there is an intrinsic reason for transport in the antiferromagnetic phases to be less sensitive to antisite disorder and domain formation. This is related to the nature of electronic wavefunctions in these phases. We consider the two phases in succession below.

In the A type phase the core spin order involves diagonal stripes. Up-spin electrons delocalise on down-spin stripes which involve one B diagonal and the two adjacent B' lines. Down-spin electrons delocalise on up-spin stripes. The down

and up stripes share a common  $B'$  line. The essential feature is that the electronic wavefunctions are quasi-one dimensional. The introduction of antisite disorder leads to two effects: (i) it hinders propagation along the stripe, and (ii) allows scattering between the stripes leading to an *expansion* of the wavefunction in the transverse direction. On its own, the first effect would have suppressed conduction, but the new matrix element between stripes allows a transverse pathway for delocalisation. In contrast to the FM case there is no *confinement* of the wavefunctions to specific domains, and the two competing effects above lead to a finite resistivity (at least a much weaker upturn) even at strong disorder.

In the clean G type phase the system can be viewed as two interpenetrating square lattices, one with up spin B sites, the other with down spin B sites. The electrons delocalise via the  $B'$  sites, and each  $B'$  site hosts both up and down electron states. Electrons in both spin channels are delocalised over the whole system in the absence of antisite disorder. The presence of antisite domains leads to scattering but no confinement of electrons to the domains. Due to the inherently 2D character of the G type electronic states, in contrast to quasi-1D for A type, the system has a lower resistivity.

We contrast the resistivity of the three phases in Figure 4.8 for the case of maximum disorder that we have studied. These are configurations with  $S \sim 0.08$ , but, as we have noted, with a fairly high degree of local correlation. The ferromagnet has a clear low temperature upturn due to the confinement of electrons into domains or pathways created by the antisite disorder. The A and G type electronic states, in either spin channel, are *not confined* to the magnetic/structural domains, and the resistivity remains comparatively lower. The high temperature resistivity is determined by spin disorder scattering, depends weakly on carrier density (the FM, A and G phases have different  $n$ ), and is almost temperature independent. In the analysis above we have ignored the possibility of additional *weak localisation* effects that may arise (at very large lengthscales) due to the 2D nature of the problem. In 3D of course such effects would be absent. We also studied the strong disorder (small  $S$ ) situation in the presence of uncorrelated antisites. On the resistivity we do not find a significant difference between correlated and uncorrelated antisite disorder. At small disorder (large  $S$ ) however we expect that correlated disorder, which involves a few minority domains, will lead

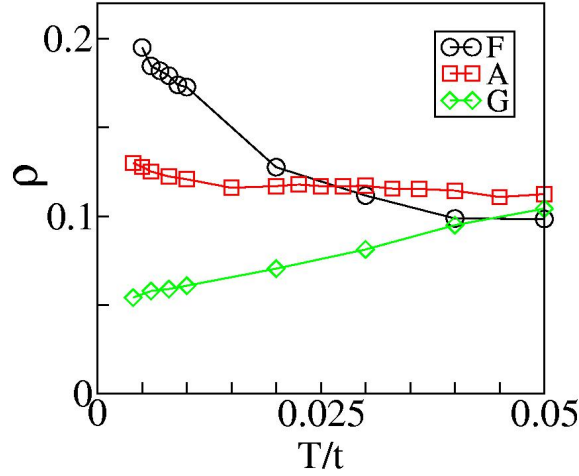


Figure 4.8: Comparison of the resistivity in the FM, A and G type correlated phases in samples with the lowest degree of order  $S = 0.08$ .

to weaker scattering and resistivity compared to randomly distributed antisites.

## 4.6 Phase coexistence

In the clean limit, the increase of electron density by doping the ferromagnet would encounter a window of phase separation. A homogeneous state is not allowed for  $0.45 \leq n \leq 0.58$  and this (idealised) system would break up into macroscopic regions having densities  $n \sim 0.45$  and  $n \sim 0.58$ . This pathology is avoided by long range Coulomb interactions or quenched disorder. For the anti-site disordered configurations that we are considering the antisite disorder itself generates an effective disorder that controls the pattern of spatial coexistence.

Figure 4.9 shows the magnetic correlations in a fixed antisite background for changing electron density. The leftmost panel is the structural pattern, showing the antisite domains. The next five snapshots correspond to increasing chemical potential,  $\mu$ , and consequently the electron density. The first panel in this set is a (domain) ferromagnet at  $n < 0.45$ , the second shows emergence of stripes along with the ferromagnetic regions. The ferromagnetic regions shrink and the linelike patterns become more prominent in the third panel. The fourth and fifth panel complete the evolution, with ferromagnetic correlations completely replaced by stripes (of both orientation) as in the middle row fourth column in Figure 4.5 .

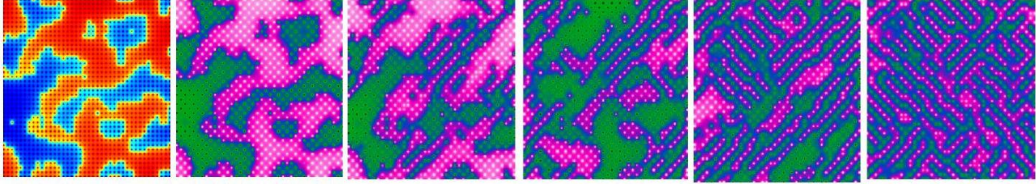


Figure 4.9: Magnetic correlations with increasing electron density as one traverses the coexistence regime in an antisite disordered background. The first panel shows the structural pattern arising from the ASD. Panel 2 shows the spin correlations at  $\mu = \mu_{FM} = -1.8$ , where the ground state is a (domain) ferromagnet. The extreme right is for  $\mu = \mu_{AF} = -1.4$ , where the system has only A type AF correlations. As  $\mu$  increases from  $\mu_{FM}$  to  $\mu_{AF}$  the pattern exhibits coexistence of short range ferromagnetic and antiferromagnetic correlations.

The evolution of the particle density with  $\mu$ , and the rapid change near the phase separation window, are shown in Figure 4.10 .

Had the antisite disorder been uncorrelated there would be no structural domains in Figure 4.9 . Since the *coexisting* phases basically inhabit the small domains, which are *ordered* in the intra-domain lengthscale, the absence of domains would wipe out the coexistent pattern. In its place we would have a nanoscale magnetic glass. The correlated disorder therefore enables the coexistent pattern to emerge and survive.

## 4.7 Discussion

While our study has some value in clarifying the interplay of antisite domains with delocalisation driven antiferromagnetism, our model differs from the *real* double perovskites in the following aspects.

(i) *Dimensionality*: The double perovskites are three dimensional and, in an ordered structure, the B and B' alternate along each axis. The effective B lattice is FCC, and therefore geometrically frustrated. This leads to a complex variety of phases [4], collinear at low filling and non collinear near half-filling. Capturing these phases via a Monte Carlo calculation is non trivial even in the absence of

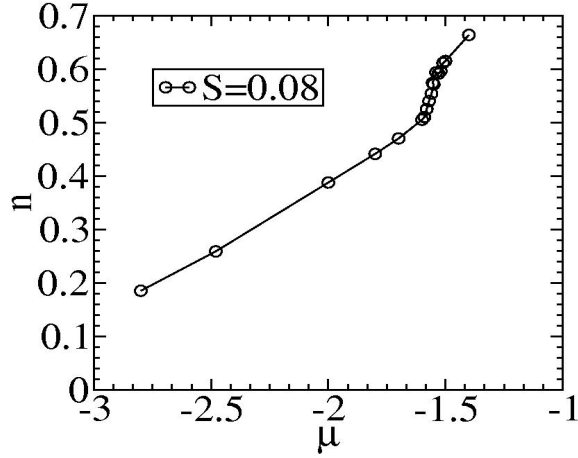


Figure 4.10: The variation of electron density with chemical potential as the FM to A type AF crossover is traversed in a high ASD sample ( $S = 0.08$ ).

antisite disorder. So, while the antisite domain pattern can be readily generated in 3D as well, solving for the magnetic structure accurately remains a difficult task. This has prevented us from studying the 3D disordered model directly. However, using the insight gained from the 2D system, and knowing the ordering wavevector (and the degeneracy of the ordering pattern) allows us to make some prediction for 3D as well. For instance, the A type phase in 3D involves  $\{1, 1, 1\}$  planes, ferromagnetic within the plane and AF between neighboring planes. There are *four families of such planes* in 3D, in contrast to *two families of lines* in 2D, each indexed by a couple of wavevectors. One such pair, for example, is  $\{\{\pi/2, \pi/2, \pi/2\}, \{3\pi/2, 3\pi/2, 3\pi/2\}\} = \{\mathbf{Q}_1, \mathbf{Q}_2\}$ , say. The effect of a small degree of mislocation on a state primarily ordered at these wavevectors would be the suppression  $D(\mathbf{Q}) \sim \frac{1}{2}(1 + S^2)$ . At large disorder, small  $S$ , the 3D residual value would be smaller than the  $\frac{1}{8}$  predicted in 2D due to the larger number of ordering possibilities in 3D.

(ii) *Effect of electron-electron interactions:* Some authors have invoked Hubbard interactions on the B and B' sites when studying the double perovskites [15]. In our analysis of the impact of antisite disorder in the ferromagnetic regime, the results of such an approach closely matches our own. In the present, antiferromagnetic, context we do not know of any calculations invoking Hubbard interactions. The Hund's coupling suffices to generate the non trivial magnetic

phases and, we feel, additional interactions should be brought in when we have adequate understanding of the vital role of disorder.

(iii) *Nature of antisite disorder on electron doping:* In a material like SFMO electron doping can be accomplished by substituting La for Sr, *i.e.*, compositions like  $\text{Sr}_{2-x}\text{La}_x\text{FeMoO}_6$ . In stoichiometric SFMO, it seems established that the primary source of disorder is Fe-Mo mislocation. However, substituting La for Sr also generates *A site* disorder in the perovskite network and in principle the doped La might sit preferentially near Fe or Mo. If that happens it would lead to an additional potential on the Fe and Mo sites. We need guidance from experiments or *ab initio* theory to model this A site disorder.

## 4.8 Conclusions

We have studied the survival of the antiferromagnetic double perovskite phases in the presence of spatially correlated antisite disorder. We observe that antisite disorder affects the antiferromagnetic order much less strongly than it affects ferromagnetism. For a given structural order parameter  $S$ , the A type antiferromagnetic structure factor follows  $D_A \sim (1 + S^2)/2$ , in contrast to  $D_F \sim S^2$  in the ferromagnet, while the G type phase follows  $D_G \sim (1 + S)^2/4$ . So, despite the possibility of large antisite disorder at the high electron doping needed to observe the antiferromagnetic phases, there is certainly hope of observing these magnetic structures. The antiferromagnetic states are metallic, and the electronic wavefunctions in these phases continue to be spatially extended even at large disorder. Antisite disorder increases the residual resistivity, but, unlike the ferromagnet, we did not observe any insulating regime. The field response of these antiferromagnetic metals is also fascinating, and is discussed in the next chapter.

# Bibliography

- [1] E. Dagotto, *Science* **309**, 257 (2005).
- [2] Y. Tokura, *Rep. Prog. Phys.* **69**, 797 (2006).
- [3] P. Sanyal and P. Majumdar, *Phys. Rev. B* **80**, 054411 (2009).
- [4] R. Tiwari and P. Majumdar, *arXiv:1105.0148* (2011).
- [5] A. Chattopadhyay and A. J. Millis, *Phys. Rev. B* **64**, 024424 (2001).
- [6] J. L. Alonso, L. A. Fernandez, F. Guinea, F. Lesmes, and V. Martin-Mayor, *Phys. Rev. B* **67**, 214423 (2003).
- [7] P. Sanyal, H. Das, and T. Saha-Dasgupta, *Phys. Rev. B* **80**, 224412 (2009).
- [8] T. K. Mandal, C. Felser, M. Greenblatt, and J. Küble, *Phys. Rev. B* **78**, 134431 (2008).
- [9] D. Sanchez, J. A. Alonso, M. Garcia-Hernandez, M. J. Martinez-Lopez, M. T. Casais, and J. L. Martinez, *J. Mater. Chem.* **13**, 1771 (2003).
- [10] S. Jana, C. Meneghini, P. Sanyal, S. Sarkar, T. Saha-Dasgupta, O. Karis, and S. Ray, *arXiv:1204.3378* (2012).
- [11] V. N. Singh and P. Majumdar, *Eur. Phys. J. B* **83**, 147 (2011).
- [12] Y. H. Huang, M. Karppinen, H. Yamauchi, and J. B. Goodenough, *Phys. Rev. B* **73** (2006) 104408.
- [13] V. N. Singh and P. Majumdar, *Europhys. Lett.* **94**, 47004 (2011).
- [14] M. E. Fisher and J. S. Langer, *Phys. Rev. Lett.* **20**, 665 (1968).
- [15] B. Aguilar, O. Navarro, and M. Avignon, *Europhys. Lett.* **88**, 67003 (2009).



# Chapter 5

## Field Response in Antiferromagnetic Metals

**Chapter summary:** In this chapter we discuss the field response expected in an antiferromagnetic double perovskite metal. While the zero field resistivity is unremarkable in such a metal, we find that the magnetoresistance can be very large and positive. This can be a direct indicator of the metallic antiferromagnetic state. Beyond a modest field, needed for suppression of long range antiferromagnetic order, the system shows more than tenfold increase in resistivity near  $T_c$  in a structurally ordered system. The ratio continues to be almost twofold even in systems with  $\sim 25\%$  antisite disorder. The effect occurs because an applied field suppresses long range antiferromagnetic order leading to a state with *short range antiferromagnetic correlations* in the field induced ferromagnetic background. These antiferromagnetic fluctuations generate strong electronic scattering and a resistivity that can be much larger than the ordered antiferromagnetic metal. This mechanism is quite general, complementary to the colossal negative magnetoresistance process, and should operate in other local moment antiferromagnetic metals as well.

### 5.1 Introduction

There has been intense focus over the last two decades on magnetic materials which display large negative magnetoresistance (MR) [1–3]. In these systems, typically, an applied magnetic field reduces the spin disorder leading to a suppres-

sion of the resistivity. The field may even drive an insulator-metal transition leading to ‘colossal’ magnetoresistance [1]. Large *positive* magnetoresistance is rarer, and seems counterintuitive since an applied field should reduce magnetic disorder and enhance conductivity. We illustrate a situation in double perovskite [4] metals, where an applied field can lead to enormous positive magnetoresistance. The underlying principle suggests that local moment antiferromagnetic (AFM) metals [5–12], at strong coupling, should in general be good candidates for such unusual field response.

Like in other correlated oxides [13], the magnetic order in the double perovskites is expected to be sensitive to electron doping as we have discussed in detail earlier. It has been suggested [14–16] that the ferromagnetic metal can give way to an AFM metal on increasing electron density. The AFM order is driven by electron delocalisation and has lower spatial symmetry than the parent structure. The conduction path in the AFM background is low dimensional and easily disrupted.

There is ongoing effort [17,18] to obtain an AFM metal by electron doping the ferromagnetic metal. Although there is no clear evidence yet of the occurrence of an AFM metal, there is some signature of a non ferromagnetic metal in the heavily electron doped  $\text{Sr}_2\text{FeMoO}_6$  [18]. The problems are twofold:

1. *Antisite defects*: in a material like  $\text{Sr}_2\text{FeMoO}_6$ , substituting La for Sr to achieve a higher electron density in the Fe-Mo subsystem tends to make the Fe and Mo ionic sizes more similar (due to resultant valence change), increases the likelihood of antisite disorder, and suppresses magnetic order.
2. *Detection*: even if an AFM state is achieved, confirming the magnetic order is not possible without neutron scattering. The zero field resistivity is unfortunately quite similar [19] to that of the ferromagnetic metal.

## 5.2 Field response in ordered AFM metal

Let us first discuss the thermal and field effects in the structurally ordered double perovskite before examining the effect of antisite disorder [20]. As we have seen in the last chapter, upon increasing electron density the ground state changes from a ferromagnetic metal to a phase with stripe-like order. The ‘stripe’ phase involves

ferromagnetic B lines coupled antiferromagnetically in the transverse direction. We call this the *A type* phase. At even higher electron density there is a more traditional antiferromagnetic phase, where an up spin B ion, say, is surrounded by four down spin B ions, and *vice versa*: the *G type* phase. We focus here on the A type phase since it has a simple 3D counterpart and occurs at physically accessible electron density.

We have used field cooling (FC) as well as zero field cooling (ZFC) protocols. For zero field cooling the system is cooled to the target temperature at field  $h/t = 0$  and then a field is applied. We calculate the resistivity and the magnetic structure factor peaks and also keep track of spatial configurations of spins.

The A type pattern has *two possible orientations* of the stripes, either from bottom left to top right, or from bottom right to top left. These are the two *diagonals* in 2D. The first corresponds to peaks in the structure factor  $D(\mathbf{q})$  at  $\{\mathbf{Q}_{A1}, \mathbf{Q}_{A2}\}$ , and the second to peaks at  $\{\mathbf{Q}_{A3}, \mathbf{Q}_{A4}\}$ . For reference,  $\mathbf{Q}_{A1} = \{\pi/2, \pi/2\}$ ,  $\mathbf{Q}_{A2} = \{3\pi/2, 3\pi/2\}$ ,  $\mathbf{Q}_{A3} = \{\pi/2, 3\pi/2\}$ ,  $\mathbf{Q}_{A4} = \{3\pi/2, \pi/2\}$ . The ferromagnetic peak in  $D(\mathbf{q})$  are at  $\mathbf{Q}_{F1} = \{0, 0\}$  and  $\mathbf{Q}_{F2} = \{\pi, \pi\}$ . The ordered configurations lead to peaks at *two* wavevectors since the model has both magnetic and non-magnetic sites and our wavevectors are defined on the overall B-B' lattice.

### 5.2.1 Field cooling

Let us first examine the field cooling results in resistivity, Figure 5.1 . Cooling at  $h/t = 0$  leads to a sharp drop in resistivity at  $T = T_c^0 \sim 0.032$ , where  $T_c^0$  is the zero field transition temperature, and  $\rho(T) \rightarrow 0$  as  $T \rightarrow 0$ . Cooling at  $h/t = 0.01$  leads to a small suppression in  $T_c$  but the trend in  $\rho(T)$  remains similar to  $h/t = 0$ . Between  $h/t = 0.01$  and  $h/t = 0.02$ , however, there is a drastic change in  $\rho(T)$ , and, as we will see later, in the magnetic state. The primary effect is a sharp increase in the  $T < T_c^0$  resistivity, with the  $T \rightarrow 0$  resistivity now being almost 40% of the paramagnetic value. Even at this stage it is clear that  $\rho(T, h)/\rho(T, 0)$  can be very large as  $T \rightarrow 0$  and is  $\sim 4$  for  $T \sim T_c^0$  and  $h/t = 0.02$ . Increasing the field even further leads to a reduction in  $\rho(T)$  over most of the temperature window since the field promotes a ferromagnetic state suppressing the antiferromagnetic fluctuations.

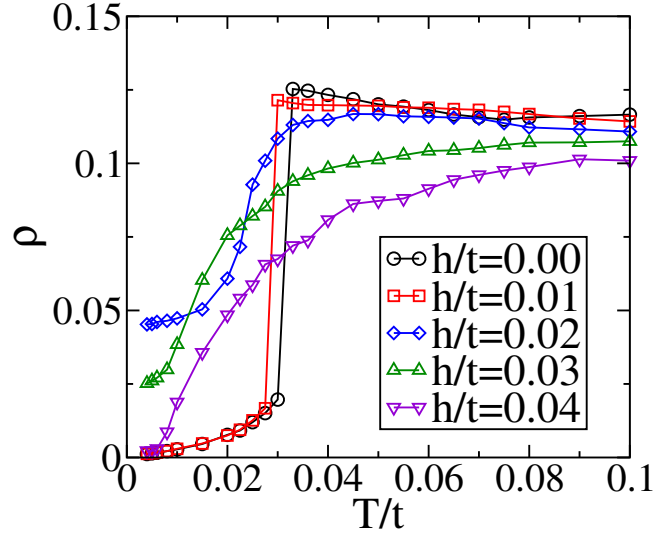


Figure 5.1: The resistivity  $\rho(T)$  in the absence of antisite disorder for cooling in different applied fields. For temperatures below the zero field transition,  $T_c^0$ ,  $\rho(T)$  increases on applying a field, and for  $T > T_c^0$   $\rho(T)$  decreases on applying a field. The ratio  $\rho(T,h)/\rho(T,0)$  can be very large as  $T \rightarrow 0$  in this field cooling situation.

### 5.2.2 Zero field cooling

Now, we will study the impact of the magnetic field within the ZFC scheme. Figure 5.2 shows the result of applying a field after the cooling the system to four different temperatures, (i) slightly above  $T_c^0$ , (ii) slightly below  $T_c^0$ , (iii) to  $T_c^0/2$  and (iv) to  $T_c^0/4$ .

For  $T > T_c^0$ , the zero field resistivity is already large and the applied field mainly suppresses the antiferromagnetic thermal fluctuations, leading to a gradual fall in the resistivity. This is weak negative magnetoresistance.

Below  $T_c^0$  (where there is already noticeable antiferromagnetic order) and at  $T_c^0/2$ , the resistivity remains almost unchanged till some value  $h_c(T) \sim 0.01$ , then there is a sharp increase in resistivity, with a peak in the ratio  $\rho(T,h)/\rho(T,0)$  around  $h/t \sim (0.02 - 0.03)$  and a fall thereafter. This is consistent with the trends seen in Figure 5.1. At  $T_c^0/2$  the ratio reaches a maximum  $\sim 12$ .

At lower temperature  $T_c^0/4$  the field appears to have a much weaker effect, mainly because the update mechanism that we adopt does not allow a cooperative

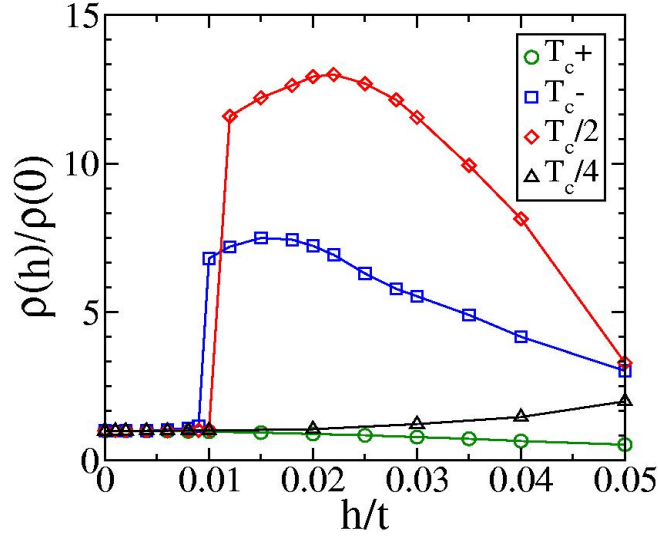


Figure 5.2: Field dependence of resistivity at different temperatures following a zero field cooling protocol. For  $T = T_c^+$  (just above  $T_c$ ) the zero field resistivity is already large and  $\rho$  decreases slightly with  $h$  due to suppression of spin disorder. For  $T = T_c^-$  (just below  $T_c$ ) and at  $T_c/2$  there is a sharp increase in resistivity at  $h/t \sim 0.01$ , with a peak around  $h/t \sim 0.02 - 0.03$  and a fall thereafter. This is consistent with the trends seen in Figure 5.1. At  $T = T_c/4$  this ZFC scheme does not manage to create competing magnetic structures for  $h/t \sim 0.05$ , possibly due to metastability of the parent AFM pattern. The field induced switching is therefore easiest achieved between  $T_c/2$  and  $T_c$ .

switching of the antiferromagnetic state at low  $T$  till very large fields. The field induced switching is therefore easiest achieved between  $T_c^0/2$  and  $T_c^0$ . Overall, there is a window of  $T$  over which a moderate magnetic field can lead to a several fold rise in resistivity.

A first understanding of the rise in resistivity can be obtained from the magnetic snapshots of the system at  $T = T_c^0/2$  in Figure 5.3. We plot the correlation  $f_i = \mathbf{S}_0 \cdot \mathbf{S}_i$  in an equilibrium magnetic snapshot, where  $\mathbf{S}_0$  is a reference spin (bottom left corner) and  $\mathbf{S}_i$  is the spin at site  $\mathbf{R}_i$ . The left panel is at  $h/t = 0$  and shows a high level of A type correlation (stripe like pattern). This is a *low dimensional* electron system since the electron propagation is along the one

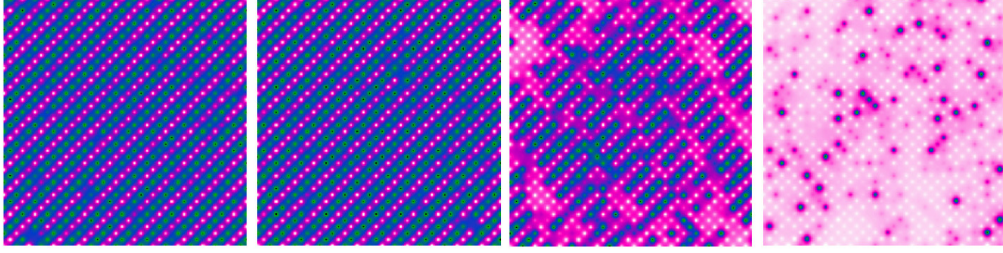


Figure 5.3: Evolution of spin correlations in the clean system in response to a magnetic field. The plot shows  $f_i = \mathbf{S}_0 \cdot \mathbf{S}_i$  in a magnetic snapshot, where  $\mathbf{S}_0$  is a reference spin (bottom left corner).  $T = T_c^0/2$  and the fields are, from left to right,  $h/t = 0, 0.008, 0.02, 0.05$ .

dimensional stripes in this 2D system. The stripe pattern has a high degree of order so the scattering effects and resistivity are low. The second panel is at  $h/t = 0.008$ , just below field induced destruction of antiferromagnetic order, and the pattern is virtually indistinguishable from that in the first panel.

The third panel in Figure 5.3 is at  $h/t = 0.02$  where the applied field has suppressed *long range* A type order. However, there are strong A type fluctuations that persist in the system and they lead to a pattern of short range ordered A type patches with competing orientations,  $\{\mathbf{Q}_{A1}, \mathbf{Q}_{A2}\}$  and  $\{\mathbf{Q}_{A3}, \mathbf{Q}_{A4}\}$ , in a spin polarised background. This patchwork leads to a high resistivity, higher than that in leftmost panel, since the ferromagnetic paths are fragmented by intervening A type regions, while the A type regions are poorly conducting due to their opposite handedness. In the last panel the field,  $h/t = 0.05$ , is large enough so that even the antiferromagnetic fluctuations are wiped out and the spin background is a 2D ferromagnet with extremely short range inhomogeneities. The resistance here is significantly below the peak value.

Let us summarise the physical picture that emerges in the non disordered system before analysing the effect of antisite disorder. The ingredients of the large magnetoresistance are the following:

1. An antiferromagnetic metallic phase, without too much quenched disorder so that the resistivity in the magnetically ordered state is small.
2. Field induced suppression of the antiferromagnetic order at  $h = h_c(T)$ ,

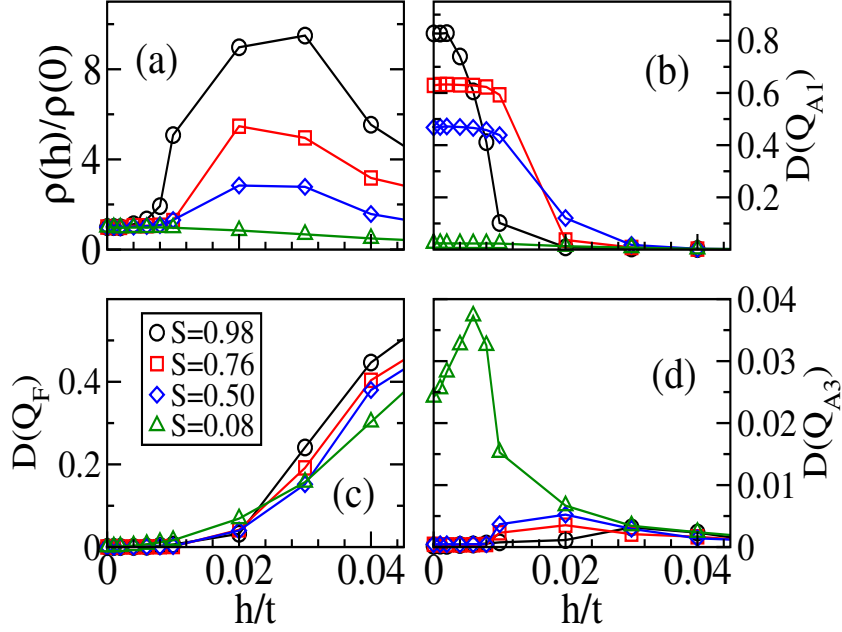


Figure 5.4: Field response in the presence of antisite disorder. The temperature is  $T = T_c^0/2$ , where  $T_c^0$  is the  $T_c$  at  $h/t = 0$  in the non disordered system. The results are obtained via ZFC. (a) Field dependence of resistivity, normalised to  $h/t = 0$ . (b) Magnetic structure factor at the major antiferromagnetic peak  $\mathbf{Q}_{A1}$ . The value is same at  $\mathbf{Q}_{A2}$  also. (c) Growth in the ferromagnetic structure factor with  $h$ . (d) Growth in the complementary antiferromagnetic peak  $\mathbf{Q}_{A3}$ , result same for  $\mathbf{Q}_{A4}$ .

say, replacing the ordered state with antiferromagnetic correlated spins in a ferromagnetic background, leading to a high resistivity state.

Let us highlight the contrast to the standard negative magnetoresistance scenario, where an applied field pushes the system from a spin disordered state to a spin ordered state. Here the applied field pushes the ordered (antiferromagnetic) state towards spin disorder, before the high field polarised state occurs. Our concrete results are in the case of a 2D double perovskite model and a stripe-like ground state, but the principle above is far more general and should apply to other non-ferromagnetic ordered states in two or three dimensions, and to microscopic models that are very different from the double perovskites. We will discuss this issue at the end.

### 5.3 Response in antisite disordered AFM metals

Defects are inevitable in any system and in particular one expects antisite disorder in the double perovskites. The concentration of such defects may actually increase on electron doping a material like  $\text{Sr}_2\text{FeMoO}_6$ , due to the valence change, and we need to check if the large magnetoresistance is wiped out by weak disorder. The presence of antisite disorder affects the zero field magnetic state itself, as we have discussed elsewhere [19], and the field response has to be understood with reference to this  $h = 0$  state.

Figure 5.4 shows the resistivity ratio  $\rho(h)/\rho(0)$  at  $T = T_c^0/2$ , in panel (a), and the field dependence of structure factor peaks in panels (b)-(d). Figure 5.5 first column shows the structural motifs on which the magnetism is studied.

Down to  $S = 0.50$  the ratio  $\rho(h)/\rho(0)$  has a pattern similar to the clean case, Figure 5.2, but the peak ratio reduces to  $\sim 3$  for  $S = 0.50$ . There is a corresponding suppression in the principal antiferromagnetic peak  $\mathbf{Q}_{A1}$  and an enhancement of the ferromagnetic peak  $\mathbf{Q}_F$ . The complementary antiferromagnetic peak  $\mathbf{Q}_{A3}$  slowly increases with  $h$ , has a maximum around  $h/t = 0.02$  (where the disconnected antiferromagnetic domains exist) and falls at large  $h$  as the system becomes ferromagnetic overall. The trend that we had observed in the clean limit is seen to survive to significant disorder. At  $S = 0.08$ , where the B-B' order is virtually destroyed, the  $h/t = 0$  state, Figure 5.5 last row, has no long range antiferromagnetic order. It is already a high resistivity state and an applied field actually leads to weak negative magnetoresistance.

Since a real double perovskite has a three dimensional structure, we have also studied a one band three dimensional model. In contrast to the two dimensional case, where the effective magnetic lattice is bipartite, the three dimensional lattice has a geometrically frustrated face centered cubic structure. This promotes various non-collinear phases, studied in detail elsewhere [16]. We had tried to study the impact of a magnetic field on these phases. These results, unfortunately, are still preliminary and more work is needed to improve their quality.

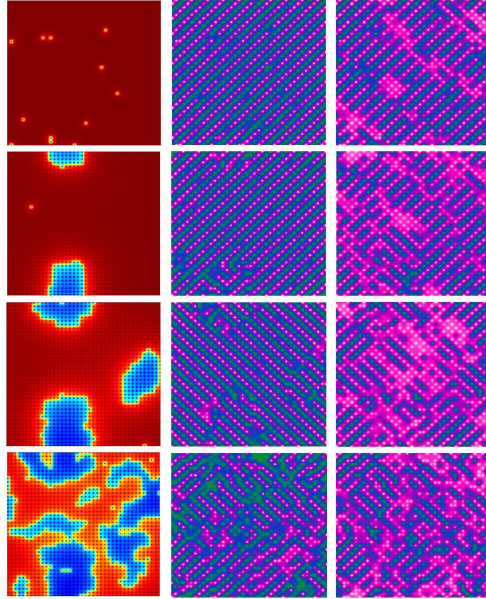


Figure 5.5: Field response in the antisite disordered systems at  $T = T_c^0/2$ , for the  $S$  values in Figure 5.4 . The left panels indicate the structural domains. The middle column shows the spin correlations at  $h/t = 0$ , note that rows 1-3 show significant A type order, while the pattern in the 4th row has AFM domains of both orientations. The right column shows the spin correlations at  $h/t = 0.02$ . In rows 1-3 the AFM pattern gets fragmented and FM regions show up. In row 4 the finite field pattern is not significantly different from the  $h/t = 0$  case. Overall, the field enhancement of *spin disorder* is large in the first three cases but modest at strong antisite disorder.

## 5.4 Discussion

Let us place our results in the general context of antiferromagnetic metals.

### 5.4.1 Earlier theory

We are aware of one earlier effort [21] in calculating the magnetoresistance of antiferromagnetic metals (and semiconductors), assuming electrons weakly coupled to an independently ordering local moment system. Indeed, the authors suggested that antiferromagnetic *semiconductors* could show positive magnetore-

sistance. Our framework focuses on field induced suppression of long range antiferromagnetic order, rather than perturbative modification, and the positive magnetoresistance shows up even in a *high density* electron system. The electron-spin coupling is also (very) large,  $J/t \gg 1$ , and cannot be handled within Born scattering.

### 5.4.2 Experimental results

The intense activity on oxides has led to the discovery of a few antiferromagnetic metals, *e.g.*, in the manganite ( $\text{La}_{0.46}\text{Sr}_{0.54}\text{MnO}_3$ ) [5], in  $\text{CaCrO}_3$  [6], in the ruthenates ( $\text{Ca}_3\text{Ru}_2\text{O}_7$ ) [7–10], and in the heavy-fermions ( $\text{CeRhIn}_5$ ) [11,12]. Of these for the manganites and  $\text{CaCrO}_3$  (where the resistivity is too large), we are not aware of magnetoresistance results across the field driven transition.  $\text{Ca}_3\text{Ru}_2\text{O}_7$  and  $\text{CeRhIn}_5$  show large increase in the resistivity with the field induced growth of ferromagnetic order, as shown in the Figure 5.6 . These are local moment antiferromagnetic metals. On application of a magnetic field there is suppression of long range antiferromagnetic order, leading possibly to a state with antiferromagnetically correlated spins in a ferromagnetic background. This may be responsible for the high resistivity that is observed. Neutron diffraction in the presence of a magnetic field should be able to conform this scenario.

### 5.4.3 Qualitative analysis

The information about the spin configurations at any  $(T, h)$  is encoded in the structure factor,  $D(\mathbf{q})$ . Let us put down a form for  $D(\mathbf{q})$  and suggest how it affects the resistivity. To simplify notation we will assume that the antiferromagnetic peak is at one wavevector  $\mathbf{Q}$ , while the ferromagnetic peak is at  $\{0, 0\}$ . The antiferromagnetic phase has an order parameter  $m_{AF}$ , say, while, for  $h > h_c(T)$ , there is induced ferromagnetic order of magnitude  $m_F$ . Assuming that the dominant *fluctuations* in the relevant part of the  $(T, h)$  phase diagram are at  $\mathbf{q} \sim \mathbf{Q}$ , we can write:  $D(\mathbf{q}) \sim m_{AF}^2 \delta(\mathbf{q} - \mathbf{Q}) + A/(1 + (\mathbf{q} - \mathbf{Q})^2 \xi^2)$  when  $h < h_c(T)$ , and  $D(\mathbf{q}) \sim m_F^2 \delta(\mathbf{q}) + A'/(1 + (\mathbf{q} - \mathbf{Q})^2 \xi^2)$  when  $h > h_c(T)$ .  $m_{AF}, m_F$  and  $\xi$  depend on  $(h, T)$ ,  $A$  depends on  $m_{AF}$  and  $\xi$  and  $A'$  on  $m_F$  and  $\xi$ . The amplitudes  $A$  and  $A'$  vanish as the corresponding  $m$  tend to saturate (since the spins get perfectly

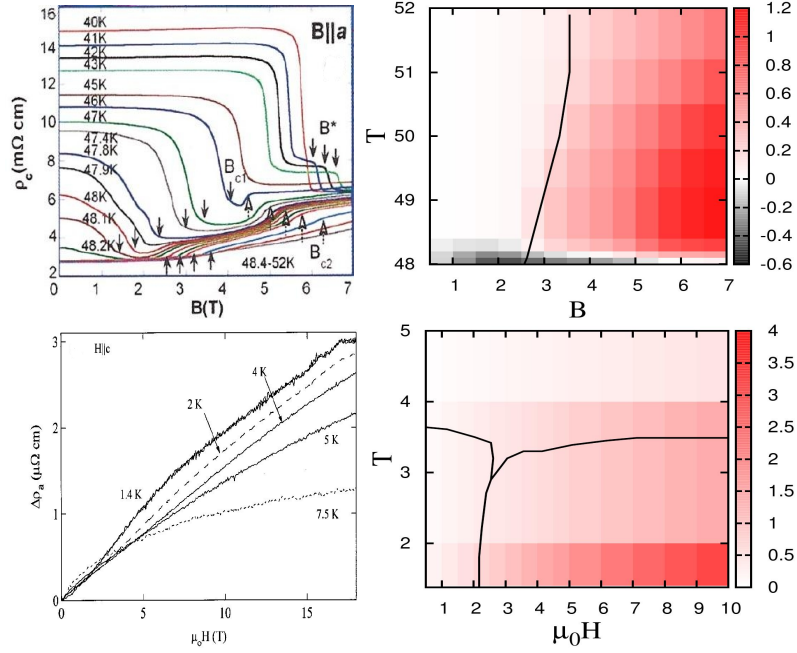


Figure 5.6: Left column : Top row shows  $\rho_c$  as a function of magnetic field for  $\text{Ca}_3\text{Ru}_2\text{O}_7$  [7]. It has antiferromagnetic metallic phase between 48K to 55K, while the bottom row shows the low temperature in-plane field-induced change in resistivity  $\Delta\rho=\rho(H)-\rho(0)$  ( $H \parallel c$ ) for antiferromagnetic metal  $\text{CeRhIn}_5$  with  $T_N=3.8\text{K}$  [11]. Right column : Plots magnetoresistance in the antiferromagnetic metallic phase for ruthenate (top panel) and heavy-fermions (bottom panel). Respective antiferromagnetic transition curve is also shown.

ordered). The delta functions in  $D(\mathbf{q})$  dictate the bandstructure while electron scattering is controlled by the Lorentzian part.

Consider three cases (a)  $T = T_c^+$ ,  $h = 0$ , (b)  $T = T_c^-$ ,  $h = 0$ , and (c)  $T = T_c^-$ ,  $h > h_c(T)$ . In (a) there is no order, so  $A$  is large, and  $\rho = \rho_a$ , say. For (b) even if  $\xi$  were the same as in (a), the presence of a large order parameter would suppress  $A$  and hence the scattering. We call this  $\rho = \rho_b \ll \rho_a$  (assuming there is indeed a large order parameter and no significant background resistivity due to impurities). If we apply a field such that  $m_{AF} \rightarrow 0$  but  $m_F$  is *still small*, then the structure factor crudely mimics the paramagnetic case, and we should have  $\rho_c \approx \rho_a$ . If all this is true, then just beyond field suppression of

antiferromagnetic order (and for  $T$  just below  $T_c$ ) we should get  $\rho_c/\rho_b \gg 1$ . Broadly, if the appearance of antiferromagnetic order with reducing  $T$  leads to a sharp drop in  $\rho$  then the field induced resistivity ratio can be large. This is independent of dimensionality and microscopic detail. A caution: as  $T \rightarrow 0$ , the applied field would drive a first order transition from a large  $m_{AF}$  state to one with large  $m_F$  and weak scattering. The scenario above will not work, as our Figure 5.2 illustrated.

## 5.5 Conclusion

We have studied the magnetoresistance in an antiferromagnetic metal motivated by the prediction of such a phase in the double perovskites. Beyond the modest field needed for suppression of long range antiferromagnetic order, the system shows almost tenfold increase in resistivity near  $T_c$ . The effect originates from strong antiferromagnetic fluctuations in the field induced ferromagnetic background. The large positive magnetoresistance, though suppressed gradually, survives the presence of significant antisite disorder. The principle that we uncover behind this “colossal positive magnetoresistance” should be applicable to other local moment based antiferromagnetic metals as well.

# Bibliography

- [1] R. von Helmolt, J. Wecker, B. Holzapfel, L. Schultz, and K. Samwer, *Phys. Rev. Lett.* **71**, 2331 (1993).
- [2] Y. Shimakawa, Y. Kubo, and T. Manako, *Nature (London)* **379**, 53 (1996).
- [3] G. Petrich, S. von Molnár, and T. Penney, *Phys. Rev. Lett.* **26**, 885 (1971).
- [4] For reviews, see D. D. Sarma, *Current Op. Solid State Mat. Sci.* **5**, 261 (2001); D. Serrate, J. M. de Teresa, and M. R. Ibarra, *J. Phys. Cond. Matt.* **19**, 023201 (2007).
- [5] T. Akimoto, Y. Maruyama, Y. Moritomo, A. Nakamura, K. Hirota, K. Ohoyama, and M. Ohashi, *Phys. Rev. B* **57**, R5594 (1998).
- [6] A. C. Komarek, S. V. Streltsov, M. Isobe, T. Möller, M. Hoelzel, A. Senyshyn, D. Trots, M. T. Fernández-Díaz, T. Hansen, H. Gotou, T. Yagi, Y. Ueda, V. I. Anisimov, M. Grüninger, D. I. Khomskii, and M. Braden, *Phys. Rev. Lett.* **101**, 167204 (2008).
- [7] X. N. Lin, Z. X. Zhou, V. Durairaj, P. Schlottmann, and G. Cao, *Phys. Rev. Lett.* **95**, 017203 (2005).
- [8] S. McCall, G. Cao, and J. E. Crow, *Phys. Rev. B* **67**, 094427 (2003).
- [9] G. Cao, K. Abboud, S. McCall, J. E. Crow, and R. P. Guertin, *Phys. Rev. B* **62**, 998 (2000).
- [10] Y. Yoshida, S.-I. Ikeda, H. Matsuhata, N. Shirakawa, C. H. Lee, and S. Katano, *Phys. Rev. B* **72**, 054412 (2005).

- [11] A. D. Christianson, A. H. Lacerda, M. F. Hundley, P. G. Pagliuso, and J. L. Sarrao, *Phys. Rev. B* **66**, 054410 (2002).
- [12] T. Takeuchi, T. Inoue, K. Sugiyama, D. Aoki, Y. Tokiwa, Y. Haga, K. Kindo, and Y. Ōnuki, *J. Phys. Soc. Jpn.* **70**, 877 (2001).
- [13] E. Dagotto, *Science* **309**, 257 (2005).
- [14] P. Sanyal and P. Majumdar, *Phys. Rev. B* **80**, 054411 (2009).
- [15] P. Sanyal, H. Das, and T. Saha-Dasgupta, *Phys. Rev. B* **80**, 224412 (2009).
- [16] R. Tiwari and P. Majumdar, arXiv:**1105.0148** (2011).
- [17] D. Sánchez, J. A. Alonso, M. García-Hernandez, M. J. Martínez-Lopez, M. T. Casais, and J. L. Martínez, *J. Mater. Chem.* **13**, 1771 (2003).
- [18] S. Jana, C. Meneghini, P. Sanyal, S. Sarkar, T. Saha-Dasgupta, O. Karis, and S. Ray, arXiv:**1204.3378** (2012).
- [19] V. N. Singh and P. Majumdar, *Eur. Phys. J. B* **83**, 147 (2011).
- [20] V. N. Singh and P. Majumdar, arXiv:**1107.0782** (2011).
- [21] I. Balberg and J. S. Helman, *Phys. Rev. B* **18**, 303 (1978).

# Chapter 6

## Magnon Spectrum in the Domain Ferromagnetic State

**Chapter summary:** This chapter describes our results on magnons in the antisite disordered ferromagnets. We have used an effective Heisenberg model with parameters that match the magnetisation in the parent electronic problem. Using a spin rotation technique and the Holstein-Primakoff transformation we compute the magnon lineshape within a  $1/S$  expansion. For the mixed ferro-antiferro system this involves a boson problem that can be solved via a Bogolyubov transformation. We provide a description of the spin wave excitations for progressively higher degree of antisite disorder. Results on the magnon energy and broadening reveal that even at large disorder, existence of domain like structure ensures that the response has a strong similarity to the clean case. We suggest a rough scheme for inferring the domain size from the spin wave damping. We also highlight how the common assumption about random antisites leads to a gross overestimate of magnon damping.

### 6.1 Introduction

Double perovskite (DP) materials with general formula  $A_2BB'O_6$  have generated a great deal of interest [1] both in terms of their basic physics as well as the possibility of technological applications. In particular,  $Sr_2FeMoO_6$  (SFMO) shows high ferromagnetic  $T_c \sim 420K$ , large electron spin polarisation (half-metallicity), and significant low field magnetoresistance [2, 3].

The ferromagnetic coupling between the  $S = \frac{5}{2}$  localized magnetic moments in  $\text{Sr}_2\text{FeMoO}_6$  ( $\text{Fe}^{3+}$  ion,  $3d^5$  state) is driven by a double exchange mechanism, where electrons from Mo delocalise over the Mo-O-Fe network. The B (Fe) ions order ferromagnetically while the conduction electrons that mediate the exchange are aligned opposite to the Fe moments, leading to a saturation magnetisation of  $4\mu_B$  per formula unit in ordered SFMO. The large entropy gain from disordering promote *antisite disorder* (ASD) whereby some B ions occupy the positions of B' ions and *vice versa*.

There is clear evidence now that B-B' mislocations are not random but spatially correlated [4, 5]. While antisite disorder (ASD) suppresses long range structural order, electron microscopy [4] and x-ray absorption fine structure (XAFS) [5] reveal that a high degree of short range order survives. The structural disorder has a direct magnetic impact. If two Fe ions adjoin each other the filled shell  $d^5$  configuration leads to antiferromagnetic (AFM) superexchange between them. The result is a pattern of structural domains, with each domain internally ferromagnetic (FM) while adjoining domains are antiferromagnetic with respect to each other.

Domain structure has been inferred in the low doping manganites as well, due to competing ferromagnetic and antiferromagnetic interactions. Inelastic neutron scattering in those materials suggest the presence of ferromagnetic domains in an antiferromagnetic matrix, and allows an estimate of the domain size [6, 7]. In this chapter we provide a similar framework for interpreting the magnetic state and domain structure in the double perovskite from spin wave data.

Our main results are the following [8].

1. We compute the dynamical magnetic structure factor within a  $\frac{1}{5}$  expansion of an effective Heisenberg model chosen to fit the electronic model results.
2. The magnon data is reminiscent of the *clean limit* even at maximum ASD (50%), where the bulk magnetisation vanishes due to interdomain cancellation.
3. We suggest a rough method for inferring the domain size from the magnon data and check its consistency with the ASD configurations used.

4. We demonstrate that *uncorrelated* ASD leads to a much greater scattering of magnons, *i.e.*, a much broader lineshape. This suggests that in addition to XAFS and microscopy, neutron scattering would be a sensitive probe of the nature of disorder in these materials.

## 6.2 Effective magnetic model

### 6.2.1 Structural motif

We quickly recapitulate the structural aspect of the problem, discussed in detail earlier, before moving to the magnetism.

Given the similar location of the B and B' ions (at the center of the octahedra) the tendency towards defect formation is more pronounced in the double perovskites. This tendency of mislocation interplays with the inherent B-B' ordering tendency and creates a spatially correlated pattern of antisites [4, 5] rather than random mislocation. To model this situation we have used a simple *lattice-gas model* [9]. On proper annealing it will go to a long range ordered B, B', B, B'... pattern. We frustrate this by using a short annealing time to mimic the situation in the real materials. We encode the atomic positions by defining a binary variable  $\eta_i$ , such that  $\eta_i = 1$  when a site has a B ion, and 0 when it has a B' ion. Thus for an ordered case we will get  $\eta$ 's as 1, 0, 1, 0, 1, 0... along each cubic axes.

The B-B' patterns that emerge on short annealing are characterised by the structural order parameter  $S = 1 - 2x$ , where  $x$  is the fraction of B (or B') atoms that are on the wrong sublattice. We have chosen four disordered families with increasing disorder for our study. Each member of the disorder family is being generated at a given annealing temperature for a fixed annealing time, starting with different initial random B-B' configurations. The amount of disorder in different member of the disorder family generated this way does not remains exactly same, it has some deviation from the average value for that family. This is the reason for the difference in the value of the structural order parameter  $S$  shown in the chapter (mentioned below), from other chapters. One structural motif each for these families is shown in the first column of Figure 6.1 , with progressively increasing disorder (from top to bottom) on a  $40 \times 40$  lattice. We have plotted

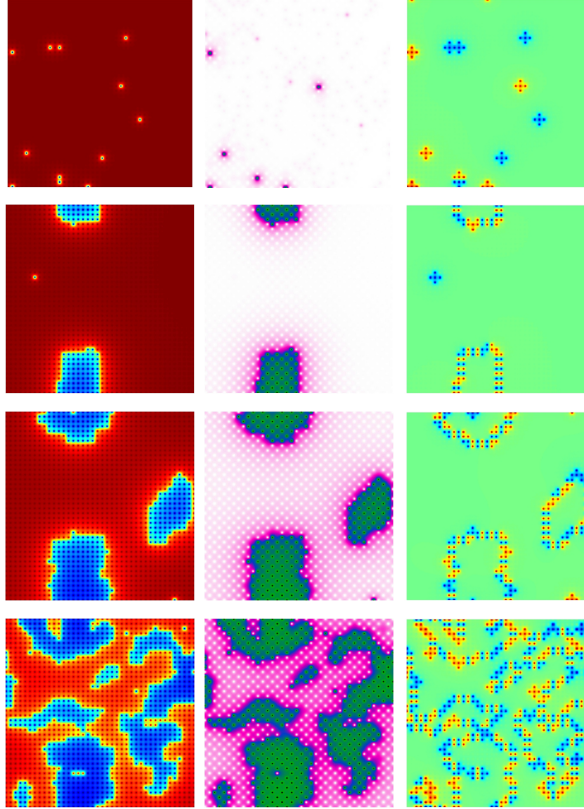


Figure 6.1: First column contains the structural motif for four disordered families with progressively increasing disorder (from top to bottom). Second column shows the ground state spin overlap. In the third column, we have shown the corresponding nearest neighbor (NN) bond configurations. Here red, blue, and green represents B-B, B'-B', and B-B' bonds respectively. Lattice size is  $40 \times 40$  [10].

$g(\mathbf{r}_i) = (\eta_i - \frac{1}{2})e^{i\pi(x_i + y_i)}$  as an indicator of structural order. For a perfectly ordered structure  $g(\mathbf{r}_i)$  is constant. We have denoted these different realisations of antisite disorder configurations as C1, C2, C3, C4 and the corresponding structural order parameter has values  $S = 0.98, 0.88, 0.59, 0.17$  from top to bottom. We solve the electronic-magnetic problem on these structural motifs.

## 6.2.2 Electronic Hamiltonian

To study the magnetic order we have used the Hamiltonian that has the usual couplings of the ordered double perovskites, and an additional antiferromagnetic coupling when two magnetic B ions are nearest neighbor. The Hamiltonian for the microscopic model is:

$$H = H_{loc}\{\eta\} + H_{kin}\{\eta\} + H_{mag}\{\eta\} \quad (6.1)$$

Where

$$\begin{aligned} H_{loc}\{\eta\} &= \epsilon_B \sum_{i,\sigma} \eta_i f_{i\sigma}^\dagger f_{i\sigma} + \epsilon_{B'} \sum_{i,\sigma} (1 - \eta_i) m_{i\sigma}^\dagger m_{i\sigma} \\ H_{kin}\{\eta\} &= -t_1 \sum_{\langle ij \rangle, \sigma} \eta_i \eta_j f_{i\sigma}^\dagger f_{j\sigma} - t_2 \sum_{\langle ij \rangle, \sigma} (1 - \eta_i)(1 - \eta_j) m_{i\sigma}^\dagger m_{j\sigma} \\ &\quad - t_3 \sum_{\langle ij \rangle, \sigma} (\eta_i + \eta_j - 2\eta_i \eta_j) (f_{i\sigma}^\dagger m_{j\sigma} + h.c.) \\ H_{mag}\{\eta\} &= J \sum_{i,\alpha\beta} \eta_i \mathbf{S}_i \cdot f_{i\alpha}^\dagger \vec{\sigma}_{\alpha\beta} f_{i\beta} + \tilde{J}_{AF} \sum_{\langle ij \rangle} \eta_i \eta_j \mathbf{S}_i \cdot \mathbf{S}_j \end{aligned}$$

Here,  $H_{loc}\{\eta\}$  is the onsite term with  $\epsilon_B$  and  $\epsilon_{B'}$  as level energies, respectively, at the B and B' sites.  $f$  is the electron operator referring to the magnetic B site and  $m$  is that of the non-magnetic B' site. Whereas  $H_{kin}$  represents the NN hopping term. For simplicity we set all the NN hopping amplitudes to be same  $t_1=t_2=t_3 = t$ . The magnetic interaction term  $H_{mag}\{\eta\}$  consists of the Hund's coupling  $J$  on the B sites, and the antiferromagnetic superexchange coupling  $\tilde{J}_{AF}$  between two NN magnetic B sites. Here  $\mathbf{S}_i$  is the classical core spin on the B site at  $\mathbf{r}_i$  with  $|\mathbf{S}_i| = 1$ . We take  $J/t \gg 1$  with  $J > 0$ , and  $\tilde{J}_{AF}|\mathbf{S}|^2/t = 0.08$ , based on the  $T_N$  scale in SrFeO<sub>3</sub>. We have ignored orbital degeneracy, Coulomb effects, *etc.*, to focus on the essential magnetic model on the disordered structure. We have used a two dimensional model because it already captures the qualitative physics while allowing ease of visualisation and access large system sizes. The formulation readily carries over to three dimensions as well.

We have used a real space exact diagonalisation based Monte Carlo method involving a travelling cluster approximation [11] to anneal the spin-fermion system towards its ground state in the disordered background [10].

Annealing the electron-spin system down to low temperature on a given structural motif leads to the magnetic ground states shown in the middle column of

Figure 6.1 . We plot the spin overlap factor,  $h_i = \mathbf{S}_0 \cdot \mathbf{S}_i$ , where  $\mathbf{S}_0$  is the left-lower-corner spin in the lattice. The comparison of the first and second columns in Figure 6.1 indicate that the structural and magnetic domains coincide with each other. The third column of Figure 6.1 shows the NN structural partners. We have three possibilities: B-B, B'-B' and B-B', represented by colours red, blue and green respectively in the plot.

### 6.2.3 Effective Heisenberg Hamiltonian

Given the difficulty in doing a spin-wave analysis on the full Hamiltonian (Eq. 6.1), we use an *effective* Heisenberg model

$$H_{eff} = \sum_{\{ij\}} J_{ij} \mathbf{S}_i \cdot \mathbf{S}_j \quad (6.2)$$

where  $\{ \}$  represents the set of NN and next nearest neighbor (NNN) sites.  $J_{ij}$  is the effective coupling (FM/AFM) between the local moments at  $\mathbf{r}_i$  and  $\mathbf{r}_j$  sites. In our two dimensional antisite disordered configurations  $J_F$  operates between two local moments when they are at the NNN position, and  $J_{AF}$  is active when the moments are at the NN position (a B-O-B arrangement). We have estimated the effective coupling  $J_F$  and  $J_{AF}$  as follows.

For getting the ferromagnetic coupling ( $J_F$ ) we have considered the ordered double perovskite structure. We calculated the order parameter, *i.e.*, the magnetic structure factor  $S(\mathbf{k})$  at  $\mathbf{k} = (0, 0)$ , as a function of temperature for the full electronic Hamiltonian (Eq. 6.1) using Monte Carlo simulation. We then repeated the same procedure for the NNN ferromagnetic Heisenberg Hamiltonian, defined on only the magnetic sites of the double perovskite. We found that for  $J_F/t = -0.04$ , the two results match very well.

In order to get the antiferromagnetic coupling we considered the ordered perovskite where both the B and B' site carry a magnetic moment (mimicking SrFeO<sub>3</sub>), and computed its antiferromagnetic structure factor peak  $\mathbf{k}=(\pi, \pi)$ . This model involves both electronic kinetic energy and Fe-Fe superexchange. We find that the result can be modeled via a Heisenberg model with  $J_{AF}/t = 0.065$ .

Using the couplings inferred from these limiting cases,  $J_F/t = -0.04$  and  $J_{AF}/t = 0.065$ , we studied the bond disordered Heisenberg model for the antisite

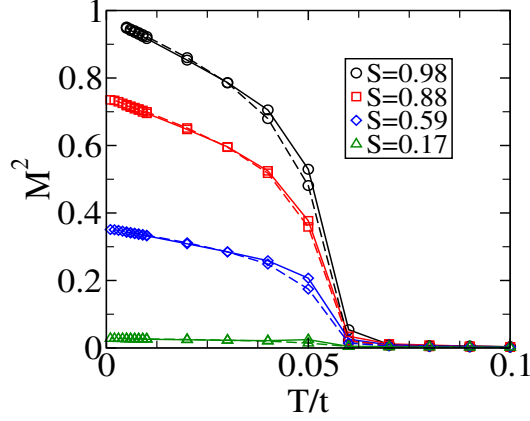


Figure 6.2: Comparison between the evolution of the spin structure factor  $S(\mathbf{k})$  at  $\mathbf{k} = (0,0)$  with temperature for the spin configurations of various disorder families (from top to bottom) C1, C2, C3 and C4 obtained from the full electronic Hamiltonian with  $\tilde{J}_{AF}S^2/t = 0.08$  and the effective Heisenberg model with  $J_F/t = -0.04$  and  $J_{AF}/t = 0.065$ . Lattice size is  $40 \times 40$ .

disordered double perovskite magnet. We compared the ferromagnetic structure factor peak  $S(\mathbf{k})$  at  $\mathbf{k}=(0,0)$  obtained from the disordered Heisenberg model with that from the full electronic Hamiltonian (Eq. 6.1). The Heisenberg result for the ferromagnetic structure factor  $S(0,0)$  as a function of temperature matches very well, Figure 6.2, with the electronic Hamiltonian result for all antisite disordered configurations. This gives us confidence in the usefulness of the Heisenberg model for spin dynamics.

## 6.3 Spin dynamics

### 6.3.1 Spin-wave excitation

We have used the spin rotation technique [12] to evaluate the spin-wave modes and dynamic structure factor at zero temperature. The effective Heisenberg model (Eq. 6.2) can be cast in a form useful for spin wave analysis by defining a *local frame* at each site so that the spins point along the  $+z$  direction in the ground

state. We can use  $\bar{\mathbf{S}}_i = U_i \mathbf{S}_i$ , where  $\bar{\mathbf{S}}_i$  points along its local  $z$ -axis in the classical limit. The unitary rotation matrix  $U_i$  for site  $\mathbf{r}_i$  is given by

$$U_i = \begin{vmatrix} \cos(\theta_i) \cos(\psi_i) & \cos(\theta_i) \sin(\psi_i) & -\sin(\theta_i) \\ -\sin(\psi_i) & \cos(\psi_i) & 0 \\ \sin(\theta_i) \cos(\psi_i) & \sin(\theta_i) \sin(\psi_i) & \cos(\theta_i) \end{vmatrix} \quad (6.3)$$

where  $\theta$ s and  $\psi$ s are the Euler rotation angles. Now one can write the generalized Hamiltonian

$$H_{eff} = \sum_{\{ij\}} J_{ij} \bar{\mathbf{S}}_i \cdot F_{ij} \bar{\mathbf{S}}_j \quad (6.4)$$

where  $F_{ij} = U_i U_j^{-1}$  is the overall rotation from one reference frame to another and its elements  $F_{ij}^{\alpha\beta}$  can be obtained from Eq. (6.3).

Applying the approximate Holstein-Primakoff (HP) transformation in the large  $S$  limit the spin operators in the local reference frame become:  $\bar{S}_i^+ = \sqrt{2S} b_i$ ,  $\bar{S}_i^- = \sqrt{2S} b_i^\dagger$  and  $\bar{S}_i^z = S - b_i^\dagger b_i$ , where  $b_i$  and  $b_i^\dagger$  are the boson (magnon) annihilation and creation operators respectively. Retaining only the quadratic terms in  $b$  and  $b^\dagger$ , which describe the dynamics of the non-interacting magnons and neglecting magnon interaction terms of order  $(\frac{1}{S})$ , the generalized Hamiltonian (Eq. 6.4) reduces to

$$\mathcal{H} = \sum_{\{ij\}} [\mathcal{J}_{ij} (G_{ij}^1 b_i^\dagger b_j + G_{ij}^2 b_i b_j + h.c.) + f_{ij} (b_i^\dagger b_i + b_j^\dagger b_j)] \quad (6.5)$$

where  $\mathcal{J}_{ij} = S J_{ij} / 2$ ,  $f_{ij} = -S J_{ij} F_{ij}^{zz}$  and the rotation coefficients  $G^1 = (F_{ij}^{xx} \pm F_{ij}^{yy}) - i(F_{ij}^{xy} \mp F_{ij}^{yx})$ . The Hamiltonian (6.5) is diagonalized by the Bogolyubov transformation

$$b_i = \sum_n (u_n^i c_n + v_n^{i*} c_n^\dagger) \quad (6.6)$$

where  $c^\dagger$  and  $c$  are the quasiparticle operators.  $u$  and  $v$ , which satisfy  $\sum_n (u_n^i u_n^{j*} - v_n^{i*} v_n^j) = \delta_{ij}$  ensuring the bosonic character of the quasiparticles are obtained from

$$\begin{pmatrix} A_{ij} & B_{ij}^* \\ B_{ij} & A_{ij}^* \end{pmatrix} \begin{pmatrix} u_n^j \\ v_n^j \end{pmatrix} = \omega_n \begin{pmatrix} \delta_{ij} & 0 \\ 0 & -\delta_{ij} \end{pmatrix} \begin{pmatrix} u_n^j \\ v_n^j \end{pmatrix} \quad (6.7)$$

where  $A_{ij} = 2\mathcal{J}_{ij} (G_{ij}^1 + G_{ji}^{1*}) + \epsilon_i \delta_{ij}$ ,  $B_{ij} = 2\mathcal{J}_{ij} (G_{ij}^2 + G_{ji}^2)$ , and  $\epsilon_i = 2 \sum_j (f_{ij} + f_{ji})$ . Now the spin-spin correlation function can be evaluated using the magnon energies and wavefunctions obtained from Eq. (6.7), where the excitation eigenvalues  $\omega_n \geq 0$ .

### 6.3.2 Dynamical structure factor

A neutron scattering experiment measures the spin-spin correlation function in momentum and frequency space  $S(\mathbf{k}, \omega)$  to describe the spin dynamics of the magnetic systems on an atomic scale. From  $\mathbf{S}_i = U_i^{-1} \bar{\mathbf{S}}_i$  one can express  $S_i^\alpha = \sum_\mu U_i^{\mu\alpha*} \bar{S}_i^\mu$  where  $\alpha$  and  $\mu$  represents the  $x$ ,  $y$ , and  $z$  components. Now applying the approximate HP transformation to the rotated spins one can write

$$S_i^\beta = p_i^\beta b_i + q_i^\beta b_i^\dagger + r_i^\beta (S - b_i^\dagger b_i) \quad (6.8)$$

where  $\beta = +, -, \text{ and } z$ . And  $p, q$ , and  $r$  are the rotation coefficients.

$$\begin{aligned} p_i^\pm &= \sqrt{\frac{S}{2}} (U_i^{xx} \pm U_i^{yy}) - i(U_i^{yx} \mp U_i^{xy}) \\ q_i^\pm &= \sqrt{\frac{S}{2}} (U_i^{xx} \mp U_i^{yy}) + i(U_i^{yx} \pm U_i^{xy}) \\ r_i^\pm &= U_i^{zx} \pm iU_i^{zy} \\ p_i^z &= U_i^{xz} - iU_i^{yz} \\ q_i^z &= U_i^{xz} + iU_i^{yz} \\ r_i^z &= U_i^{zz} \end{aligned}$$

Putting Eq. (6.6) in (6.8) the space time spin-spin correlation function can be written as

$$S_i^\alpha(t) S_j^\beta(0) = \sum_{mn} [A_{ij}^{\alpha\beta} c_m^\dagger(t) c_n(0) + B_{ij}^{\alpha\beta} c_m(t) c_n^\dagger(0)] \quad (6.9)$$

where A and B are structure factor coefficients.

$$\begin{aligned} A_{ij}^{\alpha\beta} &= q_i^\alpha p_j^\beta u_i^{m*} u_j^n + p_i^\alpha q_j^\beta v_i^{m*} v_j^n + p_i^\alpha p_j^\beta v_i^{m*} u_j^n \\ &\quad + q_i^\alpha q_j^\beta u_i^{m*} v_j^n - S \times r_i^\alpha r_j^\beta (u_i^{m*} u_i^n + u_j^{m*} u_j^n) \\ B_{ij}^{\alpha\beta} &= q_i^\alpha p_j^\beta v_i^m v_j^{n*} + p_i^\alpha q_j^\beta u_i^m u_j^{n*} + p_i^\alpha p_j^\beta u_i^m v_j^{n*} \\ &\quad + q_i^\alpha q_j^\beta v_i^m u_j^{n*} - S \times r_i^\alpha r_j^\beta (v_i^m v_i^{n*} + v_j^m v_j^{n*}) \end{aligned}$$

In the Fourier and frequency space

$$S^{\alpha,\beta}(\mathbf{k}, \omega) = \frac{1}{N} \int dt e^{i\omega t} \sum_{ij} e^{i\mathbf{k} \cdot (\mathbf{r}_i - \mathbf{r}_j)} \langle S_i^\alpha(t) S_j^\beta(0) \rangle \quad (6.10)$$

and the total spin-spin correlation function

$$\begin{aligned} S(\mathbf{k}, \omega) &= \frac{1}{2} [S^{+,-}(\mathbf{k}, \omega) + S^{-,+}(\mathbf{k}, \omega)] + S^{z,z}(\mathbf{k}, \omega) \\ &= \sum_l W_{\mathbf{k}}^l \delta(\omega - \omega_l) \end{aligned}$$

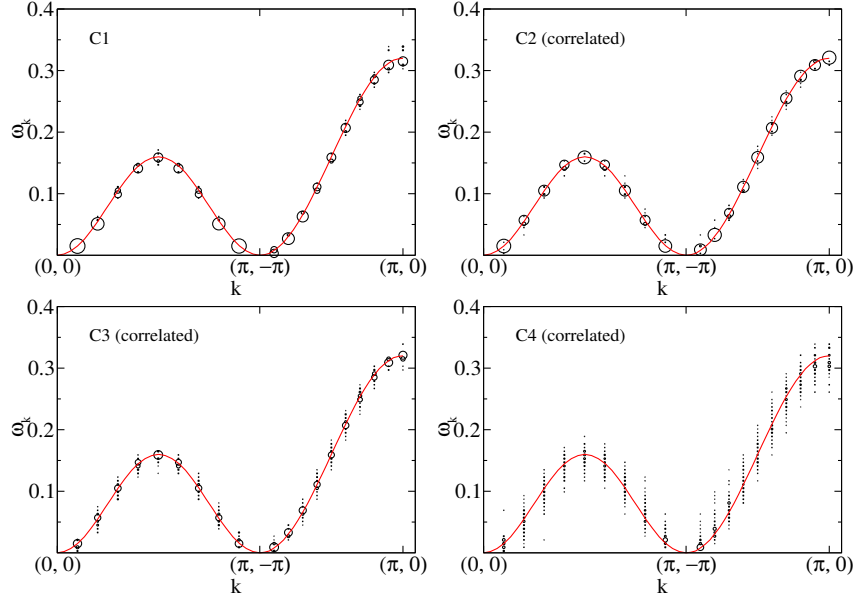


Figure 6.3: Spin-wave spectrum along main symmetry directions of the Brillouin zone for spin configurations C1, C2, C3, and C4 ( $x = 0.01, 0.11, 0.21$  and  $0.41$  respectively, shown in Figure 6.1 ). With increasing antiseite disorder from C1 to C4 the spectrum becomes broader for a fixed value of momentum  $\mathbf{k}$ . Here  $J_F = -0.04$ ,  $J_{AF} = 0.065$ , and lattice size is  $40 \times 40$ .

where the coefficient of the delta function

$$W_{\mathbf{k}}^l = \frac{1}{N} \sum_{ij} \mathcal{B}_{ij}^l e^{i\mathbf{k} \cdot (\mathbf{r}_i - \mathbf{r}_j)} \quad (6.11)$$

is the spin-wave weight with  $\mathcal{B}_{ij}^l = \frac{1}{2}(B_{ij}^{+-} + B_{ij}^{-+}) + B_{ij}^{zz}$ . Here  $W_{\mathbf{k}}^l$  is observed as the intensity of magnon spectrum in the neutron scattering experiment.

## 6.4 Results and discussion

We start by presenting the results for magnons in the configurations C1-C4 (Figure 6.1), and then move to an analysis of the linewidth, the estimation of domain size, and the contrast with the uncorrelated disorder.

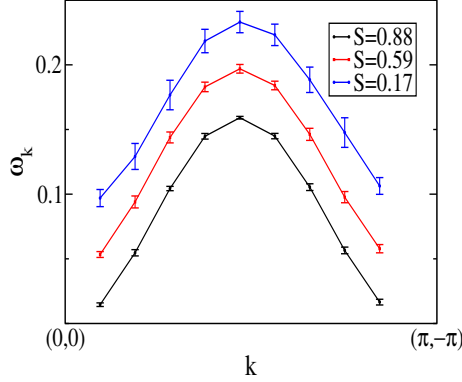


Figure 6.4: Mean spin wave energy  $\bar{\omega}_{\mathbf{k}}$  (dots) and spin-wave width  $\Delta\omega_{\mathbf{k}}$  (bars), defined in the text, for the correlated antisite configurations C2-C4. The curves are vertically shifted for clarity.

### 6.4.1 Antiferromagnetically coupled domains

Figure 6.3 shows the magnon spectra of C1-C4 obtained from the Heisenberg model with the FM and AFM couplings discussed earlier. In a model with only ferromagnetic couplings, *i.e.*, no disorder, we would have obtained only the red curve,  $\omega_{\mathbf{k}}^0$ , for propagating magnons. The striking feature in all these panels is how closely the mean energy of the magnons follow  $\omega_{\mathbf{k}}^0$  despite the large degree of mislocation in C2 and C3, and maximal disorder ( $x \sim 0.5$ ) in C4 (refer to the spatial plots in Figure 6.1). The broadening, although noticeable in C4, does not obscure the basic dispersion.

Figure 6.4 quantifies the mean energy and broadening by computing :

$$\bar{\omega}_{\mathbf{k}} = \int S(\mathbf{k}, \omega) \omega d\omega$$

$$[\Delta\omega_{\mathbf{k}}]^2 = \left[ \int S(\mathbf{k}, \omega) \omega^2 d\omega \right] - \bar{\omega}_{\mathbf{k}}^2$$

We have shown these two quantities for the C2-C4 structures in Figure 6.4 . The  $\bar{\omega}_{\mathbf{k}}$  have been vertically shifted for clarity and the  $\Delta\omega_{\mathbf{k}}$  are superposed as *error bars* on these. It is clear that even in the most disordered sample (C4), where the mislocation  $x \sim 0.4$ , the broadening is only a small fraction of the magnon energy. This will be an indicator when we discuss spin waves in an uncorrelated disorder background.

## 6.4.2 Broadening: impact of domain size

There are two ingredients responsible for the spectrum that one observes in the Figure 6.3 :

1. the domain structure,
2. the antiferromagnetic coupling across the domains.

To deconvolve these effects and have a strategy for inferring domain size from neutron data, we studied a situation where we set  $J_{AF} = 0$  in the Heisenberg model defined on the structures C1-C4. In that case we will have *decoupled ferromagnetic domains* without any requirement of antiparallel spin orientation between them. We think this is an interesting scheme to explore since the antiferro bonds are limited to the domain boundaries and *are not* equal to the number of mislocated sites.

Figure 6.5 shows the overall magnon spectrum for this case, using the same convention as in Figure 6.3 , while Figure 6.6 quantifies the mean energy and broadening in this *decoupled domain* case. The absence of  $J_{AF}$  does not seem to make a significant difference to the spectrum as a comparison of Figure 6.4 and 6.6 reveal. This correspondence, valid even in C4, suggests the following :

- most of the spectral features arise from the domain structure, and the associated confinement of spin waves, rather than the antiferro coupling,
- we can proceed with a much simpler modeling of the spectrum without invoking the complicated Bogolyubov-de Gennes formulation that antiferromagnetic coupling requires.

Essentially, much can be learnt from *tight binding* models defined on appropriate structures, as happens for ferromagnetic states, without having to invoke the *pairing* terms that arise from antiferro coupling. A modeling of the full dispersion will require the antiferro terms as well, but the inference about presence of domains, and an estimate of their size, need not. We proceed with this next.

To proceed with estimating the typical domain size we need a few assumptions:

1. The total degree of mislocation,  $x$ , should be known, based on the bulk magnetisation measurement.

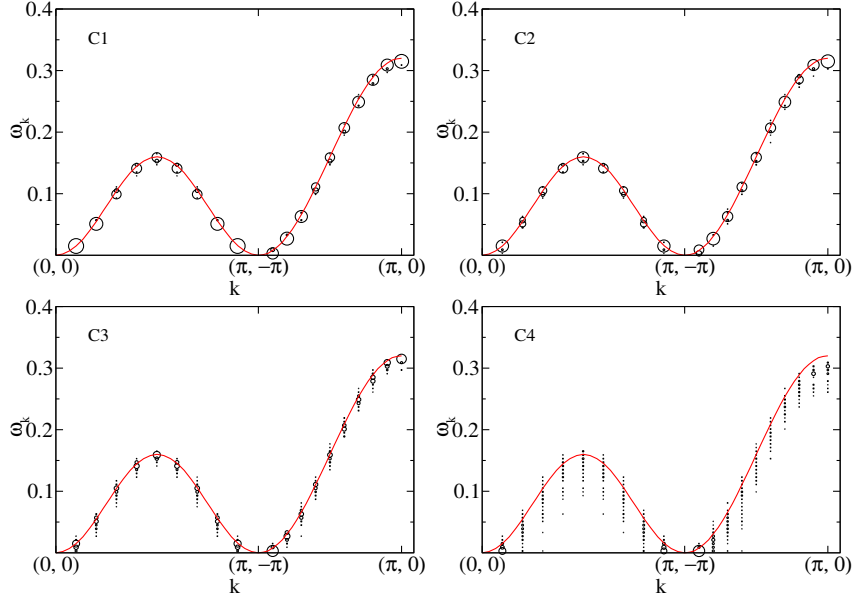


Figure 6.5: Spin-wave spectra along main symmetry directions of the Brillouin zone for spin configurations C1-C4 (Figure 6.1 ) with  $x = 0.01, 0.11, 0.21$  and  $0.41$  respectively. Increasing fractional weakly coupled domain boundary spins from C1 to C4 enhances the spin-wave softening near the zone boundary along  $[\pi, 0]$  and the spectrum also becomes broader for a given  $\mathbf{k}$ . Here  $J_F = -0.04$ ,  $J_{AF} = 0$ , and lattice size is  $40 \times 40$ .

2. If the overall system size is  $L \times L$  (or equivalent in a 3D model), the number of mislocated sites would be  $xL^2$ .
3. If the domain size is  $L_d$  then the number of domains within the  $L \times L$  area is  $N_d \sim xL^2/L_d^2$ . In reality domains need not have one single size, as C2-C4 indicate, but we need the assumption to make some headway.
4. We need to locate these  $N_d$  domains randomly, in a non overlapping manner, within the  $L \times L$  system, and average the spectrum obtained over different realisations of domain location.

This scheme, carried out for various  $L_d$ , can be compared to the full  $S(\mathbf{k}, \omega)$  data to get a feel for the appropriate  $L_d$ . We show the result below for such a tight binding exploration for the C2 configuration, modeled in terms of different

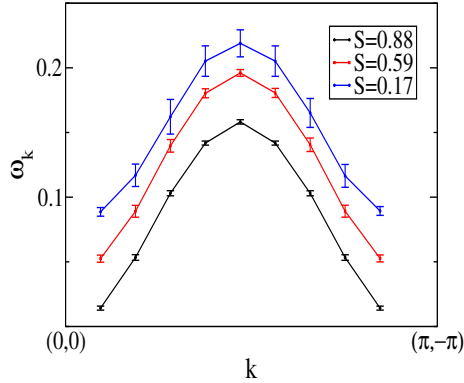


Figure 6.6: Mean spin wave energy  $\bar{\omega}_{\mathbf{k}}$  (dots) and spin-wave width  $\Delta\omega_{\mathbf{k}}$  (bars) for C2-C4 now with  $J_{AF} = 0$ , *i.e.*, decoupled domains. The curves are vertically shifted for clarity.

domain distributions that respect the same overall mislocation.

When we compare the ratio of mean broadening to bandwidth obtained at different values of  $L_d$  (and so  $N_d$ ) with that for the real data, Figure 6.4, it turns out that  $L_d = 10$  provides a best estimate. It also reasonably describes the broadening at stronger disorder, C3 and C4, where of course  $N_d$  is larger. An analytic feel for these results can be obtained by considering the modes of a square size  $L_d \times L_d$  under open boundary conditions.

### 6.4.3 Contrast with uncorrelated antisites

In modeling the antisite disorder much of the earlier work in the field assume the defect locations to be random. We have followed the experimentally motivated path which suggests that the mislocated sites themselves form an ordered structure separated from the parent (or majority) by an antiphase boundary. The sources of scattering are the boundary between these domains rather than random point defects. Since much of double perovskites modeling has assumed the random antisite situation, it is worth exploring the differences in the magnon spectra between correlated and uncorrelated antisites.

We have already seen the results for correlated disorder for different degrees of mislocation,  $x$ . We generated *uncorrelated* antisite configurations with the same  $x$  by starting with ordered configurations and randomly exchanging B and B'

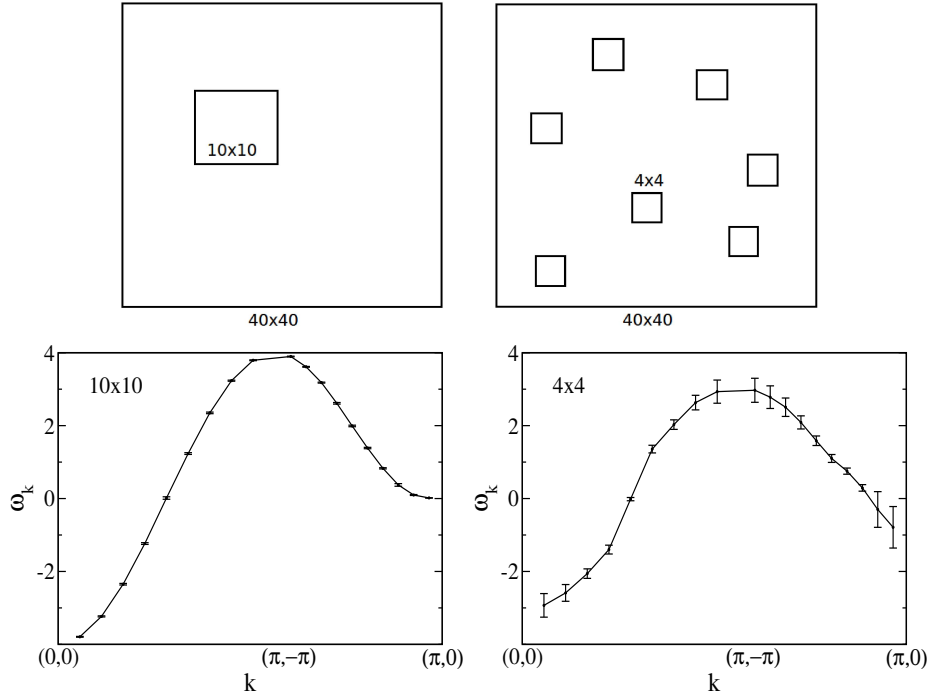


Figure 6.7: Modeling  $C_2$  in terms of a domain of size  $10 \times 10$  (left) and of seven domains of size  $4 \times 4$  (right). The corresponding mean energy and broadening are shown below.

till the desired degree of disorder is reached. These configurations naturally do not have any structural domains. Annealing the full electronic Hamiltonian on these configurations, call them  $C_1(\text{random})$ ,  $C_2(\text{random})$ , ..., etc., down to low  $T$ , leads to the magnetic ground states. The ground states are disordered ferromagnets but without any domain pattern. We computed the magnon lineshape in these configurations, and, for illustration, show the results for  $C_2(\text{random})$  and  $C_3(\text{random})$  side by side with their correlated counterparts  $C_2$  and  $C_3$  as shown in the Figure 6.8.

There is a *striking increase* in the magnon line width (or  $\Delta\omega_{\mathbf{k}}$ ) in the uncorrelated case. There is almost nine fold increase in the magnon line width in  $C_2$  and six fold in  $C_3$  of the uncorrelated disorder with respect to the correlated disorder case.

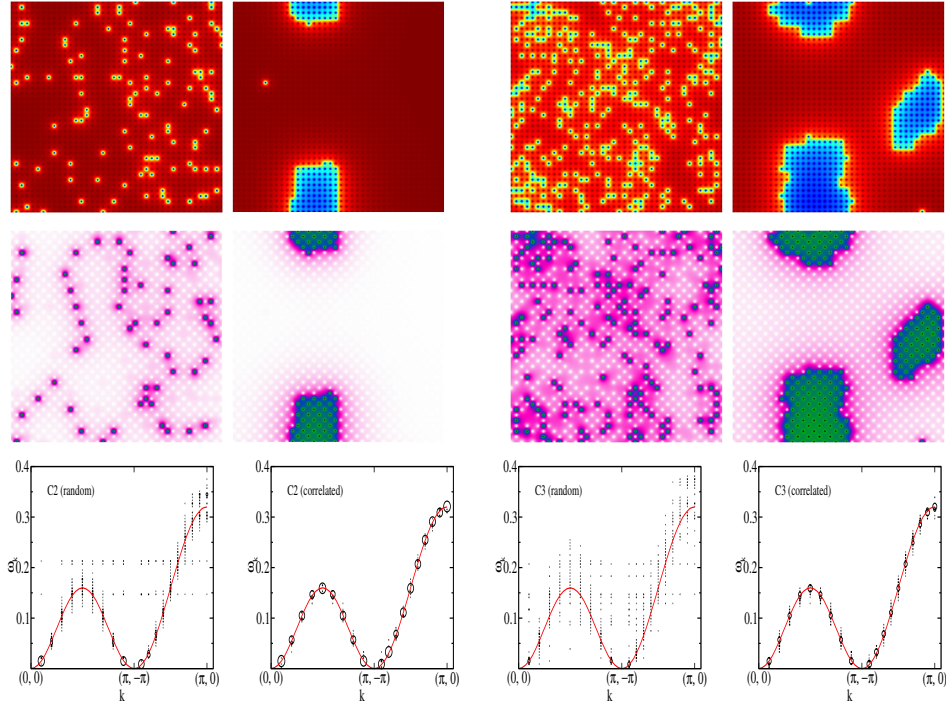


Figure 6.8: The left set of panels correspond to mislocation for  $x = 0.11$  where we compare the magnon spectrum for uncorrelated disorder (left) with correlated disorder (C2) right. The top panels refer to the structural pattern, the middle to the magnetic ground state, and the bottom to the magnon response. The right set of panels refer to  $x = 0.21$ , and the same indicators as for the left panels. Notice the remarkably broader lineshape for the uncorrelated disorder case where it is difficult to make much of a correspondence with the clean dispersion.

## 6.5 Conclusion

We have studied the dynamical magnetic structure factor of a double perovskite system taking into account the basic ferromagnetic ordering tendency and the defect induced local antiferromagnetic correlations. We used structural motifs that correspond to correlated disorder, obtained from an annealing process. The results on magnon energy and broadening reveal that even at very large disorder, the existence of domain like structure ensures that the response has a strong similarity to the clean case. We tried out a scheme for inferring the domain size

from the spin wave damping, so that experimenters can make an estimate of domains without having spatial data, and find it to be reasonably successful. We also highlight how the common assumption about random antisites, that is widely used in modeling these materials, would lead to a gross overestimate of magnon damping. In summary, dynamical neutron scattering can be a direct probe of the unusual ferromagnetic state in these materials and confirm the presence of correlated antisites.

# Bibliography

- [1] For reviews, see D. D. Sarma, *Current Op. Solid St. Mat. Sci.*, **5**, 261 (2001); D. Serrate, J. M. de Teresa, and M. R. Ibarra, *J. Phys. Cond. Matt.* **19**, 023201 (2007).
- [2] K.-I. Kobayashi, T. Kimura, H. Sawada, K. Terakura, and Y. Tokura, *Nature* **395**, 677 (1998).
- [3] Y. Tomioka, T. Okuda, Y. Okimoto, R. Kumai, K.-I. Kobayashi, and Y. Tokura, *Phys. Rev. B* **61**, 422 (2000).
- [4] T. Asaka, X. Z. Yu, Y. Tomioka, Y. Kaneko, T. Nagai, K. Kimoto, K. Ishizuka, Y. Tokura, and Y. Matsui, *Phys Rev B* **75**, 184440 (2007).
- [5] C. Meneghini, S. Ray, F. Liscio, F. Bardelli, S. Mobilio, and D. D. Sarma, *Phys. Rev. Lett.* **103**, 046403 (2009).
- [6] M. Hennion, et al, *Phys. Rev. Lett.* **94**, 057006 (2005).
- [7] S. Petit, et al, *Phys. Rev. Lett.* **102**, 207201 (2009).
- [8] S. K. Das, V. N. Singh, and P. Majumdar, arXiv: **1204.1194** (2012).
- [9] P. Sanyal, S. Tarat, and P. Majumdar, *Eur. Phys. J. B* **65**, 39 (2008).
- [10] V. N. Singh and P. Majumdar, *Europhys. Lett.* **94**, 47004 (2011).
- [11] S. Kumar and P. Majumdar, *Eur. Phys. J. B* **50**, 571-579 (2006).
- [12] R. S. Fishman, *J. Phys. Cond. Mat.* **21**, 216001 (2009).

# Chapter 7

## Thesis Summary

In this thesis we have studied the impact of the inevitable ‘antisite disorder’ (ASD) in the double perovskites (DPs) of the form  $A_2BB'O_6$ . This antisite disorder arises due to the similar ionic sizes of the B and B'. The B ion can occupy a B' site and *vice versa*. In fact, the B-B' ordering tendency has to compete with the entropy gain from mislocation. Experiments have established that this ASD is spatially correlated rather than randomly distributed. The inevitable ASD has to be understood in any modeling of the double perovskites. The promise of rich functionality in the DPs remains unfulfilled due to this B, B' mislocation.

We have modeled the spatially correlated ASD using a simple *lattice gas* model. Then we defined the electronic-magnetic model on this background and solve it via a real space Monte Carlo technique. On the equilibrium configurations of this problem we have calculated various properties like magnetisation, transport, and the spin resolved density of states. For our study we have considered double perovskites with only the B site having a magnetic moment. The magnetic order in this system is strongly affected by the local ordering of the B and B' ions. Two neighboring B ions, arising from mislocation, have an antiferromagnetic (AFM) superexchange between them. This new coupling can drastically affect physical properties, including magnetic order and transport. Our main observations are the following:

In chapter 3 we have discussed the impact of ASD on the ferromagnetic phase. We discover that, for antisite disorder with a high degree of short-range correlations, the antiphase boundaries act also as magnetic domain walls in the

ferromagnet. Increasing ASD reduces the low-field magnetization, destroys the half-metallicity, and makes the ground state insulating. While these are disadvantages, we also note that the ferromagnetic  $T_c$  is only weakly affected by moderate ASD and the low-field magnetoresistance is dramatically enhanced by disorder. Our real space approach allows an interpretation of these results in terms of the domain pattern, the effective exchange, and the short-range magnetic correlations. They are also consistent with explicit spatial imagery from recent experiments. The “intra-grain” effects highlighted here would be directly relevant to single crystals, and define the starting point for a transport theory of the polycrystalline double perovskites.

Chapter 4 focuses on the metallic antiferromagnetic phase, and the phase co-existence window. For spatially correlated antisite disorder the AFM order is affected *much less strongly* than in the FM case. This intriguing result arises from the finite  $\mathbf{Q}$  nature of AFM order which leads to a weaker ‘cancellation’ of the order between domains. For a given structural order parameter  $S$  (which measures the fraction of correctly located sites) the A type AFM structure factor follows  $D_A \sim (1 + S^2)/2$ , in contrast to  $D_F \sim S^2$  in the ferromagnet, while the G type phase follows  $D_G \sim (1 + S)^2/4$ . So, despite the possibility of large antisite disorder in the electron doped DPs, there is certainly hope of observing AFM phases. The AFM states are metallic, and the electronic wavefunctions in these phases continue to be spatially extended even at large disorder. Antisite disorder increases the residual resistivity, but, unlike the ferromagnet, we do not observe any insulating regime.

Chapter 5 discusses the field response in the antiferromagnetic DP metals. While the zero field resistivity is unremarkable in these systems, they have huge *positive* MR. In contrast to elaborate structure factor measurement, *etc.*, this is a direct indicator of the metallic AFM system. Beyond a modest field needed for suppression of long range AFM order, the system shows more than *ten-fold* increase in resistivity near  $T_c$  in a structurally ordered system. The ratio continues to be almost *two-fold* even in systems with  $\sim 25\%$  ASD. An applied field suppresses long range AFM order leading to a state with *short range AFM correlations* in the field induced FM background. These AFM fluctuations generate

strong electronic scattering and a resistivity that can be much larger than the ordered AFM metal. Although our explicit demonstration is in the context of a two dimensional spin-fermion model of the DPs, the mechanism we uncover is far more general and complementary to the colossal negative MR process. It should operate in other local moment metals that show a field driven suppression of non ferromagnetic order.

Chapter 6 describes our results on magnons in the antisite disordered ferromagnets. We use an effective Heisenberg model with parameters that match the magnetisation from the parent electronic problem. We obtain the magnon excitations using the spin rotation technique coupled with the Holstein-Primakoff transformation in the large spin limit. To leading order this results in a non-interacting disordered boson (magnon) problem that can be solved via Bogolyubov transformation. We provide a detailed description of the spin wave excitations of this complex magnetic state with large spin ( $S$ ), obtained within a  $1/S$  expansion, for progressively higher degree of mislocation, *i.e.*, antisite disorder. The results on magnon energy and broadening reveal that even at very large disorder, the existence of domain like structure ensures that the response has a strong similarity to the clean case. We tried out a scheme for inferring the domain size from the spin wave damping, so that experimenters can make an estimate of domains without having spatial data, and we find it to be reasonably successful. We also highlight how the common assumption about random antisites, that is widely used in modeling these materials, would lead to a gross overestimate of magnon damping. In summary, dynamical neutron scattering can be a direct probe of the unusual ferromagnetic state in these materials and confirm the presence of correlated antisites.

To summarise, this thesis considers some problems in the antisite disordered double perovskite magnets. We clarify the impact of correlated antisite disorder on both ferromagnetic and antiferromagnetic phases, discover that the antiferromagnet is robust to large disorder, and find that the antiferromagnetic metal has a surprisingly large positive magnetoresistance. Finally, we have provided results on the magnon spectrum in the non trivial domain ferromagnetic phase and provide an interpretation of the spectrum in terms of magnon confinement.

